

A 1.3 cm Line Survey toward Orion KL

Y. Gong^{1,2,3}, C. Henkel^{2,4}, S. Thorwirth⁵, S. Spezzano⁵, K. M. Menten², C. M. Walmsley^{6,7}, F. Wyrowski², R. Q. Mao¹, and B. Klein^{2,8}

¹ Purple Mountain Observatory & Key Laboratory for Radio Astronomy, Chinese Academy of Sciences, 2 West Beijing Road, 210008 Nanjing, PR China

² Max-Planck Institut für Radioastronomie, Auf Dem Hügel 69, 53121 Bonn, Germany

³ University of Chinese Academy of Sciences, No. 19A Yuquan Road, 100049 Beijing, PR China

⁴ Astronomy Department, King Abdulaziz University, P.O. Box 80203, Jeddah 21589, Saudi Arabia

⁵ I. Physikalisches Institut, Universität zu Köln, 50937 Köln, Germany

⁶ Osservatorio Astrofisico di Arcetri, Largo E. Fermi, 5, I-50125 Firenze, Italy

⁷ Dublin Institute of Advanced Studies, Fitzwilliam Place 31, Dublin 2, Ireland

⁸ University of Applied Sciences Bonn-Rhein-Sieg, Grantham-Allee 20, 53757 Sankt Augustin, Germany

ABSTRACT

Context. The nearby Orion Kleinmann-Low nebula is one of the most prolific sources of molecular line emission. It has served as a benchmark for spectral line searches throughout the (sub)millimeter regime.

Aims. The main goal is to systematically study spectral characteristics of Orion KL in the $\lambda \sim 1.3$ cm band.

Methods. We carried out a spectral line survey with the Effelsberg-100 m telescope towards Orion KL. It covers the frequency range between 17.9 GHz and 26.2 GHz, i.e., the radio “K-band”. We also examine ALMA maps to address the spatial origin of molecules detected by our 1.3 cm line survey.

Results. In Orion KL, we find 261 spectral lines, yielding an average line density of about 32 spectral features per GHz above 3σ (a typical value of 3σ is 15 mJy). The identified lines include 164 radio recombination lines (RRLs) and 97 molecular lines. The RRLs, from hydrogen, helium, and carbon, originate from the ionized material of the Orion Nebula, part of which is covered by our beam. The molecular lines are assigned to 13 different molecular species including rare isotopologues. A total of 23 molecular transitions from species known to exist in Orion KL are detected for the first time in the interstellar medium. Non-metastable ($J > K$) $^{15}\text{NH}_3$ transitions are detected in Orion KL for the first time. Based on the velocity information of detected lines and the ALMA images, the spatial origins of molecular emission are constrained and discussed. A narrow feature is found in SO_2 ($8_{1,7} - 7_{2,6}$), but not in other SO_2 transitions, possibly suggesting the presence of a maser line. Column densities and fractional abundances relative to H_2 are estimated for 12 molecules with local thermodynamic equilibrium (LTE) methods. Rotational diagrams of non-metastable $^{14}\text{NH}_3$ transitions with $J = K + 1$ to $J = K + 4$ yield different results; metastable ($J = K$) $^{15}\text{NH}_3$ is found to have a higher excitation temperature than non-metastable $^{15}\text{NH}_3$, also indicating that they may trace different regions. Elemental and isotopic abundance ratios are also estimated: $\text{He}/\text{H} = (8.7 \pm 0.7)\%$ derived from the ratios between helium RRLs and hydrogen RRLs; $^{12}\text{C}/^{13}\text{C} = 63 \pm 17$ from $^{12}\text{CH}_3\text{OH}/^{13}\text{CH}_3\text{OH}$; $^{14}\text{N}/^{15}\text{N} = 100 \pm 51$ from $^{14}\text{NH}_3/^{15}\text{NH}_3$; $\text{D}/\text{H} = (8.3 \pm 4.5) \times 10^{-3}$ from $\text{NH}_2\text{D}/\text{NH}_3$. The dispersion of the He/H ratios derived from $\text{Ha}/\text{He}\alpha$ pairs to $\text{H}\delta/\text{He}\delta$ pairs is very small, which is consistent with theoretical predictions that the departure coefficients b_n factors for hydrogen and helium are nearly identical. Based on a non-LTE code neglecting excitation by the infrared radiation field and a likelihood analysis, we find that the denser regions have lower kinetic temperature, which favors an external heating of the Hot Core.

Key words. astrochemistry – ISM: individual (Orion KL) – ISM: molecules – radio lines: ISM – surveys

1. Introduction

One of the best ways to study physical and chemical conditions of astronomical objects is via spectral line surveys. In fact, they are the only means to obtain a complete unbiased view of the molecular inventory of a given source. However, despite the long history of powerful large radio telescopes, only very few unbiased frequency surveys have been conducted in the centimeter wave regime. Spectroscopic features which are expected at centimeter wavelengths include radio recombination lines (RRLs) from hydrogen, helium and carbon, and pure rotational transitions of heavy species such as complex organic molecules which can be detected conveniently at centimeter wavelengths due to their small rotational constants. The molecular lines at centimeter wavelengths are likely to be optically thin and thus analysis is easier than at millimeter wavelengths. Furthermore, the “line

density” is not as high as at millimeter wavelengths, reducing the confusion level.

To summarize previous surveys at centimeter wavelengths: Bell et al. (1993) surveyed W51 from 17.6 to 22.0 GHz with the NRAO 43m telescope; Kalenskii et al. (2004) investigated the dark cloud TMC-1 at 4–6 and 8–10 GHz with the Arecibo 305m telescope; Kaifu et al. (2004) observed TMC-1 from 9 to 50 GHz with the Nobeyama 45m telescope; Gong et al. (2015) measured IRC +10216 from 17.8 to 26.3 GHz with the Effelsberg 100m telescope finding 23 new transitions from species detected previously; Remijan et al. (2008a) surveyed Sgr B2 near the Galactic center with the Green Bank Telescope (GBT) in the course of their GBT PRIMOS project¹ which led to detections of complex organic molecules such as CH_2CHCHO (propenal), $\text{CH}_3\text{CH}_2\text{CHO}$ (propanal) and CNCHO (cyanoformalde-

¹ <http://www.cv.nrao.edu/~aremijan/PRIMOS/index.html>

hyde) (Hollis et al. 2004; Remijan et al. 2008a). They have shown that the centimeter wave range of the electromagnetic spectrum has an enormous potential to detect new molecules and new transitions.

In this study, we present a 1.3 cm line survey toward the Orion Kleinmann-Low nebula (Orion KL). Orion KL has a high luminosity of $\sim 10^5 L_\odot$ (Wynn-Williams et al. 1984), harboring several luminous embedded IR sources, and is the closest high mass star formation region at a distance of 414 ± 7 pc (Menten et al. 2007). The chemistry of this source is particularly rich due to high kinetic temperature of the gas caused by the evaporation of dust grain mantles and the interaction of the newly formed stars with their environment (e.g., Herbst & van Dishoeck 2009; Charnley 1997). It is thus one of the best sources to study the spectral characteristics associated with high-mass star forming regions. So far, many spectral line surveys have been carried out toward Orion KL. The existing surveys, summarized in Table 1, cover a wide frequency range from 34.25 GHz to 6.8 THz. These efforts have resulted in the discovery of a large number of molecules, including, recently, the unusual long complex molecule methyl acetate, $\text{CH}_3\text{COOCH}_3$ (Tercero et al. 2013), as well as a deuterated ammonium cation, NH_3D^+ (Cernicharo et al. 2013). Meanwhile, no comprehensive view exists of our frequency range covered here (17.9–26.2 GHz), although numerous studies have targeted specific lines it contains, e.g., from NH_3 or CH_3OH . Here, we therefore systematically study the $\lambda \sim 1.3$ cm (K band) characteristics of Orion KL.

2. Observation and data reduction

2.1. Observations with the Effelsberg-100m telescope

The measurements were carried out in a position switching mode with the primary focus $\lambda = 1.3$ cm K-band receiver of the 100-m telescope at Effelsberg/Germany², during 2012 January, April and 2013 January, March, and May. The telescope was pointed at $\alpha_{J2000} = 05^{\text{h}}35^{\text{m}}14.17^{\text{s}}$, $\delta_{J2000} = -05^\circ22'46.5''$, about $12''$ south of the dust peak (see Fig. 1a). On- and off-source integration times were two minutes per scan. The newly installed Fast Fourier Transform Spectrometer (FFTS) was used as backend. Each of the two orthogonal linear polarizations was covered with a bandwidth of 2 GHz providing 32768 channels and resulting in a channel spacing of 61 kHz, equivalent to 0.7 km s^{-1} at 26 GHz. The actual frequency and velocity resolutions are coarser by a factor of 1.16 (Klein et al. 2012). Several frequency setups were tuned to cover the entire frequency range from 17.9 GHz to 26.2 GHz with an overlap of at least 100 MHz between two adjacent setups. Across the whole frequency range, the FWHM beamsizes varies from $35''$ to $50''$ ($\sim 40''$ at 23 GHz). The survey encompasses a total of ~ 25 observing hours. The focus was checked every few hours, in particular after sunrise and sunset. Pointing was obtained every hour toward the nearby pointing sources PKS 0420–01 or 3C161 and was found to be accurate to about $5''$. Strong continuum sources (mostly NGC7027 and 3C286) were used to calibrate the spectral line flux, assuming standard flux densities (5.5 Jy for NGC 7027 and 2.5 Jy for 3C286 at 22 GHz; Ott et al. 1994). The typical rms noise is about 3–15 mJy in 61 kHz wide channels. The conversion factor from Jy on a flux density scale (S_ν) to K on a main beam brightness

temperature scale (T_{mb}) is $T_{\text{mb}}/S_\nu \sim 1.7 \text{ K/Jy}$ at 18.5 GHz, 1.5 K/Jy at 22 GHz, and 1.4 K/Jy at 23.7 GHz. Local standard of rest (LSR) velocities are used throughout the paper.

For the data reduction, the GILDAS³ software package including CLASS and GreG was employed. During the data reduction, some inevitable defects were found at the edges of spectra. Therefore 100 channels at each edge of the original spectra were excluded. Fourth to tenth order baselines were subtracted from each spectrum with 2000 to 3000 channels to avoid lines to be truncated at the edge of sub-spectra, and then these sub-spectra were stitched together to reconstruct the complete spectrum. Since some of those sub-spectra also suffer contamination from time variable radio frequency interference (RFI), the channels showing RFI signals have been “flagged”, i.e. discarded from further analysis, resulting in some limited gaps in the averaged spectra. Furthermore, there were a few individual bad channels, which also have been eliminated.

2.2. Archival data

Here, we also present archival ALMA line survey data covering a frequency range of 214–247 GHz to study the distribution of molecules detected by our 1.3 cm line survey. The observations were carried out with 16 antennas on 2012 January 20, during ALMA’s science verification (SV) phase. Callisto and the quasar J0607–085 were used as the flux and phase calibrator, respectively. The spectral resolution is 0.488 MHz, which corresponds to $\sim 0.6 \text{ km s}^{-1}$ at 230 GHz. Its primary beam size ($\sim 30''$) is slightly smaller than the beam size of the Effelsberg-100m in the $\lambda \sim 1.3$ cm band. The CLEAN algorithm in the Common Astronomy Software Applications package (CASA) was used to deconvolve the images applying natural weighting. The synthesized beam size is $1.9'' \times 1.4''$. In this work, we chose to use 11 unpublished transitions (see Table C.1) since several other lines and dust continuum emission from the ALMA data have been already studied (e.g., Neill et al. 2013b,a; Crockett et al. 2014; Wu et al. 2014; Hirota et al. 2015). The data are available to the public and can be accessed from the ALMA-SV website⁴.

Since the ALMA images without short spacings are only sensitive to small-scale structure, we also make use of the VLA C band continuum data⁵ (project AY191A) and the SCUBA–850 μm dust emission (Di Francesco et al. 2008) to trace the large-scale structure of Orion KL. In addition, we also compare the ALMA data with other studies to address the missing flux problem (see Appendix C).

3. Components of Orion KL

Fig. 1a shows the large-scale structure of Orion KL. In Fig. 1b, we present an ALMA 230 GHz continuum image with prominent sources near or within Orion KL indicated. The positions of a few objects, Source n (a protostar coincident with a peculiar double 8.4 GHz radio continuum source), Source I (an embedded massive protostar without submillimeter and infrared continuum, but only SiO maser emission), SMA1 (a compact submillimeter source not detected in the infrared or cm regime) and the BN object (a massive protostar with a circumstellar disk), are based on previous studies (e.g., Menten & Reid 1995; Jiang et al. 2005; Beuther & Nissen 2008; Bally et al. 2011;

² The 100-m telescope at Effelsberg is operated by the Max-Planck-Institut für Radioastronomie (MPIFR) on behalf of the Max-Planck-Gesellschaft (MPG).

³ <http://www.iram.fr/IRAMFR/GILDAS>

⁴ <http://almascience.nrao.edu/alma-data/science-verification>

⁵ Image credit: NRAO/VLA Archive Survey, (c) 2005–2007 AUI/NRAO

Table 1. Existing line surveys of Orion KL.

Orion KL	Covered Frequencies	Telescope	reference
	17.9–26.2 GHz	Effelsberg-100m	This work
34.25–50 GHz & 83.5–84.5 GHz & 86–91.5 GHz ⁽¹⁾		Nobeyama-45m	Ohishi et al. (1986)
42.3–43.6 GHz		GBT-100m	Goddi et al. (2009)
70–115 GHz		NRAO-11m	Turner (1989, 1991)
72–91 GHz		Onsala-20m	Johansson et al. (1984)
67–93.6 GHz		GBT-100m	Frayser et al. (2015)
80–280 GHz ⁽²⁾		IRAM-30m	Tercero et al. (2010, 2011); Esplugues et al. (2013b)
138.3–150.7 GHz		TRAO-14m	Lee et al. (2001)
130–170 GHz		NRAO-12m	Remijan et al. (2008b)
150–160 GHz		FCRAO-14m	Ziurys & McGonagle (1993)
159.7–164.7 GHz		TRAO-14m	Lee & Cho (2002)
190–900 GHz ⁽²⁾		CSO-10m	Serabyn & Weisstein (1995)
215–247 GHz		OVRO-10.4m	Sutton et al. (1985)
216.2–217.2 GHz & 219.1–220.1 GHz & 241–242 GHz & 244–245 GHz		OVRO	Blake et al. (1996)
218.9–221.2 GHz & 228.9–231.2 GHz		IRAM-30m+SMA	Feng et al. (2015)
247–263 GHz		OVRO-10.4m	Blake et al. (1986)
257–273 GHz		JCMT-15m	Greaves & White (1991)
325–360 GHz		CSO-10m	Schilke et al. (1997)
330.5–360.1 GHz & 200.7–202.3 GHz & 203.7–205.3 GHz		NRAO-12m	Jewell et al. (1989)
334–343 GHz		JCMT-15m	Sutton et al. (1995)
455–507 GHz		JCMT-15m	White et al. (2003)
486–492 GHz & 541–577 GHz		Odin satellite	Olofsson et al. (2007); Persson et al. (2007)
607–725 GHz		CSO-10m	Schilke et al. (2001)
795–903 GHz		CSO-10m	Comito et al. (2005)
480–1907 GHz ⁽²⁾		Herschel/HIFI	Crockett et al. (2014)
1595–6816 GHz ⁽³⁾		ISO-60cm	Lerate et al. (2006)

Notes.⁽¹⁾ The covered frequency range is not entirely displayed in their paper.⁽²⁾ Note that the covered frequency range is discontinuous.⁽³⁾ The wavelength range corresponding to the given frequencies is 44 μm –188 μm .

Favre et al. 2011). The positions of IRc1, IRc2, IRc3, IRc4, IRc5, IRc6, and IRc7 infrared emission peaks are taken from Shuping et al. (2004). The millimeter continuum sources MM4, MM5, MM6 are taken from Wu et al. (2014). In the $\lambda \sim 1.3$ cm band, the spectral features of Orion KL can originate from eight distinct components within our $\sim 40''$ beam. These components are:

- (1) ionized gas from the foreground M42 HII region (see Fig. 1a). The contribution can be traced by hydrogen and helium RRLs which have typical velocities $v_{\text{lsr}} \sim -5 \text{ km s}^{-1}$ and large line widths $\Delta v > 15 \text{ km s}^{-1}$ (e.g., Wilson et al. 1997; Peimbert et al. 1992).
- (2) the photon dominated region (PDR). It is the interface region between the molecular cloud and the foreground M42 HII region. It can be traced by carbon RRLs ($v_{\text{lsr}} \sim 9 - 10 \text{ km s}^{-1}$ and $\Delta v \sim 3 - 5 \text{ km s}^{-1}$) (e.g., Natta et al. 1994), which is because carbon ions can exist outside HII regions due to their lower ionization energy (11.3 eV) with respect to that of hydrogen (13.6 eV) (e.g., Wyrowski et al. 1997; Wilson et al. 2009).
- (3) the “hot core” (HC) component. The HC is a well-known source, $\sim 2''$ from IRc2 (see Fig. 1b). It has a high kinetic temperature and a high density ($T_{\text{kin}} > 150 \text{ K}$ and $n > 10^7 \text{ cm}^{-3}$, e.g., Genzel & Stutzki 1989; Mangum & Wootten 1993; Schilke et al. 1997; Wilson et al. 2000; Wang et al. 2010; Goddi et al. 2011; Crockett et al. 2014). Note that an extremely high kinetic temperature is also indicated by detections of high J metastable NH_3 transitions with energy levels up to 1900 K and a high rotational temperature of

$\sim 400 \text{ K}$ (Wilson et al. 1993). The HC is believed to be heated by an explosive event (Bally et al. 2011; Zapata et al. 2011; Nissen et al. 2012). Its line profiles have velocities of $v_{\text{lsr}} \sim 3 - 6 \text{ km s}^{-1}$ and widths of $\Delta v \sim 5 - 12 \text{ km s}^{-1}$.

- (4) the “compact ridge” (CR) component. It is located $\sim 12''$ southwest of the well-known HC (see Fig. 1b). It has densities of $n \sim 10^6 \text{ cm}^{-3}$ and temperatures of $T_{\text{kin}} \sim 80 - 280 \text{ K}$ (e.g., Mangum & Wootten 1993; Beuther et al. 2005; Persson et al. 2007; Wang et al. 2010; Favre et al. 2011). Studies of methanol and methyl formate emission suggest that the CR is externally heated (Wang et al. 2011; Favre et al. 2011). Its line profiles have velocities of $v_{\text{lsr}} \sim 7 - 9 \text{ km s}^{-1}$ and widths of $\Delta v \sim 3 - 6 \text{ km s}^{-1}$.
- (5) the “hot core south” (HC(S)) component. The component was first noticed by studies of HDO (Neill et al. 2013b; Crockett et al. 2014) and is likely to originate from $1''$ south of the well-known HC submillimeter continuum peak (see Fig. 1b). It shows a spectral feature with $v_{\text{lsr}} \sim 6.5 - 8 \text{ km s}^{-1}$ and $\Delta v \sim 5 - 10 \text{ km s}^{-1}$.
- (6) the “extended ridge” (ER) component. It represents the ambient gas of Orion KL. It has densities of $n \sim 10^4 - 10^6 \text{ cm}^{-3}$ and temperatures of $T_{\text{kin}} < 60 \text{ K}$ showing spectral features of $v_{\text{lsr}} \sim 8 - 10 \text{ km s}^{-1}$ and $\Delta v \sim 2 - 5 \text{ km s}^{-1}$ (e.g., Blake et al. 1986; Schilke et al. 1997; Persson et al. 2007).
- (7) the “plateau” component. The component is characterized by velocities $v_{\text{lsr}} \sim 6 - 12 \text{ km s}^{-1}$ and large line widths $\Delta v > 20 \text{ km s}^{-1}$, which are attributed to outflows. Orion KL is known to contain at least two outflows, historically referred to as the low velocity flow (LVF) and the high velocity flow

- (HVF) (e.g., Genzel et al. 1981). The LVF is oriented along the SW-NE direction and is thought to be driven by radio source I (e.g., Genzel & Stutzki 1989; Menten & Reid 1995; Greenhill et al. 1998; Plambeck et al. 2009). It has spectral features of $v_{\text{lsr}} \sim 5 \text{ km s}^{-1}$ and $\Delta v \sim 18 \text{ km s}^{-1}$. The HVF, more extended than the LVF, is oriented along the SE-NW direction and is thought to be driven by the submillimeter source SMA1 or the dynamical decay of a multi-star system involving radio source I, source n and the BN object that caused the explosive event described in (3) above (e.g., Beuther & Nissen 2008; Bally et al. 2011; Goicoechea et al. 2015). It has spectral features of $v_{\text{lsr}} \sim 10 \text{ km s}^{-1}$ and the line widths can be very large reaching velocities up to 150 km s^{-1} .
- (8) the millimeter continuum sources MM4, MM5, and MM6 taken from Wu et al. (2014). Based on their $^{13}\text{CH}_3\text{CN}$ studies, MM4, MM5, and MM6 are found to have rotational temperatures of $182^{+81}_{-43} \text{ K}$, $157^{+43}_{-28} \text{ K}$, and $119^{+18}_{-14} \text{ K}$, respectively. The $^{13}\text{CH}_3\text{CN}$ spectral features are: MM4 with velocities of $v_{\text{lsr}} \sim 5.5 \text{ km s}^{-1}$ and widths of $\Delta v \sim 5.9 \text{ km s}^{-1}$; MM5 with velocities of $v_{\text{lsr}} \sim 10.1 \text{ km s}^{-1}$ and widths of $\Delta v \sim 5.4 \text{ km s}^{-1}$; MM6 with velocities of $v_{\text{lsr}} \sim 7.5 \text{ km s}^{-1}$ and widths of $\Delta v \sim 5.7 \text{ km s}^{-1}$. From Fig. 1b, MM4 is close to IRC7 while MM6 is close to IRC6.

4. Results

4.1. Line identifications

The line identification was performed with the help of the JPL⁶, CDMS⁷, and splatalogue⁸ databases as well as the on-line Lovas line list⁹ for astronomical spectroscopy (Müller et al. 2005; Pickett et al. 1998; Lovas & Dragoset 2004). However, the rest frequencies of RRLs are not contained in these databases, and are thus calculated with the Rydberg formula

$$\nu_{n_2 \rightarrow n_1} = R \left(\frac{1}{n_1^2} - \frac{1}{n_2^2} \right), \quad n_1 < n_2, \quad (1)$$

where $\Delta n = n_2 - n_1$. n_2 and n_1 are the principle quantum numbers of the upper and lower state, R is the Rydberg constant which is equal to $3.28805129 \times 10^{15} \text{ Hz}$ for hydrogen, and $3.28939118 \times 10^{15} \text{ Hz}$ for helium (Wilson et al. 2009). The nomenclature for RRLs is based on n_1 and Δn . For example, H71 α is corresponding to a hydrogen RRL with $n_1 = 71$, $n_2 = 72$, and $\Delta n = 1$. The Greek alphabet corresponds to Δn , e.g., α is corresponding to $\Delta n = 1$, β is corresponding to $\Delta n = 2$, etc.

A line is identified as real if it exhibits a 3σ feature in more than 3 adjacent raw channels. On the other hand, there are a few narrow lines which are also identified as real even though their intensity is above 3σ for fewer than 3 adjacent raw channels. Such lines show up as doublets (e.g., CH_3OCHO , CH_3OCH_3), which confirms our assignment. Identified lines are listed in Table 2. Given that line profiles are complex in Orion KL, different methods are employed to fit our observed lines. For RRLs, we simply use one single Gaussian component to derive their observed properties. For molecular lines showing nuclear quadrupole hyperfine structure (hfs, like HC_3N , CH_3CN , HNCO , NH_3 , etc.), we used the HFS fitting routine embedded

in CLASS to derive the observed properties (including the optical depth) while least-square fits of Gaussians are performed for the other molecular transitions. On the other hand, the observed lines of sulfur-bearing molecules are composites of different distinct components, so here the approach we take is to adopt a range of velocities and line widths of different components to separate their contributions. This is based on general knowledge of the source (see Sect. 3). The NH_3 emission also originates from several components, but here the situation is even more complex. In this case, multiple component fitting becomes unrealistic. Therefore, we only give the integrated intensities for those NH_3 transitions which have a heterogeneous origin. Although Ca lines are blended with $\text{He}\alpha$ lines, we present double Gaussian fits to separate their relative contributions to obtain the observed properties of Ca lines since little information about Ca lines exists in the literature. For other blended transitions, we do not separate the lines but simply integrate the whole line profiles to obtain upper limits to the integrated intensities of individual spatial subcomponents.

The observed line parameters for different species are displayed in Tables A.1–A.6, where the rms noise σ given is for 61 kHz wide channels. Fig. 2 shows an overview of the 1.3 cm spectral line survey toward Orion KL. In the survey, we find 261 lines, yielding an average line density of about 32 spectral features per GHz above 3σ . The line density is much smaller than that at millimeter wavelengths (e.g., Tercero et al. 2010). All lines are identified. The identified lines include 164 RRLs and 97 molecular lines. The RRLs, from hydrogen, helium, and carbon, originate from the ionized material of the Orion Nebula, part of which is covered by our beam. The molecular lines are assigned to 13 different molecules including rare isotopologues. 23 lines from already known species are detected for the first time in the interstellar medium (marked by an “N” in the last column of Table 2). 19 molecular lines or carbon RRLs are blended with neighbouring hydrogen or helium RRLs. From Fig. 2, we can see that the spectrum is dominated by strong lines arising from four species, the super strong H_2O ($6_{1,6}-5_{2,3}$) maser with $S_\nu > 30000 \text{ Jy}$, the series of CH_3OH maser lines starting at $\approx 25 \text{ GHz}$ with $S_\nu > 10 \text{ Jy}$, low J metastable transitions of NH_3 with $S_\nu > 5 \text{ Jy}$ and $\text{H}\alpha$ lines with $S_\nu > 2 \text{ Jy}$. Fig. B.1 shows the observed spectrum in more detail. Each panel covers $\sim 500 \text{ MHz}$ with a 10 MHz overlap between adjacent panels so that lines truncated in one panel will not be truncated in the neighboring panel. In addition, Fig. B.2–B.16 shows zoom-in plots of all identified lines.

4.2. Radio recombination lines

From Fig. B.1 and Table 2, we find that the frequency range is mainly occupied by RRLs. Among the 164 RRLs, there are 116 hydrogen RRLs, 39 helium RRLs, and 9 carbon RRLs. Their spectra are shown in Figs. B.2–B.10 and their observed line parameters are given in Table A.1. 56 hydrogen RRLs with $\Delta n \geq 6$ are detected. Furthermore, hydrogen RRLs with Δn as high as 11 are detected in this survey while hydrogen RRLs with even higher Δn (≤ 25) are reported by Bell et al. (2011). Carbon RRLs are all blended with helium RRLs since line widths of RRLs are broad and the separations between the rest frequencies of carbon RRLs and helium RRLs with the same n_1 and Δn are small. Furthermore, the velocity differences shift the carbon RRLs slightly into the He RRLs (See Sect. 3 for the differences with respect to radial velocities.).

From Fig. 3a, we can see that line widths ($\sim 24 \text{ km s}^{-1}$) of hydrogen RRLs are broader than those ($\sim 16 \text{ km s}^{-1}$) of he-

⁶ <http://spec.jpl.nasa.gov>

⁷ <http://www.astro.uni-koeln.de/cdms/catalog>

⁸ <http://www.splatalogue.net>

⁹ <http://www.nist.gov/pml/data/micro/index.cfm>

lium RRLs. The line broadening of RRLs is thought to arise from thermal motions and turbulence (Wilson et al. 2009). The observed line width, $\Delta\nu$, has a thermal and a turbulent contribution, $\Delta\nu = \sqrt{\Delta\nu_{\text{th}}^2 + \Delta\nu_{\text{tur}}^2}$, where $\Delta\nu_{\text{th}}$ is the thermal width, and $\Delta\nu_{\text{tur}}$ is the line width caused by turbulent flows. Taking the electron temperature of the foreground HII region as 8300 K (Wilson et al. 1997) and following a Maxwell-Boltzmann velocity distribution, the thermal widths of hydrogen and helium are estimated to be 19.5 km s^{-1} and 9.8 km s^{-1} with the formula $\Delta\nu_{\text{th}} = 2\sqrt{2\ln 2}(\frac{kT}{m})^{1/2}$, where k is the Boltzmann constant, T is the electron temperature, and m is the mass of a particle. Consequently, the average hydrogen and helium turbulent line widths are estimated to be $14.1 \pm 1.0 \text{ km s}^{-1}$ and $12.4 \pm 1.4 \text{ km s}^{-1}$, respectively. From Fig. 3b, we can see that most points lie below the red dashed line where the turbulent line widths are equal for hydrogen and helium. This suggests that hydrogen turbulent line widths might be slightly larger than those of helium. However, the large errors make it uncertain. If the difference can be confirmed, that may indicate that hydrogen RRLs trace a larger portion of ionized gas than helium RRLs in Orion KL. The exciting stars of the HII region have $T_{\text{eff}} \sim 4 \times 10^4 \text{ K}$ (Baldwin et al. 1991). This is higher than the critical T_{eff} of 37000 K, below which helium is no longer appreciably ionised (Wilson et al. 2009). The innermost parts of their HII regions should therefore show ionized HeII. The outer parts, however, are devoid of HeII, while still containing ionized hydrogen. The larger volume leads to a larger line width. Nevertheless, the bulk of the discrepancy between observed line widths of hydrogen and helium RRLs originates from their thermal contributions.

Assuming local thermodynamic equilibrium (LTE) and following the formulae (6.24)–(6.27) of Brocklehurst & Seaton (1972), the intensity ratios of RRL pairs with different Δn from the same atom at neighbouring frequencies (e.g., H88 β /H70 α) are found to be

$$\frac{T_{\Delta n_1}}{T_{\Delta n_2}} = \frac{\Delta n_1 K(\Delta n_1)}{\Delta n_2 K(\Delta n_2)}, \quad (2)$$

where Δn_1 and Δn_2 represent different Δn defined in formula (1), and $\Delta n K(\Delta n)$ is given in Table I of Brocklehurst & Seaton (1972). From Fig. 4, we find that observed ratios from H β /H α , H γ /H α , H δ /H α , are consistent with LTE ratios. Based on a table of the departure coefficients b_n provided by Salem & Brocklehurst (1979), we find that all b_n factors are larger than 0.94 and smaller than unity, when adopting an electron temperature of 8300 K and an electron density of $1 \times 10^4 \text{ cm}^{-3}$ (Wilson et al. 1997). Therefore, we suggest that the LTE deviations are very small for these RRLs in Orion KL.

4.3. Molecular lines

In this section, we focus on the origin of detected molecular lines according to the line parameters obtained by Gaussian fits or hfs fits in our survey as well as spatial distributions of their corresponding transitions at higher frequencies obtained from the ALMA-SV data (see Table C.1 and Fig. C.1).

4.3.1. NH_3 , $^{15}\text{NH}_3$, and NH_2D

In our band, we find 7 metastable NH_3 transitions, 27 non-metastable NH_3 transitions, 7 metastable $^{15}\text{NH}_3$ transitions, 3 non-metastable $^{15}\text{NH}_3$ transitions, and 2 NH_2D transitions (see

Table A.2 and Fig. B.11). It is worth noting that the non-metastable $^{15}\text{NH}_3$ transitions are detected in Orion KL for the first time. The line widths of non-metastable $^{15}\text{NH}_3$ transitions become narrower with increasing J , while there is no such trend for the metastable $^{15}\text{NH}_3$ transitions (see Fig. B.12 and Table A.2). This suggests that higher- J non-metastable transitions may trace denser regions where turbulent motions become less dominant. We note that the errors of the line widths ($\sim 1 \text{ km s}^{-1}$) are large compared to the differences between these line widths, so further observations are needed to confirm the trend. Based on previous VLA ammonia observations (e.g., Genzel et al. 1982; Goddi et al. 2011), NH_3 emission is mainly found in the HC, the Plateau, MM4, MM5, and MM6, but barely in the CR. Velocities around 6 km s^{-1} and large line widths suggest that $^{15}\text{NH}_3$ mainly comes from the HC. One of the two NH_2D transitions belongs to the para, the other to the ortho species¹⁰, which have already been reported by Walmsley et al. (1987). The intensity of NH_2D ($4_{1,4a} - 4_{0,4s}$) from our observations is smaller than theirs, but is still within their uncertainties. NH_2D ($3_{1,3s} - 3_{0,3a}$) is blended with NH_3 ($8,5$) at 18808.5 MHz and H118 ϵ at 18808.4 MHz (see Fig. B.12). From Fig. C.1, NH_2D emission is found in the HC, the HC(S), and in MM4. NH_2D ($3_{1,3s} - 3_{0,3a}$) and ($4_{1,4a} - 4_{0,4s}$) are considered to arise from the HC in the following analysis.

4.3.2. H_2O and HDO

We find one H_2O line and one HDO line (see Table A.6). The H_2O ($6_{1,6} - 5_{2,3}$) maser is blended with NH_3 ($3,1$), and shows multiple velocity components which have peak intensities of $>1000 \text{ Jy}$ (see Fig. B.16). A previous deuterated water study has shown that HDO mainly comes from the HC(S) (see Fig. 6 of Neill et al. 2013b). Although HDO ($3_{2,1} - 4_{1,4}$) is blended, it clearly peaks at $\sim 7 \text{ km s}^{-1}$, which coincides with the velocity of the HC(S). This also points out that the deuterated water arises mainly from the HC(S).

4.3.3. Sulfur-bearing molecules, SO_2 and OCS

We find five transitions of SO_2 and one transition of OCS in the survey. Most of the unblended lines can be fitted with two velocity components (see Fig. B.14 and Table A.4). From Fig. C.1, we can see that the SO_2 emission around 6 km s^{-1} mainly comes from the HC. Thus, the two velocity components are assigned to the HC and the plateau. But for SO_2 ($8_{1,7} - 7_{2,6}$), it cannot be fitted with two Gaussian components. There is an additional narrow component which has a velocity of $\sim 8 \text{ km s}^{-1}$ and a line width of $\sim 2 \text{ km s}^{-1}$ when we fit the line with three Gaussian components. It may result from emission from the CR, an outstanding emitter of transitions at low upper level energy, but it is narrower than the typical SO_2 line width ($3\text{--}6 \text{ km s}^{-1}$) of the CR (Esplugues et al. 2013b). Alternatively, it may be affected by population inversion since the narrow component is not detected in other SO_2 transitions in our band and the 1.3, 2mm, and 3 mm bands (Esplugues et al. 2013b). Furthermore, SO_2 is extremely enhanced by shocks so that it becomes the strongest coolant in

¹⁰ For NH_2D , the inversion motion splits each rotational level (denoted by the quantum numbers $J_{k_a k_c}$) into two inversion states, labeled as “s” and “a”, corresponding to symmetric and antisymmetric states of the two equivalent minimum-energy structures (Ho & Townes 1983). The ortho levels are those in the “s” state with odd k_a and in the “a” state with even k_a while other states belong to the para species.

the 607–725 GHz survey which outperforms CO by a large factor (Schilke et al. 2001).

OCS (2–1) also shows two components, but the fitted velocity and line width are different from those derived from SO₂ (see Table A.4). The line width of the plateau component from OCS is much narrower than found for SO₂. This is probably because OCS (2–1) is only excited in the LVF. Based on the distributions of OCS (see Fig. C.1), the other component of OCS (2–1) is assigned to the HC(S) according to the fitted velocity and line width.

4.3.4. Cyanopolyynes, HC₃N and HC₅N

Cyanopolyynes are well studied and abundant in many different astronomical environments such as the late-type carbon star IRC +10216 and the cold starless core TMC-1 (e.g., Cernicharo et al. 2000; Kaifu et al. 2004) whereas they are not prominent in Orion KL (Esplugues et al. 2013a). BIMA observations show that toward Orion KL, HC₃N emission originates in the HC (Wright et al. 1996) whereas the origin of HC₅N is still a puzzle. In our survey, we find one HC₃N line and two HC₅N lines (see Fig. B.16). Based on the measured velocities and line widths (see Table A.6), HC₅N seems to originate from the CR or the HC(S) or the ER. From Fig. C.1, we confirm that HC₃N is mainly from HC while HC₅N is not detected in the archival ALMA data. Nevertheless, it would be very surprising if HC₃N and HC₅N would not share the same spatial origin in Orion KL. Assuming that HC₅N originates from the same region as HC₃N, the HC₅N/HC₃N abundance ratio is estimated to be $(2.8 \pm 0.7) \times 10^{-2}$ according to Table 3. This is slightly lower than the $(7 \pm 4) \times 10^{-2}$ of Esplugues et al. (2013a). HC₅N (7–6) is inside the frequency range covered by our survey. With the rotational temperatures and column densities listed in Table 3, we can estimate the peak intensity of HC₅N (7–6) by assuming a low opacity, a Gaussian profile, a line width of 5 km s⁻¹, and a source size of 10". The peak intensity is estimated to be about 0.012 Jy, so its non-detection can be expected. On the other hand, we do not detect HC₇N and HC₉N transitions in this band which are detected in large numbers toward TMC-1 and IRC +10216 (Kaifu et al. 2004; Gong et al. 2015). HCN $\nu_2=1$ direct *l*-type transitions detected originally in the protoplanetary nebula CRL 618 (Thorwirth et al. 2003) and selected high-mass star-forming regions (Thorwirth 2001) as well as the prototypical starburst galaxy Arp 220 (Salter et al. 2008) are also not detected in this survey. A tentative detection of the $J = 9$ direct *l*-type transition towards Orion KL reported earlier (Thorwirth 2001) could not be confirmed here.

4.3.5. CH₃OH and ¹³CH₃OH

In this survey, we find seventeen CH₃OH ($\nu_t=0$) transitions, four torsionally excited CH₃OH ($\nu_t=1$) transitions, and one ¹³CH₃OH ($\nu_t=0$) transition. The $J_2 - J_1$ *E* methanol masers with $J = 2...10$, already reported (e.g., Menten et al. 1988a), are all detected. From Fig. 5, our measurements show that the peak intensities of these masers increase with principle quantum number J from 2 to 6 and decrease with J from 6 to 10. This is consistent with the result of Menten et al. (1986), although the $J_2 - J_1$ *E* methanol masers with $J = 8, 9$ are not included in their analysis. The newly detected CH₃OH (26₂ – 26₁ *E*) line, belonging to the $J_2 - J_1$ *E* class, might not to be affected by population inversion, since it agrees well with the fit to the rotational diagram to CH₃OH transitions (see Sect. 5.1). From Fig. C.1, we can see

that methanol exists in the HC, the HC(S), the CR, MM4, MM5 and MM6. Based on the fitted line widths and velocities (see Table A.3), we suggest that transitions detected by our survey mainly arise from the CR.

4.3.6. HNCO

From Fig. C.1, HNCO is found to exist mainly in the HC, the HC(S), and MM4 while only weak emission arises from MM5, MM6, and the CR. The HNCO emission in HC(S) stands out around velocities ranging from 6–10 km s⁻¹. In combination with the fitted parameters of HNCO (1–0) (see Table A.6), we suggest that HNCO (1–0) mainly originates from the HC(S). HNCO is believed to be enhanced in shocked regions (Zinchenko et al. 2000), which may indicate that the HC(S) component is formed via shocks due to the interaction between the outflowing gas and ambient clouds.

4.3.7. H₂CO

In this survey, we find one transition of H₂CO, the 9_{2,7}–9_{2,8} line, which is from the para state of H₂CO. From Fig. C.1, H₂CO is found to exist in the HC, the HC(S), the CR, the Plateau, MM5, and MM6. Based on the fitted parameters (see Table A.6), H₂CO (9_{2,7}–9_{2,8}) may arise from the HC(S) or the CR. On the other hand, H₂CO (9_{2,7}–9_{2,8}) has an upper energy of 205 K, so we suggest that H₂CO (9_{2,7}–9_{2,8}) is mainly from the HC(S).

4.3.8. CH₃CN and CH₃CH₂CN

One CH₃CN transition and one CH₃CH₂CN transition are detected in our survey. Based on Fig. C.1, we find that the CH₃CN emission arises from many spatial components, among which the HC is the strongest, while CH₃CH₂CN emission is mainly from the HC, followed by MM4. Inspecting the fitted parameters for CH₃CN (1₀–0₀) and CH₃CH₂CN (3_{1,3}–2_{1,2}) (see Table A.6), we suggest that the two transitions are also mainly from the HC. The line profile of CH₃CH₂CN (3_{1,3} – 2_{1,2}) is broad, because its hfs lines are blended. Although many other CH₃CH₂CN transitions with similar upper level energies fall in this band, they are expected to be much weaker since their intrinsic strengths are much lower.

4.3.9. CH₃OCHO and CH₃OCH₃

In our survey, we find twelve CH₃OCHO transitions and two CH₃OCH₃ transitions (see Table A.5 and Table A.6). Based on the fitted velocities and narrow line widths, we suggest that CH₃OCHO and CH₃OCH₃ originate from the CR. From Fig. C.1, we find that the emissions of CH₃OCHO and CH₃OCH₃ mainly come from the CR, followed by MM5 and MM6.

4.3.10. A brief summary

The origin of molecules detected by our 1.3 cm line survey is briefly summarized in Table 4, demonstrating that chemical differentiation exists in Orion KL. This differentiation is roughly consistent with the fact that nitrogen-bearing molecules are favored in the HC while oxygen-bearing molecules are more predominant in the CR (e.g., Beuther et al. 2005; Friedel & Snyder 2008).

5. Discussion

5.1. Rotational temperatures, column densities and fractional abundances relative to H_2

Given that the density in Orion KL is relatively high (see Sect. 3), LTE should be a good approximation. In the 1.3 cm wavelength range, the continuum emission is dominated by free-free emission. Toward Orion KL, free-free emission originates mainly from its foreground HII region M42 and is optically thin in the 18–26 GHz band (Mezger & Henderson 1967; Terzian & Parrish 1970). So the free-free continuum emission of Orion KL itself is simply assumed to be zero in the radiative transfer equation to estimate the opacity of molecular transitions at 1.3 cm wavelength. Thus, the opacity at the line center can be estimated via a formula given by Wilson et al. (2009),

$$\tau = -\ln\left(1 - \frac{T_{mb}}{f(J(T_{rot}) - J(T_{bg}))}\right), \quad (3)$$

where T_{mb} is the observed peak intensity, T_{rot} is the rotational temperature, and T_{bg} is the 2.73 K cosmic microwave background brightness temperature. f is the filling factor $f = \theta_s^2 / (\theta_s^2 + \theta_{beam}^2)$, where we assume a Gaussian source and beam width FWHM of θ_s and θ_{beam} , respectively. $J(T) = \frac{h\nu}{k} \frac{1}{e^{h\nu/kT} - 1}$, h is the Planck constant, ν is the rest frequency of the analyzed transition, and k is the Boltzmann constant. If we take a filling factor of 0.06 (corresponding to an assumed source size of $10''$) and a rotational temperature of 100 K, a peak intensity of 1 K (corresponding to ~ 0.7 Jy at 22 GHz) is equivalent to an opacity of 0.18 at the line center. When a higher rotational temperature is taken, the opacity becomes even lower. Thus, most of the detected thermally excited molecular lines appear to be optically thin, with the exception of the low J NH_3 transitions. On the other hand, lines with hfs allow for determinations of opacity as well. Based on the HFS fitting routine in CLASS, we confirm that HC_3N (2–1), CH_3CN (1₀–0₀), $HNCO$ (1_{0,1}–0_{0,0}), and CH_3CH_2CN (3_{1,3}–2_{1,2}) are optically thin (see Table A.6).

Below, we use rotational diagrams to roughly estimate rotational temperatures and column densities. The standard formula used here is

$$\ln\left(\frac{3kW}{8\pi^3\nu\mu^2S}\right) = \ln\left(\frac{N_{tot}}{Q(T_{rot})}\right) - \frac{E_u}{kT_{rot}}, \quad (4)$$

where k is the Boltzmann constant, W is the integrated intensity, ν is the rest frequency, μ is the permanent dipole moment, S is the transition's intrinsic strength, N_{tot} is the total column density, T_{rot} is the rotational temperature, Q is the partition function, and E_u is the upper level energy of the transition. The values of Q and μ are taken from the CDMS and JPL catalogs. Note that the partition function for CH_3OH and $^{13}CH_3OH$ has included the vibrational state $v_t=0$ and $v_t=1$ (Dr. Christian P. Endres, priv. comm.). For molecules with at least two transitions, we use least-square fits to the rotational diagrams to derive their rotational temperatures and column densities. For molecules with only one transition detected, we fix rotational temperatures, according to the values from literature or chemically related molecules, to derive their column densities (see Table 3). But for HC_5N , the fitted rotational temperature is about 1 K, which is not reasonable. This is because we only detect two HC_5N transitions and their upper level energy difference (~ 1 K) is very small. Thus, rotational temperatures of 30 K and 200 K are taken to derive the column density of HC_5N assuming that HC_5N originates from the CR and HC, respectively.

Following previous studies (Neill et al. 2013a; Crockett et al. 2014), we assume that all molecules with the same origin have the same source size to simplify the calculation. Adopted source sizes for each component are also based on Table 2 of Crockett et al. (2014) and the parameters of the HC(S) are assumed to be the same as those of the HC. With the adopted source sizes, the observed intensities are corrected for beam dilution by dividing by the filling factor to derive source-averaged column densities. The H_2 column densities adopted in Crockett et al. (2014) are used to calculate fractional abundances of the detected molecules.

Fig. 6 shows rotational diagrams for molecules with more than two transitions detected in our survey. For NH_3 , we only fit the non-metastable transitions since metastable transitions consist of several components and decompositions based on the velocity information may be less accurate. In the fitting process, we separate non-metastable transitions into four classes which are labeled as $J = K + 1$, $J = K + 2$, $J = K + 3$, and $J = K + 4$. For $J = K + 1$, NH_3 (2,1), (3,2), (4,3), (5,4), (6,5), and (7,6) are ignored in the fitting process since they are potentially contaminated by emission from other components rather than only from the HC component (see Fig. B.11). From the fitted result (see Fig. 6) where the ortho-to-para ratio is set to unity (based on the analysis of $^{15}NH_3$, see the discussion below), we find that only NH_3 (2,1) and (3,2) deviate significantly, while all others lie along the fitted line which suggests that other $J = K + 1$ transitions are also dominated by the HC component. Nevertheless, if NH_3 (8,7), (9,8), (10,9), and (11,10) are not optically thin, the derived rotational temperature will be overestimated and the derived column density will be underestimated. We also find that the fits for $J = K + 2$ and $J = K + 3$ have rotational temperatures similar to $J = K + 1$. However, the fit for $J = K + 4$ has a much lower rotational temperature. Furthermore, the derived NH_3 column densities go up from $J = K + 1$ to $J = K + 4$. This suggests that the four classes may trace different NH_3 emission regions. However, it is surprising that the $J = K + 4$ class has the largest column density among the four since the $J = K + 4$ transitions require particularly high excitation. We also note that the fit for the $J = K + 4$ class may have large uncertainties since we only have three data points.

To determine the ortho-to-para ratio of ammonia, $^{15}NH_3$ is more suited since the optical depths are much smaller than those of NH_3 . Assuming that this rare isotopologue was formed in the same region as its main species, we fit its para and ortho states of metastable transitions separately (see Fig. 6). The ortho-to-para ratio is estimated to be 0.99 ± 0.34 , in accord with the result ($0.7_{-0.3}^{+0.5}$) of Hermsen et al. (1985), agreeing very well with the fact that the ortho-to-para ratio approaches the statistical ratio of unity when ammonia is equilibrated under high kinetic temperature conditions (e.g., Takano et al. 2002). On the other hand, we find that metastable $^{15}NH_3$ has a higher excitation temperature than non-metastable $^{15}NH_3$ although only three points have been fitted for the non-metastable $^{15}NH_3$ (see Fig. 6 and Table 3). This is likely due to the fact that the metastable line excitation is dominated by collisions while the excitation of the non-metastable transitions follows the radiation field. In the very dense medium, collisional (T_{kin}) and radiative (T_{rad}) temperatures could be the same. However, T_{rad} may suffer from beam dilution effects, which results in lower rotational temperatures. Alternatively, non-metastable $^{15}NH_3$ transitions trace higher densities than its metastable counterparts, and thus represent the temperature of higher excited inner regions than metastable transitions. Meanwhile, the HC is believed to be externally heated by an explosive event (Bally et al. 2011;

Zapata et al. 2011; Nissen et al. 2012), so the innermost region could be colder. Therefore, non-metastable transitions of $^{15}\text{NH}_3$ can be expected to have a lower rotational temperature than its metastable transitions. This is also consistent with the fact that the $J = K + 4$ transitions of $^{14}\text{NH}_3$, tracing denser regions, have a lower rotational temperature.

No CH_3OH maser lines were included in the fit due to their deviation from LTE. CH_3OH ($2_1 - 3_0\text{E}$) was also not included because this line comprises several velocity components due to its low upper level energy ($E_u/k = 28$ K). We fit the A type and the E type of CH_3OH and CH_3OCHO , separately. Consequently, the CH_3OCHO A/E abundance ratio is estimated to be 1.38 ± 0.26 slightly higher than the expected value of unity while the CH_3OH A/E abundance ratio is estimated to be 0.77 ± 0.33 , slightly lower than the expected value of unity. Nevertheless, the differences could be caused by uncertainties. For SO_2 , we fit its HC component and its plateau component separately. We find that the HC component has a higher rotational temperature and a higher column density than its plateau component.

The resulting rotational temperatures and column densities, together with results obtained with single dish telescopes from the literature, are given in Table 3. We find fitted rotational temperatures ranging from 69 to 209 K and derived molecular column densities ranging from 9.6×10^{13} to $1.9 \times 10^{18} \text{ cm}^{-2}$. This results in fractional abundances spanning over more than four orders of magnitude. Taking beam dilution into account, we find that most of our results agree well with previous studies based on (sub)millimeter lines except for SO_2 , CH_3CN , and HNCO . Our SO_2 column density for the HC is less than that of Crockett et al. (2014) by a factor of 6. This is because our fitted rotational temperature is much lower and the SO_2 lines of Crockett et al. (2014) at higher frequencies, trace higher temperatures. The derived column densities of HC_3N , HC_5N , CH_3CN and HNCO are higher than those from previous studies listed in Table 3. The upper level energies of their transitions are very low, so they are probably contaminated by other components not being part of the HC. Thus, our assumed source size of $10''$ could be an underestimate, which results in an overestimated column density. The derived column densities should then be upper limits for the average column density of those molecules. Alternatively, previously reported column densities were derived from (sub)millimeter lines which may suffer from opacity effects, leading to an underestimate of their column densities.

5.2. Elemental and isotopic abundance ratios in Orion KL

The He^+/H^+ , $^{12}\text{C}/^{13}\text{C}$, $^{14}\text{N}/^{15}\text{N}$, and D/H abundance ratios are fundamental parameters for the study of cosmology and the evolution of galaxies (e.g., Boesgaard & Steigman 1985; Wilson & Rood 1994; Steigman 2007).

5.2.1. He/H

Benefiting from a large number of RRLs, we can make use of hydrogen and helium RRL pairs to estimate the He^+/H^+ abundance ratio which can be used to evaluate the He/H abundance ratio. Under LTE conditions, the He/H abundance ratio can be

calculated via the integrated intensity of Gaussian fits to the hydrogen and helium RRLs (e.g., Churchwell et al. 1974):

$$y = \frac{N(\text{He})}{N(\text{H})} \approx \frac{1}{R} \frac{\int_{\Omega_s} d\Omega \int S_\nu(\text{He}^+) d\nu}{\int_{\Omega_s} d\Omega \int S_\nu(\text{H}^+) d\nu}, \quad (5)$$

where R is the ratio of volumes of He^+ and H^+ Strömgren spheres, weighted by the square of the proton density, Ω_s is the source solid angle, $\int S_\nu(\text{He}^+) d\nu$ and $\int S_\nu(\text{H}^+) d\nu$ are the observed integrated intensities of corresponding helium and hydrogen RRLs. Assuming that the HII region has the same size as the HeII region, formula (5) becomes

$$y = \frac{N(\text{He})}{N(\text{H})} \approx \frac{\int S_\nu(\text{He}^+) d\nu}{\int S_\nu(\text{H}^+) d\nu}. \quad (6)$$

In this work, there are 28 unblended pairs which are from $\text{Ha}/\text{He}\alpha$, $\text{H}\beta/\text{He}\beta$, $\text{H}\gamma/\text{He}\gamma$, and $\text{H}\delta/\text{He}\delta$. The rest frequencies of these pairs are only about 7 MHz apart, so their ratios should be free of uncertainties related to pointing accuracy, calibration errors, and different beam widths. Fig. 7 shows the derived He/H abundance ratios according to formula (6). We find that uncertainties increase from $\text{Ha}/\text{He}\alpha$ to $\text{H}\delta/\text{He}\delta$. Thus, we take the sigma-weighted mean value as the He/H abundance ratio which is estimated to be $(8.7 \pm 0.7)\%$. This agrees well with previous studies (Peimbert et al. 1992; Wilson & Rood 1994; Quireza et al. 2006), and is slightly lower than the $(9.1 \pm 0.5)\%$ from previous $\text{H}66\alpha$ and $\text{He}66\alpha$ measurements which were pointed at the HII maximum (Thum et al. 1980). Therefore, we confirm that the He/H abundance ratio is comparable to the primordial He/H abundance ratio of $\sim 8.3\%$ due to Big Bang Nucleosynthesis (BBN; Olive & Skillman 2004; Steigman 2007) and the solar value ($\sim 9.8\%$; Wilson & Rood 1994), which indicates that the He/H abundance ratio is mainly determined by BBN but little affected by stellar nucleosynthesis. Furthermore, the dispersion of the ratios derived from $\text{Ha}/\text{He}\alpha$ pairs to $\text{H}\delta/\text{He}\delta$ pairs is small (see Fig. 7), suggesting that the departure coefficients, the b_n factors, are nearly identical for hydrogen and helium. This agrees well with theoretical predictions (e.g., Storey & Hummer 1995).

5.2.2. $^{12}\text{C}/^{13}\text{C}$

We use the total column density of CH_3OH and $^{13}\text{CH}_3\text{OH}$, including both the A and E type, to estimate the $^{12}\text{C}/^{13}\text{C}$ ratio in the CR. For CH_3OH , we obtain a total column density of $(2.0 \pm 0.4) \times 10^{18} \text{ cm}^{-2}$. Since the A/E abundance ratio is estimated to be 0.77 ± 0.33 (see Sect. 5.1), we simply assume the A/E abundance ratio to be unity for $^{13}\text{CH}_3\text{OH}$. We arrive at a total column density of $(3.2 \pm 0.6) \times 10^{16} \text{ cm}^{-2}$ for $^{13}\text{CH}_3\text{OH}$. This results in a $^{12}\text{C}/^{13}\text{C}$ ratio of 63 ± 17 , which agrees very well with the result (57 ± 14) based on CH_3OH transitions at higher frequencies (Persson et al. 2007), and the 50 ± 20 from H_2CS transitions (Tercero et al. 2010), while it is slightly higher than the value (43 ± 7) from CN lines (Savage et al. 2002). This confirms that the $^{12}\text{C}/^{13}\text{C}$ ratio in the CR is slightly smaller than the value (77 ± 7) in the local ISM and the solar value (89, Wilson & Rood 1994). Since the solar value represents the local interstellar medium 4.5 Gyrs ago, the difference may arise from the Galactic chemical evolution. Isotope selective photodissociation by UV photons can influence the $^{12}\text{C}/^{13}\text{C}$ ratio due to the difference in self-shielding of ^{12}C and ^{13}C (van Dishoeck & Black

1988; Savage et al. 2002; Milam et al. 2005, e.g.). ^{13}C is expected to be more easily photodissociated, which will result in a higher $^{12}\text{C}/^{13}\text{C}$ ratio, rather than a lower value that we obtained. This suggests that the effect cannot be significant influencing the $^{12}\text{C}/^{13}\text{C}$ ratio in Orion KL. Previous studies have also shown that chemical fractionation does not play a substantial role in influencing such ratios (e.g., Milam et al. 2005).

5.2.3. $^{14}\text{N}/^{15}\text{N}$

Here, we use the average column density of NH_3 and $^{15}\text{NH}_3$ to estimate the $^{14}\text{N}/^{15}\text{N}$ ratio in the HC. For NH_3 , we find that the column density obtained from the NH_3 ($J = K + 4$) transitions is nearly an order of magnitude higher than the values derived from the $J = K + 1$, $J = K + 2$, and $J = K + 3$ transitions, which may be due to different excitation conditions. For NH_3 ($J = K + 1$, $J = K + 2$, and $J = K + 3$) which share similar excitation conditions, we take a sigma-weighted average value of the three groups as the column density of NH_3 in the HC, which is estimated to be $(2.4 \pm 1.2) \times 10^{17} \text{ cm}^{-2}$. For $^{15}\text{NH}_3$, we take the average value derived from metastable and non-metastable transitions as the column density of $^{15}\text{NH}_3$, which is estimated to be $(2.4 \pm 0.3) \times 10^{15} \text{ cm}^{-2}$. This results in a $^{14}\text{N}/^{15}\text{N}$ ratio of 100 ± 51 , which is roughly consistent with the previous value of 170^{+140}_{-80} by Hermsen et al. (1985), but smaller than the 234 ± 47 derived from CN transitions (Adande & Ziurys 2012). This indicates that the $^{14}\text{N}/^{15}\text{N}$ ratio in the HC is smaller than the 450 ± 22 in the local ISM (Wilson & Rood 1994), the 1000 ± 200 in the prototypical starless cloud core L1544 (Bizzocchi et al. 2013), and the 300 ± 50 in Barnard 1 (Daniel et al. 2013). Fractionation in nitrogen is likely to play an important role in cold temperature (~ 10 K) regions (Rodgers & Charnley 2008), but the effect can be neglected in Orion KL due to its high temperature. Meanwhile, the $^{14}\text{N}/^{15}\text{N}$ ratio is found to be 361 ± 141 in the prototypical PDR region Orion Bar (Adande & Ziurys 2012). Thus, isotope selective photodissociation by UV photons should not affect the $^{14}\text{N}/^{15}\text{N}$ ratio a lot either. Since ^{15}N may originate from massive stars and is potentially destroyed in lower mass stars (e.g., Henkel et al. 1994; Wilson & Rood 1994; Chin et al. 1999; Wang et al. 2009), such an enhanced ^{15}N in the massive star-forming regions like Orion KL can be expected. Furthermore, our value is similar to the 111 ± 17 in the Large Magellanic Cloud (LMC) massive star-forming region N113, the ~ 100 in the LMC star-forming region N159HW and the value in the central region of NGC 4945 (Chin et al. 1999).

5.2.4. D/H

The deuterium fraction can be estimated from the ratio between the column densities of para- NH_3 and para- NH_2D , which have been discussed above and which are given in Table 3. We obtain a D/H ratio of $(8.3 \pm 4.5) \times 10^{-3}$. This is slightly higher than the value 3×10^{-3} from a previous deuterated ammonia (Walmsley et al. 1987) and a deuterated water study (Neill et al. 2013b), and is consistent with $(2 - 8) \times 10^{-3}$ from a study of other deuterated molecules (Neill et al. 2013a). This confirms that the D/H ratio for NH_3 is strongly affected by fractionation and is nearly two orders of magnitude higher than the abundance ratio in the interstellar medium and the primordial D/H ratio ($\sim 1.5 \times 10^{-5}$; e.g. Wilson & Rood 1994; Oliveira et al. 2003; Steigman 2007). Our value is also consistent with the ratio derived from HCN and DCN in the Orion Bar (Leurini et al. 2006; Parise et al. 2009). The enhancement could be attributed

to a fossil record of the deuteration of icy dust grain mantles (e.g., Roberts & Millar 2000; Millar 2005) or warm deuterium chemistry driven by CH_2D^+ (Parise et al. 2009).

5.3. A RADEX non-LTE model for $^{15}\text{NH}_3$

The inversion lines of ammonia are widely used as a Galactic and extragalactic molecular temperature tracer (e.g., Walmsley & Ungerechts 1983; Ho & Townes 1983; Mauersberger et al. 2003). However, the $^{14}\text{NH}_3$ transitions tend to become optically thick in high density regions containing hot cores. Furthermore, Orion KL contains several spatial components which make contributions to the $^{14}\text{NH}_3$ emission, resulting in difficulties of disentangling the different velocity components. On the contrary, the $^{15}\text{NH}_3$ transitions can be expected to be optically thin since the $^{14}\text{N}/^{15}\text{N}$ abundance ratio is of order 100 in Orion KL (see Sect. 5.2.3); the transitions of $^{15}\text{NH}_3$ only show one velocity component from the HC, thus they can be used to constrain the physical properties of the HC. Furthermore, $^{15}\text{NH}_3$ is proved to be a good tracer for high density environments such as ultra-compact HII regions (e.g., Wyrowski & Walmsley 1996). Here, we present a non-LTE analysis of $^{15}\text{NH}_3$ using the RADEX code (van der Tak et al. 2007), where the Einstein A coefficients of $^{15}\text{NH}_3$ are from the CDMS database while its collision rates are taken to be the same as those of $^{14}\text{NH}_3$ (Danby et al. 1988). A spherical cloud geometry is assumed. In the models, we do not account for any external radiation fields with the notable exception of the cosmic microwave background. However, infrared pumping is likely to affect the populations of $^{15}\text{NH}_3$ in the innermost regions of Orion KL. Therefore, spatial densities derived from purely collisional excitation can be considered as upper limits. To evaluate the models, we compare the observed line ratios with the modeled line ratios to minimize χ^2 which is defined as

$$\chi^2 = \sum_i \frac{(R_{\text{obs}(i)} - R_{\text{model}(i)})^2}{\sigma_{\text{obs}(i)}^2}, \quad (7)$$

where $R_{\text{obs}(i)}$, and $R_{\text{model}(i)}$ represent the observed and modeled line ratios, and $\sigma_{\text{obs}(i)}$ represents the uncertainty in $R_{\text{obs}(i)}$. We note that the uncertainties of observed line ratios, $(\frac{^{15}\text{NH}_3(2,2)}{^{15}\text{NH}_3(1,1)}, \frac{^{15}\text{NH}_3(4,4)}{^{15}\text{NH}_3(2,2)}, \frac{^{15}\text{NH}_3(5,5)}{^{15}\text{NH}_3(4,4)}, \frac{^{15}\text{NH}_3(3,2)}{^{15}\text{NH}_3(2,1)}, \text{etc.})$ should be free of calibration errors and beam dilution effects due to being close in frequency. Following previous χ^2 studies (e.g., Zhang et al. 2014), we only take solutions with a likelihood $L > 0.6$ into account, where L is defined as

$$L = \exp(-\chi^2/2)/L_{\text{max}}. \quad (8)$$

L_{max} is the maximum likelihood, corresponding to the minimum value of χ^2 .

Assuming that the HC has a typical size of $10''$ and a line width of 7 km s^{-1} , we obtain a velocity gradient of $350 \text{ km s}^{-1} \text{ pc}^{-1}$. Adopting a fixed para- $^{15}\text{NH}_3$ abundance of 8×10^{-9} (see Table 3), we arrive at a para- $^{15}\text{NH}_3$ abundance per velocity gradient $[X]/(dv/dr)$ of $2.3 \times 10^{-11} \text{ pc (km s}^{-1})^{-1}$. The modeled kinetic temperatures (T_{kin}) range from 10 to 500 K with a step size of 5 K. The H_2 number density $\log(\frac{n(\text{H}_2)}{\text{cm}^{-3}})$ varies from 3.0 to 9.0 with a step size of 0.1. We modeled the metastable para- $^{15}\text{NH}_3$ line ratios, and the results are shown in Fig. 8a and 8b. We can see that there are two groups of solutions: (1) a warmer group with $T_{\text{kin}} = 145 - 190 \text{ K}$ and $n_{\text{H}_2} = 10^{6.6} - 10^{7.1} \text{ cm}^{-3}$ and (2) a colder group with $T_{\text{kin}} = 95 - 150 \text{ K}$

and $n_{\text{H}_2} = 10^{7.2} - 10^{8.0} \text{ cm}^{-3}$. The first group of solutions is roughly consistent with previous studies (Genzel & Stutzki 1989; Wang et al. 2010; Goddi et al. 2011). The second group of solutions indicates that the $^{15}\text{NH}_3$ emission region may have a colder kinetic temperature in an even denser region. This can be expected since the HC in Orion KL is thought to be externally heated (Bally et al. 2011; Zapata et al. 2011; Nissen et al. 2012), which may result in an inner denser region with a lower kinetic temperature. On the other hand, we find that the line ratio $\frac{^{15}\text{NH}_3(5,5)}{^{15}\text{NH}_3(4,4)}$ is only sensitive to kinetic temperature in a region with a spatial density less than 10^7 cm^{-3} . When densities are higher than 10^7 cm^{-3} at the abundance given above, these lines become optically thicker, and thus the ratios are no longer a good kinetic temperature tracer. Including the non-metastable para- $^{15}\text{NH}_3$ in the modeling (see Figs. 8c and 8d), we obtain a solution with $T_{\text{kin}} = 95 - 145 \text{ K}$ and $n_{\text{H}_2} = 10^{7.4} - 10^{8.0} \text{ cm}^{-3}$, similar to the second group of solutions based on metastable transitions, which is supportive of a colder and denser region existing in the HC.

We also modeled the line ratios from ortho- $^{15}\text{NH}_3$. Since the ortho-to-para ratio is found to be around unity (see Sect. 5.1), the ortho- $^{15}\text{NH}_3$ abundance per velocity gradient is assumed to be the same as that for para- $^{15}\text{NH}_3$. With the line ratios $\frac{^{15}\text{NH}_3(6,6)}{^{15}\text{NH}_3(3,3)}$ and $\frac{^{15}\text{NH}_3(4,3)}{^{15}\text{NH}_3(3,3)}$, we use the same method to model these ratios from ortho- $^{15}\text{NH}_3$, and the results are shown in Figs. 8e and 8f. We find that ortho- $^{15}\text{NH}_3$ emission is likely to come from a region with $T_{\text{kin}} = 60 - 105 \text{ K}$ and $n_{\text{H}_2} = 10^{8.0} - 10^{8.6} \text{ cm}^{-3}$, which is indicative of an even colder and denser region. This further suggests that the HC is externally heated.

The $^{15}\text{NH}_3$ abundance calculated with the LTE column density and an assumed H_2 column density may have a large uncertainty, which probably results in a large error in T_{kin} and $n(\text{H}_2)$. Thus, we carried out another RADEX modelling with two different $^{15}\text{NH}_3$ abundances of 8×10^{-10} and 8×10^{-8} . The results are shown in Fig. 9. By comparison with Fig. 8, we find that the derived kinetic temperature depends little on the assumed $^{15}\text{NH}_3$ abundances while the modeled spatial density depends strongly on the assumed $^{15}\text{NH}_3$ abundances. Fig. 9 also shows that denser region has a lower kinetic temperature even when changing abundances. Therefore, external heating of the HC still holds for the $^{15}\text{NH}_3$ abundances ranging from 8×10^{-10} to 8×10^{-8} .

As mentioned above, an external radiation field is not taken into account in this modeling. In principle, infrared pumping can affect the population of ammonia via vibrationally excited lines (e.g., see Fig. 1 of Mauersberger et al. 1988). When the infrared radiation field becomes very intense, the population can be significantly affected, and such effect may have led to a large number (~ 20) of NH_3 masers in W51-IRS2 (Henkel et al. 2013). The lack of NH_3 masers and T_{kin} values below 200 K indicate that vibrational excitation of ammonia does not play a major role for the HC in Orion KL. However, our modeling without excitation by the infrared radiation field only gives upper limits for the spatial density.

6. Summary and Conclusions

We have carried out a 1.3 cm spectral line survey toward Orion KL with the Effelsberg-100 m telescope. We detect a total of 261 lines, yielding an average line density of about 23 spectral features per GHz above 3σ (a typical value of 3σ is 15 mJy). Among them, 164 lines are radio recombination lines (RRLs) from hydrogen, helium and carbon, 97 lines can be assigned to 13 different molecules including rare isotopologues. A total of

23 molecular transitions from species known to exist in Orion KL are detected for the first time in the interstellar medium. Non-metastable $^{15}\text{NH}_3$ transitions are detected in Orion KL for the first time. An analysis of line widths suggests that the bulk of the discrepancy between observed line widths of hydrogen and helium RRLs originates from their thermal contributions. The intensity ratios of RRL pairs with different Δn from the same atom at neighbouring frequencies are consistent with the local thermodynamic equilibrium (LTE) ratios, suggesting that the LTE deviations are very small in this band. The origin of molecules detected by our survey is discussed according to observed lines and ALMA images. A narrow feature is found in SO_2 ($8_{1,7} - 7_{2,6}$), but not in other SO_2 transitions, possibly suggesting the presence of a maser line. Column densities and fractional abundances relative to H_2 are estimated for 12 molecules with rotational diagrams. We find that the four classes of non-metastable NH_3 from $J = K + 1$ to $J = K + 4$ have different excitation conditions and metastable $^{15}\text{NH}_3$ has a higher excitation temperature than non-metastable $^{15}\text{NH}_3$. The elemental and isotopic abundance ratios are calculated: $\text{He}^+/\text{H}^+ = (8.7 \pm 0.7)\%$ derived from the ratios between helium RRLs and hydrogen RRLs; $^{12}\text{C}/^{13}\text{C} = 63 \pm 17$ from $^{12}\text{CH}_3\text{OH}/^{13}\text{CH}_3\text{OH}$; $^{14}\text{N}/^{15}\text{N} = 100 \pm 51$ from $^{14}\text{NH}_3/^{15}\text{NH}_3$; $\text{D}/\text{H} = (8.3 \pm 4.5) \times 10^{-3}$ from $\text{NH}_2\text{D}/\text{NH}_3$. The dispersion of the He/H ratios derived from $\text{H}\alpha/\text{He}\alpha$ pairs to $\text{H}\delta/\text{He}\delta$ pairs is very small, which is consistent with theoretical predictions that the departure coefficients b_n factors for hydrogen and helium are nearly identical. A non-LTE model of $^{15}\text{NH}_3$ neglecting external radiation fields and a likelihood analysis supports the view that the hot core is externally heated.

ACKNOWLEDGMENTS

We would like to thank an anonymous referee for a helpful report that led to improvements in the paper. We greatly thank Christian P. Endres for providing $^{15}\text{NH}_3$ spectroscopic information. We wish to thank Zhiyu Zhang for discussions of the χ^2 analysis and appreciate the assistance of the Effelsberg-100m operators during the observations. Y. Gong acknowledges support by the MPG-CAS Joint Doctoral Promotion Programme (DPP), and NSFC Grants 11127903, 11233007 and 10973040. S. Thorwirth gratefully acknowledges funding by the Deutsche Forschungsgemeinschaft (DFG) through grant TH 1301/3-2. S. Spezzano wishes to thank the DFG SFB956 and the “Fondazione Angelo della Riccia” for funding. This paper makes use of the following ALMA data: ADS/JAO.ALMA#2011.0.00009.SV. ALMA is a partnership of ESO (representing its member states), NSF (USA) and NINS (Japan), together with NRC (Canada) and NSC and ASIAA (Taiwan), in cooperation with the Republic of Chile. The Joint ALMA Observatory is operated by ESO, AUI/NRAO and NAOJ. This research has made use of NASA’s Astrophysics Data System.

References

- Adande, G. R. & Ziurys, L. M. 2012, *ApJ*, 744, 194
- Baldwin, J. A., Ferland, G. J., Martin, P. G., et al. 1991, *ApJ*, 374, 580
- Bally, J., Cunningham, N. J., Moeckel, N., et al. 2011, *ApJ*, 727, 113
- Bell, M. B., Avery, L. W., MacLeod, J. M., & Vallée, J. P. 2011, *Ap&SS*, 333, 377
- Bell, M. B., Avery, L. W., & Watson, J. K. G. 1993, *ApJS*, 86, 211
- Beuther, H. & Nissen, H. D. 2008, *ApJ*, 679, L121
- Beuther, H., Zhang, Q., Greenhill, L. J., et al. 2005, *ApJ*, 632, 355
- Bizzocchi, L., Caselli, P., Leonardo, E., & Dore, L. 2013, *A&A*, 555, A109
- Blake, G. A., Masson, C. R., Phillips, T. G., & Sutton, E. C. 1986, *ApJS*, 60, 357
- Blake, G. A., Mundy, L. G., Carlstrom, J. E., et al. 1996, *ApJ*, 472, L49
- Boesgaard, A. M. & Steigman, G. 1985, *ARA&A*, 23, 319

- Brocklehurst, M. & Seaton, M. J. 1972, *MNRAS*, 157, 179
- Cernicharo, J., Guélin, M., & Kahane, C. 2000, *A&AS*, 142, 181
- Cernicharo, J., Tercero, B., Fuente, A., et al. 2013, *ApJ*, 771, L10
- Charnley, S. B. 1997, *ApJ*, 481, 396
- Chin, Y.-n., Henkel, C., Langer, N., & Mauersberger, R. 1999, *ApJ*, 512, L143
- Churchwell, E., Mezger, P. G., & Huchtmeier, W. 1974, *A&A*, 32, 283
- Comito, C., Schilke, P., Phillips, T. G., et al. 2005, *ApJS*, 156, 127
- Crockett, N. R., Bergin, E. A., Neill, J. L., et al. 2014, *ApJ*, 787, 112
- Danby, G., Flower, D. R., Valiron, P., Schilke, P., & Walmsley, C. M. 1988, *MNRAS*, 235, 229
- Daniel, F., Gérin, M., Roueff, E., et al. 2013, *A&A*, 560, A3
- Di Francesco, J., Johnstone, D., Kirk, H., MacKenzie, T., & Ledwosinska, E. 2008, *ApJS*, 175, 277
- Esplughes, G. B., Cernicharo, J., Viti, S., et al. 2013a, *A&A*, 559, A51
- Esplughes, G. B., Tercero, B., Cernicharo, J., et al. 2013b, *A&A*, 556, A143
- Favre, C., Despois, D., Brouillet, N., et al. 2011, *A&A*, 532, A32
- Feng, S., Beuther, H., Henning, T., et al. 2015, *ArXiv e-prints*
- Frayer, D. T., Maddalena, R. J., Meijer, M., et al. 2015, *AJ*, 149, 162
- Friedel, D. N. & Snyder, L. E. 2008, *ApJ*, 672, 962
- Genzel, R., Ho, P. T. P., Bieging, J., & Downes, D. 1982, *ApJ*, 259, L103
- Genzel, R., Reid, M. J., Moran, J. M., & Downes, D. 1981, *ApJ*, 244, 884
- Genzel, R. & Stutzki, J. 1989, *ARA&A*, 27, 41
- Goddi, C., Greenhill, L. J., Humphreys, E. M. L., Chandler, C. J., & Matthews, L. D. 2011, *ApJ*, 739, L13
- Goddi, C., Greenhill, L. J., Humphreys, E. M. L., et al. 2009, *ApJ*, 691, 1254
- Goicoechea, J. R., Chavarría, L., Cernicharo, J., et al. 2015, *ApJ*, 799, 102
- Gong, Y., Henkel, C., Spezzano, S., et al. 2015, *A&A*, 574, A56
- Greaves, J. S. & White, G. J. 1991, *A&AS*, 91, 237
- Greenhill, L. J., Gwinn, C. R., Schwartz, C., Moran, J. M., & Diamond, P. J. 1998, *Nature*, 396, 650
- Henkel, C., Wilson, T. L., Asiri, H., & Mauersberger, R. 2013, *A&A*, 549, A90
- Henkel, C., Wilson, T. L., Langer, N., Chin, Y.-N., & Mauersberger, R. 1994, in *Lecture Notes in Physics*, Berlin Springer Verlag, Vol. 439, The Structure and Content of Molecular Clouds, ed. T. L. Wilson & K. J. Johnston, 72–88
- Herbst, E. & van Dishoeck, E. F. 2009, *ARA&A*, 47, 427
- Hermesen, W., Wilson, T. L., Walmsley, C. M., & Batrla, W. 1985, *A&A*, 146, 134
- Hermesen, W., Wilson, T. L., Walmsley, C. M., & Henkel, C. 1988, *A&A*, 201, 285
- Hirota, T., Kim, M. K., Kurono, Y., & Honma, M. 2015, *ApJ*, 801, 82
- Ho, P. T. P. & Townes, C. H. 1983, *ARA&A*, 21, 239
- Hollis, J. M., Jewell, P. R., Lovas, F. J., Remijan, A., & Møllendal, H. 2004, *ApJ*, 610, L21
- Jewell, P. R., Hollis, J. M., Lovas, F. J., & Snyder, L. E. 1989, *ApJS*, 70, 833
- Jiang, Z., Tamura, M., Fukagawa, M., et al. 2005, *Nature*, 437, 112
- Johansson, L. E. B., Andersson, C., Ellerd, J., et al. 1984, *A&A*, 130, 227
- Kaifu, N., Ohishi, M., Kawaguchi, K., et al. 2004, *PASJ*, 56, 69
- Kalenskii, S. V., Slysh, V. I., Goldsmith, P. F., & Johansson, L. E. B. 2004, *ApJ*, 610, 329
- Klein, B., Hochgürtel, S., Krämer, I., et al. 2012, *A&A*, 542, L3
- Lee, C. W. & Cho, S.-H. 2002, *Journal of Korean Astronomical Society*, 35, 187
- Lee, C. W., Cho, S.-H., & Lee, S.-M. 2001, *ApJ*, 551, 333
- Lerate, M. R., Barlow, M. J., Swinyard, B. M., et al. 2006, *MNRAS*, 370, 597
- Leurini, S., Rolfs, R., Thorwirth, S., et al. 2006, *A&A*, 454, L47
- López, A., Tercero, B., Kisel, Z., et al. 2014, *A&A*, 572, A44
- Lovas, F. J. & Dragoset, R. A. 2004, *J. Phys. Chem. Ref. Data*, 33, 177
- Mangum, J. G. & Wootten, A. 1993, *ApJS*, 89, 123
- Matsakis, D. N., Wright, M. C. H., Townes, C. H., et al. 1980, *ApJ*, 236, 481
- Mauersberger, R., Henkel, C., Weiß, A., Peck, A. B., & Hagiwara, Y. 2003, *A&A*, 403, 561
- Mauersberger, R., Henkel, C., & Wilson, T. L. 1988, *A&A*, 205, 235
- Menten, K. M. & Reid, M. J. 1995, *ApJ*, 445, L157
- Menten, K. M., Reid, M. J., Forbrich, J., & Brunthaler, A. 2007, *A&A*, 474, 515
- Menten, K. M., Walmsley, C. M., Henkel, C., & Wilson, T. L. 1986, *A&A*, 157, 318
- Menten, K. M., Walmsley, C. M., Henkel, C., & Wilson, T. L. 1988a, *A&A*, 198, 267
- Menten, K. M., Walmsley, C. M., Henkel, C., & Wilson, T. L. 1988b, *A&A*, 198, 253
- Mezger, P. G. & Henderson, A. P. 1967, *ApJ*, 147, 471
- Milam, S. N., Savage, C., Brewster, M. A., Ziurys, L. M., & Wyckoff, S. 2005, *ApJ*, 634, 1126
- Millar, T. J. 2005, *Astronomy and Geophysics*, 46, 29
- Müller, H. S. P., Schlöder, F., Stutzki, J., & Winnewisser, G. 2005, *Journal of Molecular Structure*, 742, 215
- Natta, A., Walmsley, C. M., & Tielens, A. G. G. M. 1994, *ApJ*, 428, 209
- Neill, J. L., Crockett, N. R., Bergin, E. A., Pearson, J. C., & Xu, L.-H. 2013a, *ApJ*, 777, 85
- Neill, J. L., Wang, S., Bergin, E. A., et al. 2013b, *ApJ*, 770, 142
- Nissen, H. D., Cunningham, N. J., Gustafsson, M., et al. 2012, *A&A*, 540, A119
- Ohishi, M., Kaifu, N., Suzuki, H., & Morimoto, M. 1986, *Ap&SS*, 118, 405
- Olive, K. A. & Skillman, E. D. 2004, *ApJ*, 617, 29
- Oliveira, C. M., Hébrard, G., Howk, J. C., et al. 2003, *ApJ*, 587, 235
- Olofsson, A. O. H., Persson, C. M., Koning, N., et al. 2007, *A&A*, 476, 791
- Ott, M., Witzel, A., Quirrenbach, A., et al. 1994, *A&A*, 284, 331
- Parise, B., Leurini, S., Schilke, P., et al. 2009, *A&A*, 508, 737
- Peimbert, M., Rodriguez, L. F., Bania, T. M., Rood, R. T., & Wilson, T. L. 1992, *ApJ*, 395, 484
- Persson, C. M., Olofsson, A. O. H., Koning, N., et al. 2007, *A&A*, 476, 807
- Pickett, H. M., Poynter, R. L., Cohen, E. A., et al. 1998, *J. Quant. Spec. Radiat. Transf.*, 60, 883
- Plambeck, R. L., Wright, M. C. H., Friedel, D. N., et al. 2009, *ApJ*, 704, L25
- Quireza, C., Rood, R. T., Bania, T. M., Balser, D. S., & Maciel, W. J. 2006, *ApJ*, 653, 1226
- Remijan, A. J., Hollis, J. M., Lovas, F. J., et al. 2008a, *ApJ*, 675, L85
- Remijan, A. J., Leigh, D. P., Markwick-Kemper, A. J., & Turner, B. E. 2008b, *ArXiv e-prints*
- Roberts, H. & Millar, T. J. 2000, *A&A*, 361, 388
- Rodgers, S. D. & Charnley, S. B. 2008, *MNRAS*, 385, L48
- Salem, M. & Brocklehurst, M. 1979, *ApJS*, 39, 633
- Salter, C. J., Ghosh, T., Catinella, B., et al. 2008, *AJ*, 136, 389
- Savage, C., Apponi, A. J., Ziurys, L. M., & Wyckoff, S. 2002, *ApJ*, 578, 211
- Schilke, P., Benford, D. J., Hunter, T. R., Lis, D. C., & Phillips, T. G. 2001, *ApJS*, 132, 281
- Schilke, P., Groesbeck, T. D., Blake, G. A., & Phillips, T. G. 1997, *ApJS*, 108, 301
- Serabyn, E. & Weisstein, E. W. 1995, *ApJ*, 451, 238
- Shuping, R. Y., Morris, M., & Bally, J. 2004, *AJ*, 128, 363
- Steigman, G. 2007, *Annual Review of Nuclear and Particle Science*, 57, 463
- Storey, P. J. & Hummer, D. G. 1995, *MNRAS*, 272, 41
- Sutton, E. C., Blake, G. A., Masson, C. R., & Phillips, T. G. 1985, *ApJS*, 58, 341
- Sutton, E. C., Peng, R., Danchi, W. C., et al. 1995, *ApJS*, 97, 455
- Takano, S., Nakai, N., & Kawaguchi, K. 2002, *PASJ*, 54, 195
- Tercero, B., Cernicharo, J., Pardo, J. R., & Goicoechea, J. R. 2010, *A&A*, 517, A96
- Tercero, B., Kleiner, I., Cernicharo, J., et al. 2013, *ApJ*, 770, L13
- Tercero, B., Vincent, L., Cernicharo, J., Viti, S., & Marcelino, N. 2011, *A&A*, 528, A26
- Terzian, Y. & Parrish, A. 1970, *Astrophys. Lett.*, 5, 261
- Thorwirth, S. 2001, PhD thesis, I. Physikalisches Institut Universität zu Köln Zülpicher Str. 77 50937 Köln Germany
- Thorwirth, S., Wyrowski, F., Schilke, P., et al. 2003, *ApJ*, 586, 338
- Thum, C., Mezger, P. G., & Pankonin, V. 1980, *A&A*, 87, 269
- Turner, B. E. 1989, *ApJS*, 70, 539
- Turner, B. E. 1991, *ApJS*, 76, 617
- van der Tak, F. F. S., Black, J. H., Schöier, F. L., Jansen, D. J., & van Dishoeck, E. F. 2007, *A&A*, 468, 627
- van Dishoeck, E. F. & Black, J. H. 1988, *ApJ*, 334, 771
- Walmsley, C. M., Hermesen, W., Henkel, C., Mauersberger, R., & Wilson, T. L. 1987, *A&A*, 172, 311
- Walmsley, C. M. & Ungerechts, H. 1983, *A&A*, 122, 164
- Wang, K.-S., Kuan, Y.-J., Liu, S.-Y., & Charnley, S. B. 2010, *ApJ*, 713, 1192
- Wang, M., Chin, Y.-N., Henkel, C., Whiteoak, J. B., & Cunningham, M. 2009, *ApJ*, 690, 580
- Wang, S., Bergin, E. A., Crockett, N. R., et al. 2011, *A&A*, 527, A95
- White, G. J., Araki, M., Greaves, J. S., Ohishi, M., & Higginbottom, N. S. 2003, *A&A*, 407, 589
- Wilson, T. L., Filges, L., Codella, C., Reich, W., & Reich, P. 1997, *A&A*, 327, 1177
- Wilson, T. L., Gaume, R. A., Gensheimer, P., & Johnston, K. J. 2000, *ApJ*, 538, 665
- Wilson, T. L., Henkel, C., Huttemeister, S., et al. 1993, *A&A*, 276, L29
- Wilson, T. L., Rohlfs, K., & Hüttemeister, S. 2009, *Tools of Radio Astronomy* (Springer-Verlag)
- Wilson, T. L. & Rood, R. 1994, *ARA&A*, 32, 191
- Wright, M. C. H., Plambeck, R. L., & Wilner, D. J. 1996, *ApJ*, 469, 216
- Wu, Y., Liu, T., & Qin, S.-L. 2014, *ApJ*, 791, 123
- Wynn-Williams, C. G., Genzel, R., Becklin, E. E., & Downes, D. 1984, *ApJ*, 281, 172
- Wyrowski, F., Schilke, P., Hofner, P., & Walmsley, C. M. 1997, *ApJ*, 487, L171
- Wyrowski, F. & Walmsley, C. M. 1996, *A&A*, 314, 265
- Zapata, L. A., Schmid-Burgk, J., & Menten, K. M. 2011, *A&A*, 529, A24
- Zhang, Z.-Y., Henkel, C., Gao, Y., et al. 2014, *A&A*, 568, A122
- Zinchenko, I., Henkel, C., & Mao, R. Q. 2000, *A&A*, 361, 1079
- Ziurys, L. M. & McGonagle, D. 1993, *ApJS*, 89, 155

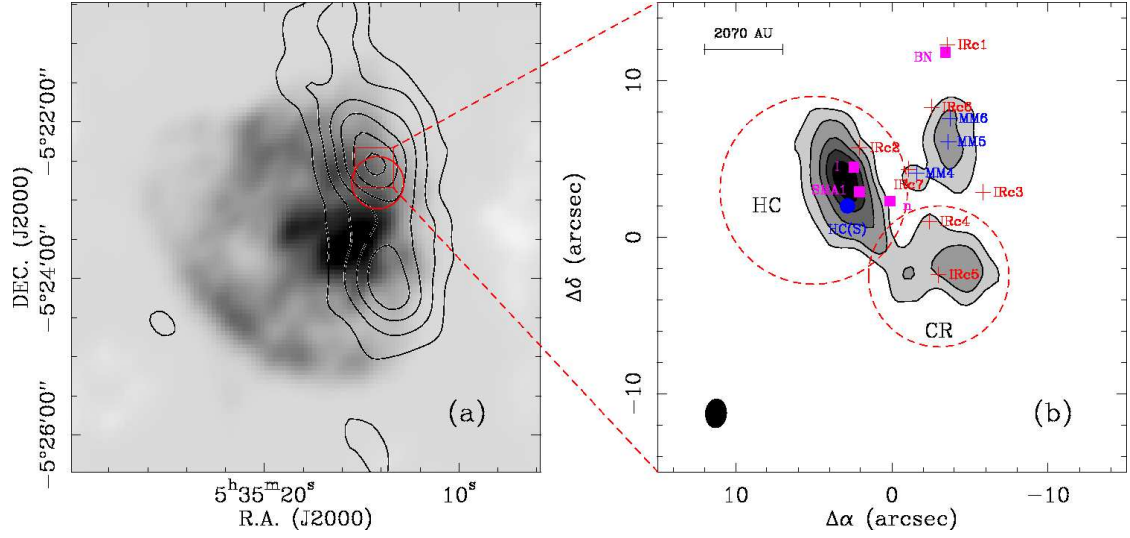


Fig. 1. (a) The SCUBA-850 μm dust emission (contours) overlaid on the 6 cm VLA continuum image. The contours correspond to 5, 10, 20, 40, 80, 160 Jy beam^{-1} . The red circle represents the Effelsberg FWHM beamsize (40''). The red box represents the mapped region of Fig. 1b. (b) Continuum map of Orion KL at 230 GHz from the ALMA-SV line survey modified from Figure 8 of Crockett et al. (2014). The contour levels are 10%, 20%, 40%, 60%, 80% of the peak intensity of 1.406 Jy beam^{-1} . The positions of source n, source I, SMA1 and the BN object are indicated by the purple squares. The position of the hot core south (HC(S)) is indicated by the blue circle. The positions of Infrared sources IRc1, IRc2, IRc3, IRc4, IRc5, IRc6, and IRc7 are marked by red crosses. Blue crosses indicate millimeter wave continuum sources. The approximate positions of the compact ridge and the hot core are indicated by the red dashed circles and the acronyms CR and HC. (these sources are described in more details in Sect. 3.) The physical scale is given by the horizontal bar. The synthesized beam is shown in the lower left of the panel. The reference point corresponds to $(\alpha_{\text{J2000}}, \delta_{\text{J2000}}) = (05^{\text{h}}35^{\text{m}}14.350^{\text{s}}, -05^{\circ}22'35.00'')$.

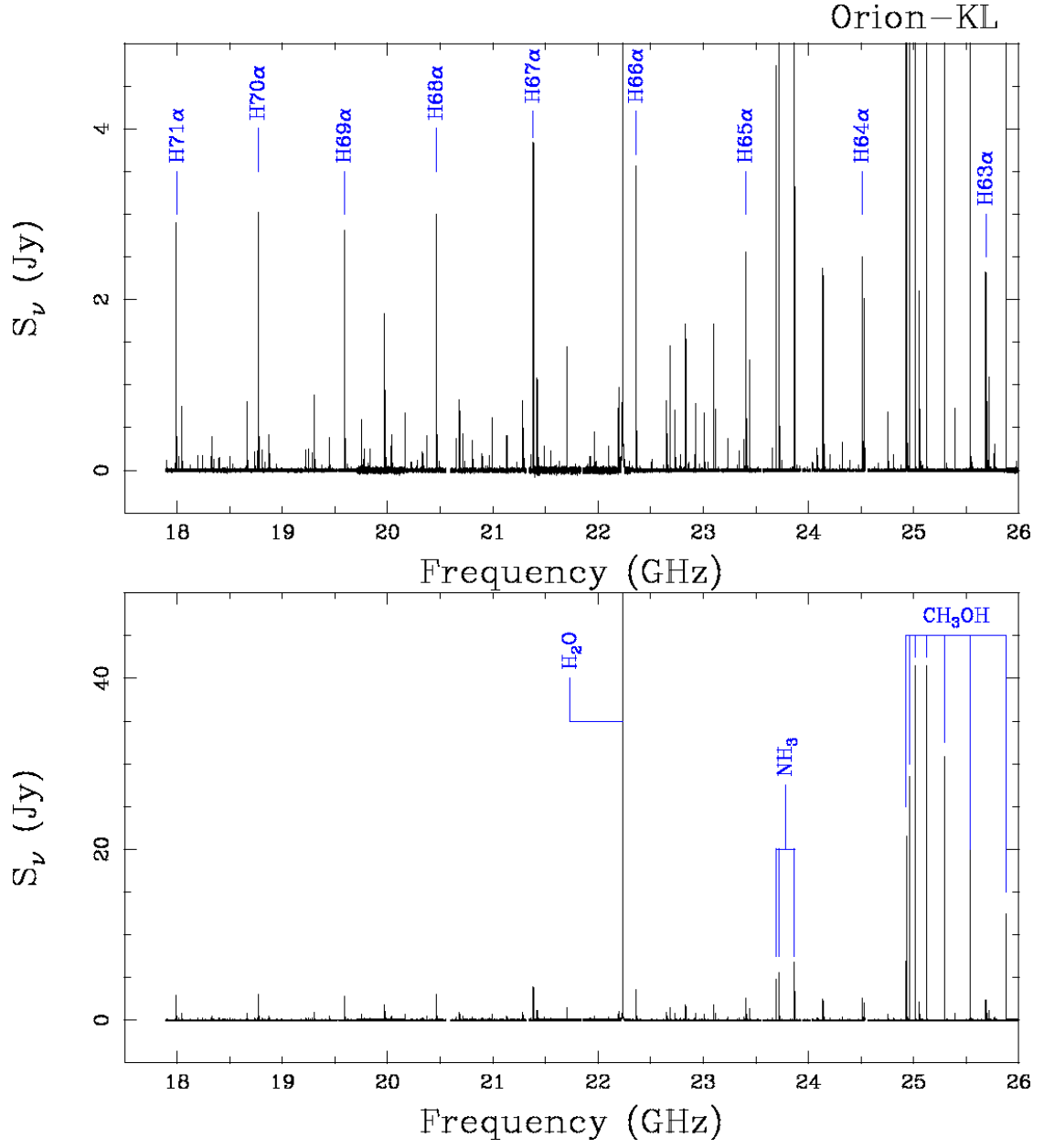


Fig. 2. Overview of the 1.3 cm line survey toward Orion KL with strong lines marked. The displayed frequency scale is based on the Local Standard of Rest velocity 0 km s^{-1} .

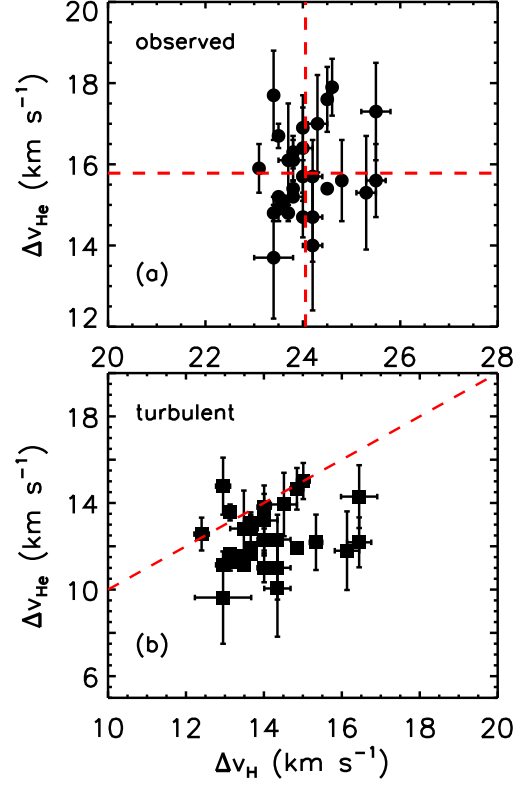


Fig. 3. (a) The relationship between the observed line widths of hydrogen (abszissa) and helium (ordinate) RRLs. The red dashed lines represent the unweighted mean values of observed line widths of hydrogen and helium RRLs, respectively. (b) The relationship between the turbulent line widths derived from hydrogen and helium RRLs. The red dashed line connects points where turbulent line widths for hydrogen and helium are equal.

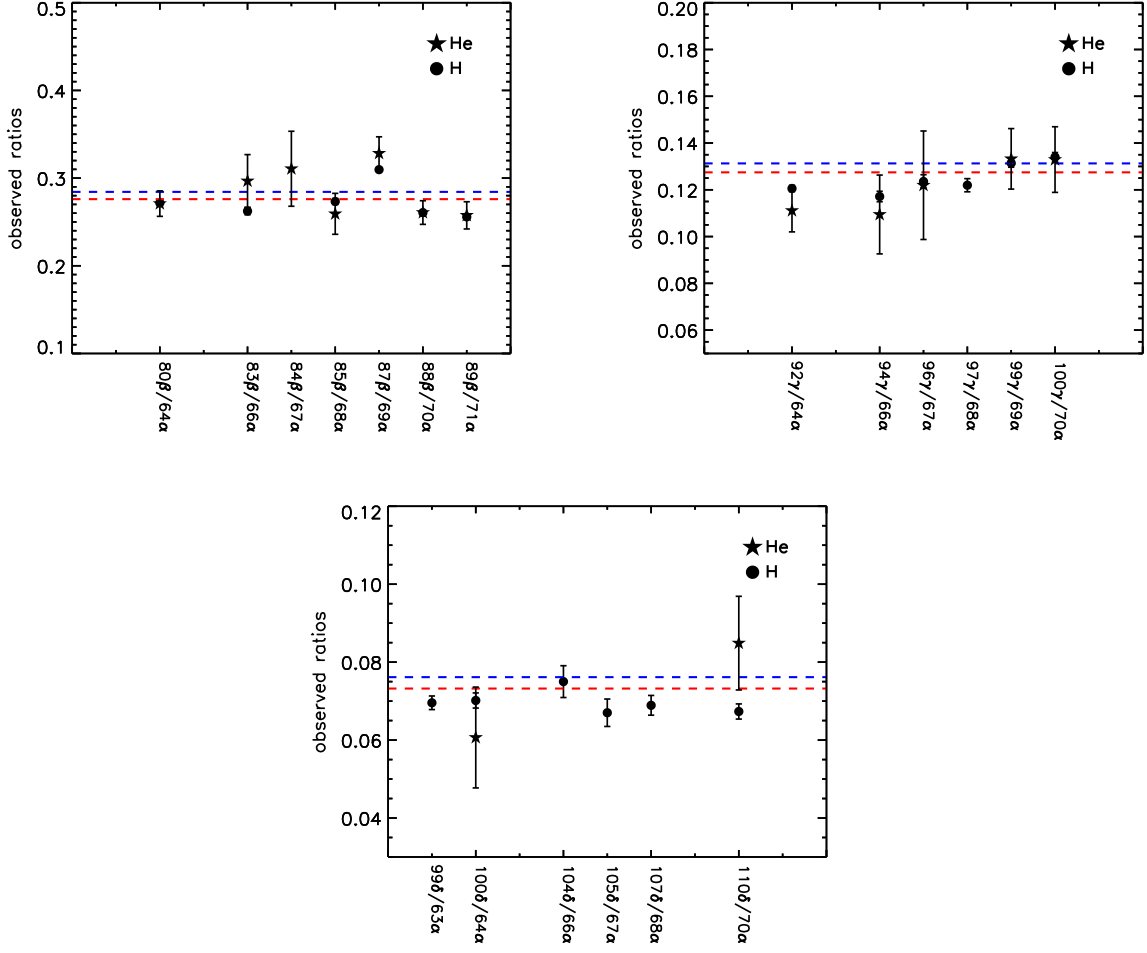


Fig. 4. Comparison of observed and LTE ratios of recombination lines. The observed ratios for hydrogen and helium RRLs are marked with circles and pentagrams. The red dashed lines represent the LTE ratios while the blue dashed lines represent the LTE ratios with the departure coefficients b_n corrected. Each ratio is given below the respective abscissa.

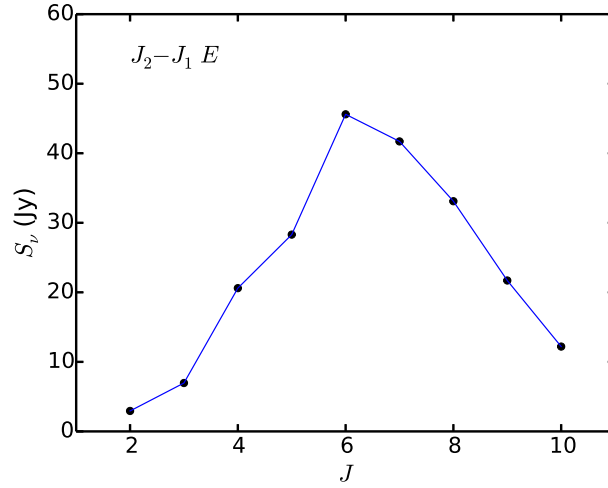


Fig. 5. Observed peak intensities of CH_3OH ($J_2 - J_1 E$) masers as a function of rotational quantum number J .

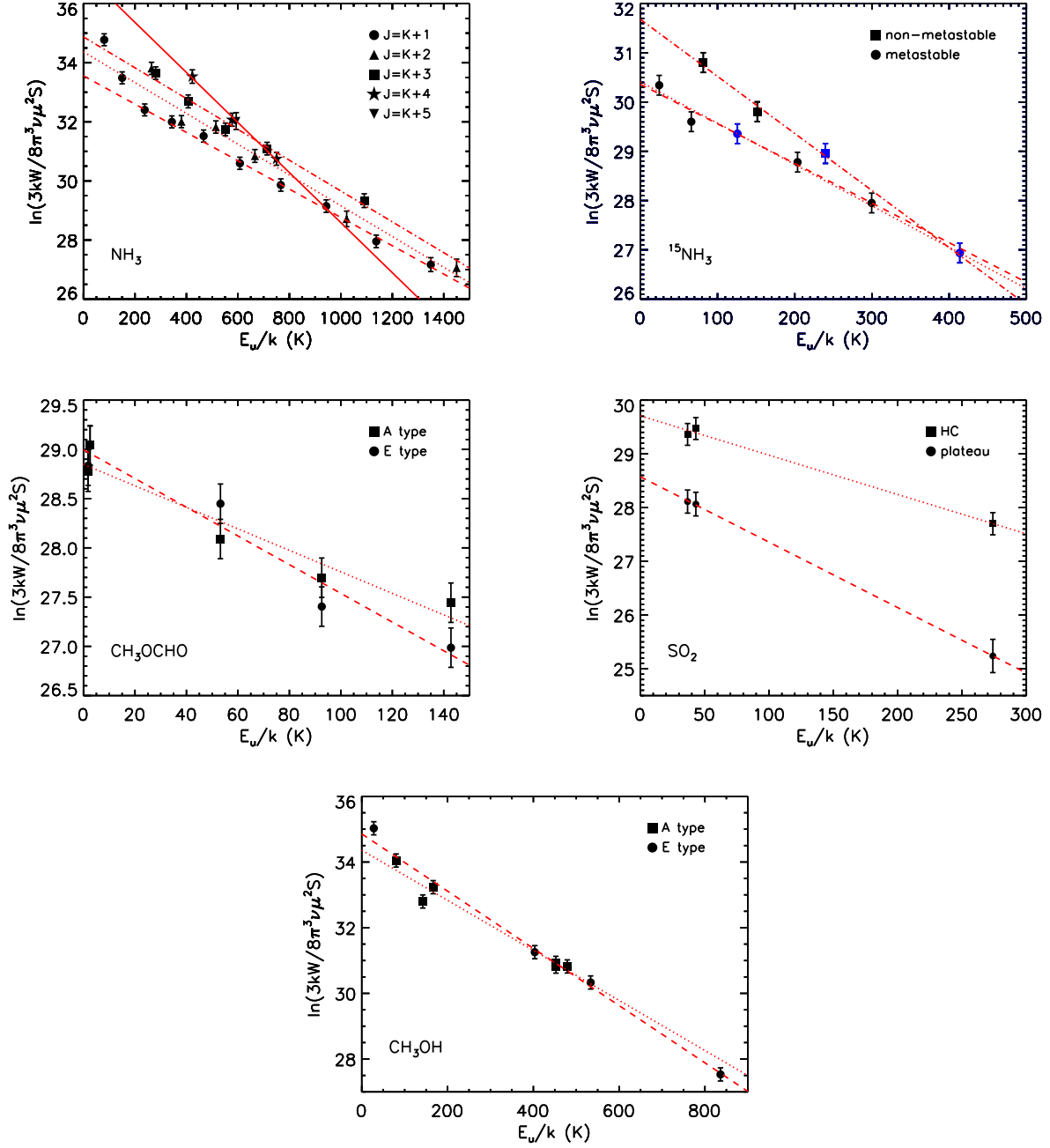


Fig. 6. Rotational diagrams for NH₃, ¹⁵NH₃, CH₃OCHO, SO₂, and CH₃OH. The circles and squares are explained by the legends in the upper right of each panel. A calibration error of 20% has been included in the error bars. In the NH₃ panel, least-square fits to $J + 1$, $J + 2$, $J + 3$, and $J + 4$ are indicated by a red dashed line, a red dotted line, a red dot-dashed line, and a red solid line. In the ¹⁵NH₃ panel, the para and ortho transitions of ¹⁵NH₃ are black and blue; the least-square fits to para and ortho metastable ¹⁵NH₃ transitions and non-metastable ¹⁵NH₃ transitions are indicated by a red dashed line, a red dotted line and a red dot-dashed line, respectively. In the CH₃OH and CH₃OCHO panels, the dashed and dotted lines represent fits to A type and E type transitions, respectively. In the SO₂ panel, dashed and dotted lines represent fits to its plateau and its HC component.

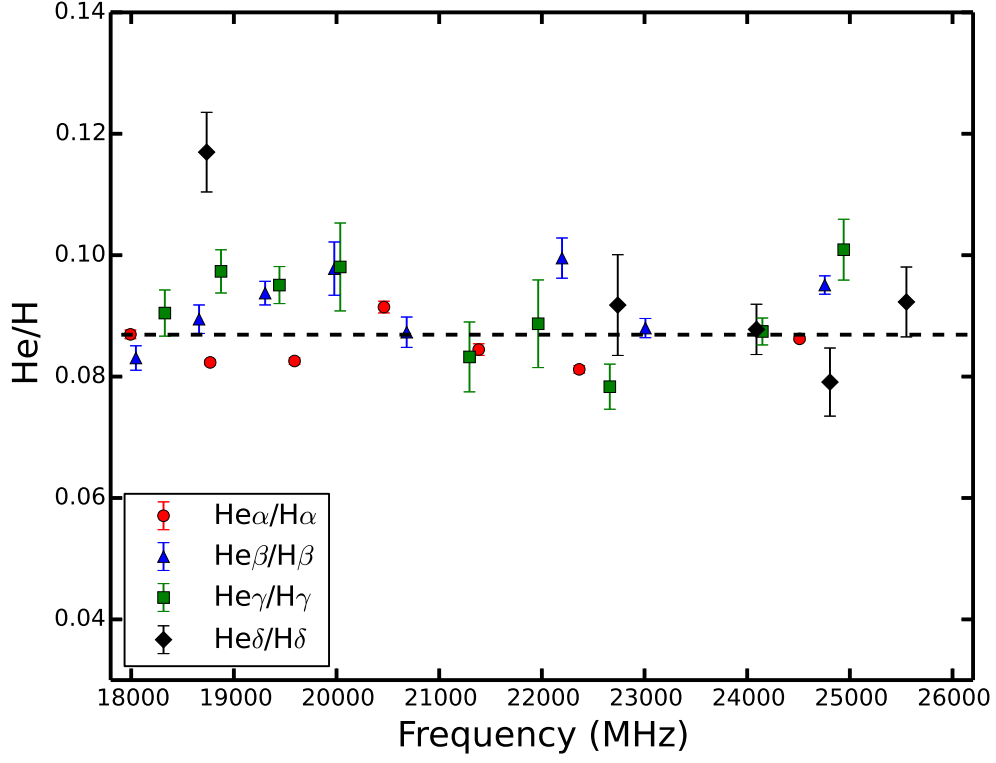


Fig. 7. He^+/H^+ abundance ratios derived from RRLs as a function of rest frequency. The abundance ratios derived from $\text{He}\alpha/\text{H}\alpha$, $\text{He}\beta/\text{H}\beta$, $\text{He}\gamma/\text{H}\gamma$ and $\text{He}\delta/\text{H}\delta$ are marked with red filled circles, blue filled triangles, green filled squares and black filled diamonds, respectively. The dashed line represents the sigma-weighted mean value of He^+/H^+ abundance ratios.

Table 2. Lines detected in the survey of Orion-KL.

Rest frequency (MHz)	Transition	E_u/k (K)	notes
17901.6	H120 ϵ		
17978.5	H127 ζ		
17992.6	H71 α		
17999.9	He71 α		1
18001.5	C71 α		1
18017.3	NH ₃ (7,3)	750	
18019.0	H139 θ		
18045.9	H89 β		
18053.2	He89 β		
18123.4	H133 η		
18196.2	HC ₃ N (2–1)	1	
18241.7	H111 δ		
18327.5	H101 γ		
18335.0	He101 γ		
18347.5	H119 ϵ		
18391.5	NH ₃ (6,1)	593	
18398.0	CH ₃ CN (1 ₀ –0 ₀)	1	2
18400.1	H126 ζ		2, 3
18402.7	H138 θ		3
18499.3	NH ₃ (9,6)	1091	
18528.0	H132 η		
18661.1	H88 β		
18668.7	He88 β		
18734.9	H110 δ		
18742.5	He110 δ		
18769.2	H70 α		
18776.8	He70 α		1
18778.5	C70 α		1
18807.9	NH ₂ D (3 _{1,3} S–3 _{0,3} A)	94	4
18808.4	H118 ϵ		4
18808.5	NH ₃ (8,5)	893	4
18835.1	H125 ζ		
18859.0	H142 ι		
18874.8	H100 γ		
18882.5	He100 γ		
18884.6	NH ₃ (6,2)	578	
18944.7	H131 η		
19218.4	NH ₃ (7,4)	713	
19246.1	H109 δ		
19283.8	H124 ζ		5
19284.8	H117 ϵ		5
19304.7	H87 β		
19312.6	He87 β		
19374.0	H130 η		
19444.0	H99 γ		
19451.9	He99 γ		
19591.1	H69 α		
19599.1	He69 α		1
19600.9	C69 α		1
19621.6	H135 θ		
19654.0	H140 ι		
19757.5	NH ₃ (6,3)	551	
19776.0	H108 δ		6
19777.4	H116 ϵ		6
19816.4	H129 η		
19838.3	NH ₃ (5,1)	423	
19967.4	CH ₃ OH (2 ₁ –3 ₀ E)	28	
19978.2	H86 β		
19986.3	He86 β		

Table 2. continued.

Rest frequency (MHz)	Transition	E_u/k (K)	notes
20036.3	H98 γ		
20044.5	He98 γ		
20051.7	H134 θ		
20171.1	CH ₃ OH (11 ₁ –10 ₂ A ⁺)	166	
20225.1	H122 ζ		
20272.4	H128 η		
20287.0	H115 ϵ		
20325.5	H107 δ		
20333.8	He107 δ		7
20335.4	SO ₂ (12 _{3,9} –13 _{2,12})	94	7, N
20346.8	CH ₃ OH (17 ₆ –18 ₅ E)	534	N
20371.5	NH ₃ (5,2)	407	
20460.0	HDO (3 _{2,1} – 4 _{1,4})	226	8
20461.8	H68 α		8
20470.1	He68 α		1
20472.0	C68 α		1
20494.5	H133 θ		9
20494.3	H138 ι		9
20653.0	H97 γ		
20683.3	H85 β		
20691.8	He85 β		
20718.7	H121 ζ		10
20719.2	NH ₃ (8,6)	835	10
20735.4	NH ₃ (9,7)	1023	
20804.9	NH ₃ (7,5)	666	
20814.3	H114 ϵ		
20895.6	H106 δ		
20908.9	CH ₃ OH (16 ₋₄ –15 ₋₅ E)	403	
20932.5	H137 ι		
20950.5	H132 θ		
20970.7	CH ₃ OH $v_t=1$ (10 ₁ –11 ₂ A ⁺)	452	
20994.7	NH ₃ (6,4)	514	
21070.7	NH ₃ (11,9)	1450	
21134.3	NH ₃ (4,1)	280	
21227.2	H126 η		11
21228.6	H120 ζ		11
21285.3	NH ₃ (5,3)	380	
21295.2	H96 γ		
21301.3	HC ₅ N (8 – 7)	2	
21303.9	He96 γ		
21359.9	H113 ϵ		
21383.2	H136 ι		12
21384.8	H67 α		12
21393.5	He67 α		1
21395.5	C67 α		1
21420.0	H131 θ		13
21422.1	H84 β		13
21430.8	He84 β		
21487.2	H105 δ		
21550.3	CH ₃ OH $v_t=1$ (12 ₂ –11 ₁ A ⁻)	479	
21637.9	¹⁵ NH ₃ (4,3)	240	
21703.4	NH ₃ (4,2)	264	
21784.0	¹⁵ NH ₃ (3,2)	152	N
21903.8	H130 θ		
21924.8	H112 ϵ		
21964.3	H95 γ		
21973.3	He95 γ		
21981.6	HNCO (1 _{0,1} –0 _{0,0})	1	
22044.2	¹⁵ NH ₃ (2,1)	82	N

Table 2. continued.

Rest frequency (MHz)	Transition	E_u/k (K)	notes
22101.4	H104 δ		
22196.5	H83 β		
22205.5	He83 β		
22235.1	H ₂ O (6 _{1,6} –5 _{2,3})	643	14
22299.6	H118 ζ		
22324.4	H134 ι		
22364.2	H66 α		
22373.3	He66 α		1
22375.3	C66 α		1
22402.1	H129 θ		
22509.8	H111 ϵ		
22624.9	¹⁵ NH ₃ (1,1)	24	
22649.8	¹⁵ NH ₃ (2,2)	66	
22653.0	NH ₃ (5,4)	343	
22661.8	H94 γ		
22671.0	He94 γ		
22688.3	NH ₃ (4,3)	238	
22732.5	NH ₃ (6,5)	467	
22739.2	H103 δ		
22748.5	He103 δ		
22775.1	H123 η		
22789.4	¹⁵ NH ₃ (3,3)	126	
22815.7	H133 ι		
22827.7	CH ₃ OCHO (2 _{1,2} –1 _{1,1} E)	2	15
22828.1	CH ₃ OCHO (2 _{1,2} –1 _{1,1} A)	2	15
22834.2	NH ₃ (3,2)	150	
22862.3	H117 ζ		
22915.8	H128 θ		
22925.0	NH ₃ (7,6)	608	
22965.6	H ₂ CO (9 _{2,7} –9 _{2,8})	205	N
23008.6	H82 β		
23018.0	He82 β		
23046.0	¹⁵ NH ₃ (4,4)	204	
23098.8	NH ₃ (2,1)	80	
23115.9	H110 ϵ		
23121.0	CH ₃ OH (9 ₂ –10 ₁ A ⁺)	142	
23145.4	¹³ CH ₃ OH (4 ₀ –3 ₁ E)	36	N
23232.3	NH ₃ (8,7)	767	
23321.6	H132 ι		16
23324.4	H122 η		16
23347.0	CH ₃ OH (7 ₁ –7 ₁ A ⁺)	80	N
23389.1	H93 γ		17
23390.0	CH ₃ OCH ₃ (12 _{3,10} –11 _{4,7} AA)	83.7	17, N
23393.1	CH ₃ OCH ₃ (12 _{3,10} –11 _{4,7} EE)	83.7	N
23398.6	He93 γ		18
23401.8	H102 δ		18, 19
23404.3	H65 α		19
23411.4	He102 δ		20
23413.8	He65 α		1, 20, 21
23414.2	SO ₂ (5 _{2,4} –6 _{1,5})	24	N, 21
23416.0	C65 α		1
23422.0	¹⁵ NH ₃ (5,5)	300	
23444.0	H116 ζ		22
23444.8	CH ₃ OH (10 ₁ –9 ₂ A [–])	143	22
23445.3	H127 θ		22
23518.2	H136 κ		
23657.6	NH ₃ (9,8)	943	
23694.5	NH ₃ (1,1)	23	
23722.6	NH ₃ (2,2)	64	

Table 2. continued.

Rest frequency (MHz)	Transition	E_u/k (K)	notes
23743.8	H109 ϵ		
23842.5	H131 ι		
23860.9	H81 β		
23870.1	NH ₃ (3,3)	124	23
23870.6	He81 β		23
23891.6	H121 η		
23922.3	¹⁵ NH ₃ (6,6)	414	
23963.9	HC ₅ N (9–8)	6	
23991.2	H126 θ		
24039.6	SO ₂ (21 _{5,17} –22 _{4,18})	274	
24045.6	H115 ζ		
24083.5	SO ₂ (8 _{2,6} –9 _{1,9})	43	
24090.4	H101 δ		
24100.2	He101 δ		
24139.4	NH ₃ (4,4)	201	
24147.9	H92 γ		
24157.7	He92 γ		
24205.4	NH ₃ (10,9)	1138	
24296.5	CH ₃ OCHO (2 _{0,2} –1 _{0,1} E)	2	
24298.5	CH ₃ OCHO (2 _{0,2} –1 _{0,1} A)	2	
24325.9	OCS (2–1)	2	
24379.1	H130 ι		
24394.8	H108 ϵ		
24477.3	H120 η		
24509.9	H64 α		
24519.9	He64 α		1
24522.1	C64 α		1
24532.9	NH ₃ (5,5)	295	
24625.2	CH ₃ OCHO (12 _{3,9} –12 _{3,10} E)	53	N
24649.4	CH ₃ OCHO (12 _{3,9} –12 _{3,10} A)	53	N
24668.0	H114 ζ		
24755.7	H80 β		
24765.8	He80 β		
24806.3	H100 δ		
24816.4	He100 δ		
24882.0	NH ₃ (11,10)	1350	N
24928.7	CH ₃ OH (3 ₂ –3 ₁ E)	36	24
24931.9	H129 ι		24
24933.5	CH ₃ OH (4 ₂ –4 ₁ E)	45	
24934.4	CH ₃ OH (2 ₂ –2 ₁ E)	29	
24939.8	H91 γ		
24950.0	He91 γ		
24959.1	CH ₃ OH (5 ₂ –5 ₁ E)	57	
25018.1	CH ₃ OH (6 ₂ –6 ₁ E)	71	
25023.8	NH ₂ D (4 _{1,4a} –4 _{0,4s})	152	
25056.0	NH ₃ (6,6)	408	
25069.7	H107 ϵ		
25079.9	He107 ϵ		25
25082.3	H119 η		25
25124.9	CH ₃ OH (7 ₂ –7 ₁ E)	87	
25134.9	H124 θ		
25294.4	CH ₃ OH (8 ₂ –8 ₁ E)	106	
25312.0	H113 ζ		
25322.8	CH ₃ OH $v_t=1$ (9 _{9,1} –9 _{8,2} A)	788	26, 27, N
	CH ₃ OH $v_t=1$ (9 _{9,0} –9 _{8,1} A)	788	26, 27, N
25323.5	¹⁵ NH ₃ (8,8)	688	27, N
25392.8	SO ₂ (8 _{1,7} –7 _{2,6})	37	N
25497.5	CH ₃ OCHO (20 _{5,15} –20 _{5,16} E)	143	N
25501.5	H128 ι		

Table 2. continued.

Rest frequency (MHz)	Transition	E_u/k (K)	notes
25530.7	CH ₃ OCHO (20 _{5,15} –20 _{5,16} A)	143	N
25541.4	CH ₃ OH (9 _{2,7} –9 _{1,8} E)	127	
25550.8	H99 δ		
25561.2	He99 δ		
25609.7	H136 λ		
25642.8	H132 κ		
25686.3	H63 α		
25695.9	H79 β		28
25696.7	He63 α		1, 28
25699.1	C63 α		1
25706.4	He79 β		29
25707.4	H118 η		29
25715.1	NH ₃ (7,7)	539	
25730.2	CH ₃ OCHO (16 _{4,12} –16 _{4,13} E)	93	N
25734.1	H123 θ		
25759.8	CH ₃ OCHO (16 _{4,12} –16 _{4,13} A)	93	N
25766.8	H90 γ		30
25769.8	H106 ϵ		30
25777.3	He90 γ		
25787.1	CH ₃ OH (26 ₂ –26 ₁ E)	836	N
25878.3	CH ₃ OH (10 ₂ –10 ₁ E)	150	
25978.7	H112 ζ		
26044.8	CH ₃ OCHO (2 _{1,1} –1 _{1,0} E)	3	
26048.5	CH ₃ OCHO (2 _{1,1} –1 _{1,0} A)	3	
26120.6	CH ₃ OH $v_t=1$ (10 ₁ –11 ₂ A ⁺)	453	N
26124.6	CH ₃ CH ₂ CN (3 _{1,3} – 2 _{1,2})	4	N

Notes. Notes– (1) C α lines all blended with nearby He α lines in our band. (2) CH₃CN (1₀ – 0₀) at 18398.0 MHz is blended with H126 ζ at 18400.1 MHz. (3) H126 ζ at 18400.1 MHz is blended with H138 θ at 18402.7 MHz. (4) NH₂D (3_{1,3}–3_{0,3}) at 18807.9 MHz is blended with NH₃ (8,5) at 18808.5 MHz and H118 ϵ at 18808.4 MHz. (5) H124 ζ at 19283.8 MHz is blended with H117 ϵ at 19284.8 MHz. (6) H108 δ at 19776.0 MHz is blended with H116 ϵ at 19777.4 MHz. (7) He107 δ at 20333.8 MHz is blended with SO₂ (12_{3,9} – 13_{2,12}) at 20335.4 MHz. (8) HDO (3_{2,1} – 4_{1,4}) at 20460.0 MHz is blended with H68 α at 20461.8 MHz. (9) H133 θ at 20494.5 MHz is blended with H138 ι at 20494.3 MHz. (10) H121 ζ at 20718.7 MHz is blended with NH₃ (8,6) at 20719.2 MHz. (11) H126 η at 21227.2 MHz is blended with H120 ζ at 21228.6 MHz. (12) H136 ι at 21383.2 MHz is blended with H67 α at 21384.8 MHz. (13) H131 θ at 21420.0 MHz is blended with H84 β at 21422.1 MHz. (14) H₂O (6_{1,6} – 5_{2,3}) at 22235.1 MHz is blended with NH₃ (3,1) at 22234.6 MHz. (15) CH₃OCHO (2_{1,2} – 1_{1,1} E) at 22827.7 MHz is blended with CH₃OCHO (2_{1,2} – 1_{1,1} A) at 22828.1 MHz. (16) H132 ι at 23321.6 MHz is blended with H122 η at 23324.4 MHz. (17) H93 γ at 23389.1 MHz is blended with CH₃OCH₃ (12_{3,10}–11_{4,7} AA) at 23390.0 MHz. (18) He93 γ at 23398.6 MHz is blended with H102 δ at 23401.8 MHz. (19) H102 δ at 23401.8 MHz is blended with H65 α at 23404.3 MHz. (20) He102 δ at 23411.4 MHz is blended with He65 δ at 23413.8 MHz. (21) He65 α at 23413.8 MHz is blended with SO₂ (5_{2,4}–6_{1,5}) at 23414.2 MHz. (22) H116 ζ at 23444.0 MHz is blended with CH₃OH (10_{1,9}–9_{2,8} A) at 23444.8 MHz and H127 θ at 23445.3 MHz. (23) NH₃ (3,3) at 23870.1 MHz is blended with He81 β at 23870.6 MHz. (24) CH₃OH (3_{2,1} – 3_{1,2} E) at 24928.7 MHz is blended with H129 ι at 24931.9 MHz. (25) He107 ϵ at 25079.9 MHz is blended with H119 η at 25082.3 MHz. (26) CH₃OH $v_t=1$ (9_{9,1}–9_{8,2} A) and CH₃OH $v_t=1$ (9_{9,0}–9_{8,1} A) at 25322.8 MHz are nearly degeneracy. (27) CH₃OH $v_t=1$ (9_{9,1}–9_{8,2} A) at 25322.8 MHz is blended with ¹⁵NH₃ (8,8) at 25323.5 MHz. (28) H79 β at 25695.9 MHz is blended with He63 α at 25696.7 MHz. (29) He79 β at 25706.4 MHz is blended with H118 η at 25707.4 MHz. (20) H90 γ at 25766.8 MHz is blended with H106 ϵ at 25769.8 MHz. (N) Newly detected transits in the interstellar medium from known astronomical molecules.

Table 3. Column densities and rotational temperatures of the detected molecules compared with previous studies.

Species	This work					Other studies				
	T_{rot} (K)	N (cm^{-2})	$\chi(N/N_{\text{H}_2})$	θ_s ($''$)	Note	T_{rot} (K)	N (cm^{-2})	θ_s ($''$)	Note ^(b)	Ref.
NH ₃ ($J = K + 1$)	209 ± 22	$(1.2 \pm 0.7) \times 10^{17}$	$(4.0 \pm 2.1) \times 10^{-7}$	10	HC	160 ± 25	$2.9^{+0.9}_{-0.7} \times 10^{16}$	40	beam	Her88
NH ₃ ($J = K + 2$)	192 ± 13	$(2.4 \pm 0.8) \times 10^{17}$	$(7.9 \pm 2.5) \times 10^{-7}$	10	HC	250	1.3×10^{17}	10	HC	Cro14
NH ₃ ($J = K + 3$)	191 ± 13	$(4.1 \pm 0.9) \times 10^{17}$	$(1.3 \pm 0.3) \times 10^{-6}$	10	HC					
NH ₃ ($J = K + 4$)	118 ± 13	$(1.9 \pm 1.1) \times 10^{18}$	$(6.0 \pm 3.5) \times 10^{-6}$	10	HC					
¹⁵ NH ₃ (metastable, para)	124 ± 14	$(2.6 \pm 0.4) \times 10^{15}$	$(8.4 \pm 0.1) \times 10^{-9}$	10	HC	110 ± 10	6.6×10^{13}	40	beam	Her85
¹⁵ NH ₃ (metastable, ortho)	119 ± 14	$(2.5 \pm 0.8) \times 10^{15}$	$(8.1 \pm 0.3) \times 10^{-9}$	10	HC	115 ± 15	9.4×10^{13}	40	beam	Her85
¹⁵ NH ₃ (non-metastable)	86 ± 13	$(1.6 \pm 1.8) \times 10^{15}$	$(5.2 \pm 5.8) \times 10^{-9}$	10	HC	200	1.0×10^{15}	10	HC	Cro14
NH ₂ D (para)	120 ^(a)	$(2.0 \pm 0.4) \times 10^{15}$	$(6.4 \pm 1.3) \times 10^{-9}$	10	HC	115	1.7×10^{14}	40	beam	Wal87
							$(2.8 \pm 0.7) \times 10^{15}$	10	HC	Nei13
						75 ± 11	$(9.7 \pm 3.8) \times 10^{15}$	11	beam	Sch01
						250	3.9×10^{15}	10	HC	Cro14
						160	8.7×10^{15}	11	beam	Whi03
CH ₃ OH (E)	115 ± 8	$(1.1 \pm 0.4) \times 10^{18}$	$(2.8 \pm 1.1) \times 10^{-6}$	10	CR	599 ± 295	$(9.3 \pm 4.8) \times 10^{16}$	11	beam	Whi03
CH ₃ OH (A)	131 ± 8	$(8.6 \pm 1.4) \times 10^{17}$	$(2.2 \pm 0.4) \times 10^{-6}$	10	CR	188 ± 3	$(7.0 \pm 0.2) \times 10^{16}$	20	beam	Sch97
						303 ± 6	$(5.0 \pm 0.2) \times 10^{16}$	11	beam	Sch01
						140	4.5×10^{16}	65 – 107	beam	Tur91
						114	7.7×10^{15}	40	beam	Ziu93
						140	4.5×10^{16}	46	beam	Jon84
¹³ CH ₃ OH (E)	120 ^(a)	$(1.6 \pm 0.3) \times 10^{16}$	$(4.0 \pm 0.8) \times 10^{-8}$	10	CR	33 ± 5	$(2.0 \pm 0.6) \times 10^{15}$	25	CR	Men88
						190 ± 150	$(5.0 \pm 4.0) \times 10^{15}$	25	CR	Men88
						140	1.0×10^{16}	10	CR	Cro14
						128	1.5×10^{16}	10	HC(S)	Cro14
						229 ± 14	$(9.6 \pm 1.1) \times 10^{15}$	11	beam	Sch01
						115	5.9×10^{16}	6	CR	Per07
SO ₂	137 ± 20	$(1.5 \pm 0.2) \times 10^{16}$	$(4.7 \pm 0.8) \times 10^{-8}$	10	HC	136 ± 9	$(1.2 \pm 0.1) \times 10^{17}$	11	beam	Whi03
	82 ± 10	$(2.2 \pm 0.4) \times 10^{15}$	$(7.8 \pm 1.5) \times 10^{-9}$	30	Plateau	187 ± 4	$(6.0 \pm 0.3) \times 10^{16}$	11	beam	Sch01
						240	9.0×10^{16}	10	HC	Cro14
						100	1.8×10^{15}	10	CR	Cro14
						140	2×10^{16}	40	beam	Ziu93
						138 ^{+14.7} _{-12.0}	$1.5^{+0.35}_{-0.2} \times 10^{16}$	65 – 107	beam	Tur91
						124 ± 3	$(7.7 \pm 0.5) \times 10^{16}$	20	beam	Sch97
						93	8.0×10^{16}	30	beam	Ser95
						136	1.8×10^{16}	46	beam	Lee02
							$(1.0 \pm 0.4) \times 10^{17}$	10	HC	Esp13b
							$(1.0 \pm 0.3) \times 10^{16}$	30	Plateau	Esp13b
OCS	100 ^(a)	$(5.8 \pm 1.2) \times 10^{16}$	$(1.9 \pm 0.4) \times 10^{-7}$	10	HC(S)	106	9.0×10^{16}	11	beam	Whi03
	100 ^(a)	$(9.0 \pm 1.8) \times 10^{15}$	$(5.0 \pm 1.0) \times 10^{-8}$	30	Plateau	118	8.6×10^{14}	65 – 107	beam	Tur91
						83 ± 30	$(1.8 \pm 1.8) \times 10^{16}$	20	beam	Sch97
						190	3.2×10^{16}	10	HC	Cro14
						165	4.3×10^{15}	10	CR	Cro14
						110	1.2×10^{16}	30	Plateau	Cro14
							$(1.6 \pm 0.4) \times 10^{16}$	15	CR	Ter10
							$(1.2 \pm 0.3) \times 10^{16}$	30	Plateau	Ter10
							$(5.3 \pm 1.0) \times 10^{16}$	10	HC	Ter10
HNCO	150 ^(a)	$(2.3 \pm 0.5) \times 10^{17}$	$(7.5 \pm 1.5) \times 10^{-7}$	10	HC(S)	150 ± 14	$(4.9 \pm 0.4) \times 10^{15}$	11	beam	Whi03
						160 ± 14	$(1.3 \pm 2.3) \times 10^{15}$	20	beam	Sch97
						240 ± 13	$(3.1 \pm 0.5) \times 10^{15}$	11	beam	Sch01
H ₂ CO	150 ^(a)	$(6.5 \pm 1.3) \times 10^{16}$	$(2.1 \pm 0.4) \times 10^{-7}$	10	HC(S)	166	1.6×10^{16}	11	beam	Whi03
						190 ± 9	$(3.2 \pm 0.5) \times 10^{15}$	11	beam	Sch01
						39.9	2.4×10^{14}	65 – 107	beam	Tur91
HC ₃ N	200 ^(a)	$(2.5 \pm 0.5) \times 10^{16}$	$(8.0 \pm 1.6) \times 10^{-8}$	10	HC	225 ± 200	$(5.2 \pm 7.8) \times 10^{15}$	20	beam	Sch97
						32.4 ⁺⁶⁰ ₋₁₂	$4.6^{+3.0}_{-1.8} \times 10^{13}$	65 – 107	beam	Tur91
						200	1.8×10^{15}	10	HC	Per07
						164	1.5×10^{15}	11	beam	Whi03
						210	1.5×10^{15}	10	HC	Cro14
						115	1.3×10^{15}	30	Plateau	Cro14
						110	$(2.0 \pm 0.5) \times 10^{14}$	15	CR	Esp13a
						220	$(1.0 \pm 0.3) \times 10^{15}$	10	HC	Esp13a
						150	$(7 \pm 2) \times 10^{14}$	20	Plateau	Esp13a
HC ₅ N	30 ^(a)	$(1.2 \pm 0.2) \times 10^{14}$	$(3.1 \pm 0.5) \times 10^{-10}$	10	CR	31.2 ^{+3.5} _{-3.4}	$1.0^{+0.46}_{-0.27} \times 10^{13}$	65 – 107	beam	Tur91
	200 ^(a)	$(6.9 \pm 1.1) \times 10^{14}$	$(2.2 \pm 0.4) \times 10^{-9}$	10	HC	220	$(7 \pm 2) \times 10^{13}$	10	HC	Esp13a
						110	$(3.0 \pm 0.9) \times 10^{12}$	15	CR	Esp13a

Table 3. continued.

Species	This work					Other study				
	T_{rot} (K)	N (cm^{-2})	$\chi(N/N_{\text{H}_2})$	θ_s ($''$)	Note	T_{rot} (K)	N (cm^{-2})	θ_s ($''$)	Note ^(b)	Ref.
CH ₃ OCH ₃	100 ^(a)	$(4.4 \pm 0.9) \times 10^{16}$	$(1.1 \pm 0.2) \times 10^{-8}$	10	CR	60	$(5 \pm 2) \times 10^{12}$	120	ER	Esp13a
						160	2×10^{16}	10		Com05
						89 \pm 5	$(1.8 \pm 0.2) \times 10^{16}$	20	beam	Sch97
						360 \pm 26	$(2.8 \pm 0.4) \times 10^{15}$	11	beam	Sch01
						112	1.3×10^{17}	6	CR	Per07
						110	6.5×10^{16}	10	CR	Cro14
						100	2.1×10^{16}	10	HC(S)	Cro14
						157 \pm 30	$(1.4 \pm 0.2) \times 10^{16}$	11	beam	Whi03
						197.4	1.1×10^{16}	46	beam	Lee02
						75	2.5×10^{15}	46	beam	Joh84
						109	3.0×10^{15}	40	beam	Ziu93
						91.0 ^{+33.7} _{-19.0}	$1.3^{+0.3}_{-0.1} \times 10^{15}$	65 – 107	beam	Tur91
						301 \pm 95	$(5.1 \pm 1.0) \times 10^{16}$	11	beam	Whi03
						98 \pm 3	$(1.5 \pm 0.1) \times 10^{16}$	20	beam	Sch97
						110	1.3×10^{17}	10	CR	Cro14
CH ₃ OCHO (E)	69 \pm 8	$(1.3 \pm 0.2) \times 10^{17}$	$(3.4 \pm 0.4) \times 10^{-7}$	10	CR	316 \pm 9	$(1.3 \pm 0.1) \times 10^{17}$	11	beam	Sch01
						52	7.7×10^{14}	40	beam	Ziu93
CH ₃ OCHO (A)	92 \pm 14	$(1.8 \pm 0.2) \times 10^{17}$	$(4.7 \pm 0.6) \times 10^{-7}$	10	CR		2.5×10^{16}	30	beam	Ser95
						75.2	1.5×10^{15}	46	beam	Lee02
CH ₃ CN	200 ^(a)	$(1.9 \pm 0.4) \times 10^{17}$	$(6.1 \pm 1.2) \times 10^{-7}$	10	HC	227 \pm 21	$(3.6 \pm 0.4) \times 10^{15}$	11	beam	Whi03
						445 \pm 36	$(1.7 \pm 0.7) \times 10^{15}$	46	beam	Sch97
						274	6.5×10^{14}	65 – 107	beam	Tur91
						260	3.7×10^{15}	10	HC	Cro14
						230	3.5×10^{15}	10	CR	Cro14
						120	1.0×10^{16}	30	Plateau	Cro14
CH ₃ CH ₂ CN	150 ^(a)	$(4.1 \pm 0.8) \times 10^{16}$	$(1.3 \pm 0.3) \times 10^{-7}$	10	HC	136	2.1×10^{16}	10	HC	Cro14
						99 \pm 3	$(1.3 \pm 0.2) \times 10^{16}$	20	beam	Sch97
						239 \pm 4	$(3.1 \pm 0.2) \times 10^{16}$	11	beam	Sch01
							$(7 \pm 2) \times 10^{16(c)}$		HC	Lop14

Notes.

(a) the rotational temperature is fixed. (b) “beam” in the note represents that the column density is beam-averaged. (c) The value is the sum of the three hot core components in López et al. (2014).

References for rotational temperatures and column densities from the literature. –Her85: Hermsen et al. (1985); Her88: Hermsen et al. (1988); Wal87: Walmsley et al. (1987); Nei13: Neill et al. (2013a); Sch97: Schilke et al. (1997); Sch01: Schilke et al. (2001); Men88: Menten et al. (1988b); Com05: Comito et al. (2005); Per07: Persson et al. (2007); Cro14: Crockett et al. (2014); Lee02: Lee & Cho (2002); Joh84: Johansson et al. (1984); Whi03: White et al. (2003); Ter10: Tercero et al. (2010); Ser95: Serabyn & Weisstein (1995); Tur91: Turner (1991); Ziu93: Ziurys & McGonagle (1993); Lop14: López et al. (2014); Esp13a: Esplugues et al. (2013a); Esp13b: Esplugues et al. (2013b).

Table 4. The spatial origin of molecules detected by our 1.3 cm line survey.

molecules	origins ⁽¹⁾						
	HC	HC(S)	Plateau	CR	MM4	MM5	MM6
NH ₃	√	√	√		√	√	√
¹⁵ NH ₃	√						
NH ₂ D	√	√			√	√	
HDO		√					
SO ₂	√	√	√	√			
OCS	√	√	√	√	√	√	
HC ₃ N	√	√			√	√	√
HC ₅ N		?		?			
CH ₃ OH	√	√		√	√	√	√
¹³ CH ₃ OH				√			
HNCO	√	√		√	√	√	√
H ₂ CO	√	√	√	√		√	√
CH ₃ CN	√	√		√	√	√	√
CH ₃ CH ₂ CN	√	√			√		
CH ₃ OCHO				√			√
CH ₃ OCH ₃				√		√	√

Notes.

⁽¹⁾ A “?” mark indicates that the origin is still questionable. √ denotes that the molecule has emission originating from the component.

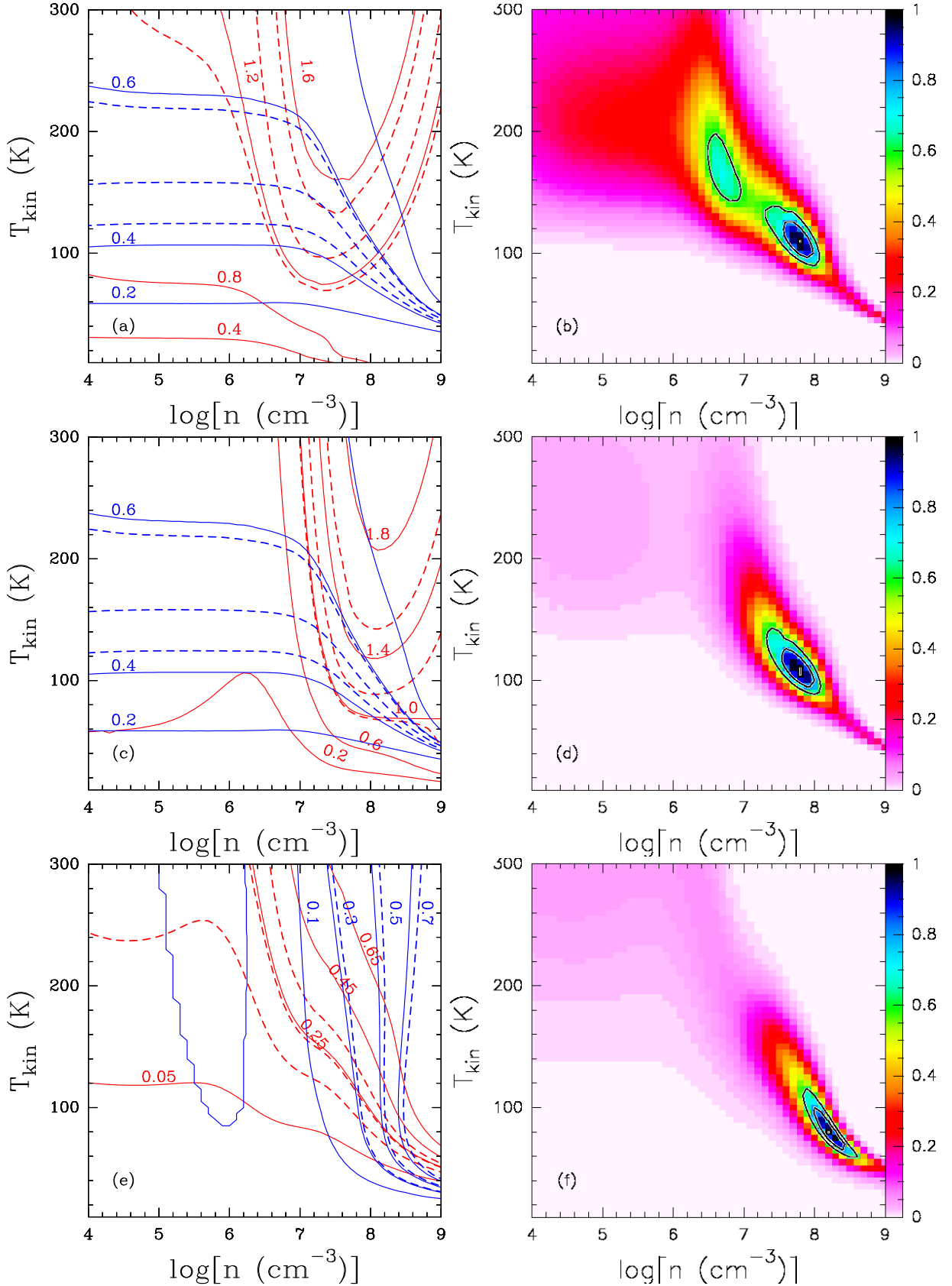


Fig. 8. Radex radiative transfer calculations on the excitation of $^{15}\text{NH}_3$. (a) The modeled line ratios $\frac{^{15}\text{NH}_3(2,2)}{^{15}\text{NH}_3(1,1)}$ (red lines) and $\frac{^{15}\text{NH}_3(5,5)}{^{15}\text{NH}_3(4,4)}$ (blue lines) as a function of n_{H_2} and T_{kin} . The solid red and blue lines represent the calculated $\frac{^{15}\text{NH}_3(2,2)}{^{15}\text{NH}_3(1,1)}$ and $\frac{^{15}\text{NH}_3(5,5)}{^{15}\text{NH}_3(4,4)}$ line ratios which are labeled. The dashed lines represent observed line ratios and their upper and lower limits. (b) The derived likelihood as a function of n_{H_2} and T_{kin} . Only metastable para- $^{15}\text{NH}_3$ transitions are included in the modeling. The likelihood scale is indicated by the color bar. The contours represent the likelihoods 0.6, and 0.8. (c) Same as Fig. 8a, but the solid red lines represent the line ratios of $\frac{^{15}\text{NH}_3(3,2)}{^{15}\text{NH}_3(2,1)}$. (d) Same as Fig. 8b, but the non-metastable transitions are also included in the modeling. (e) Same as Fig. 8a, but the solid red and blue lines represent the line ratios of $\frac{^{15}\text{NH}_3(6,6)}{^{15}\text{NH}_3(3,3)}$ and $\frac{^{15}\text{NH}_3(4,3)}{^{15}\text{NH}_3(3,3)}$. (f) Same as Fig. 8d, but for ortho- $^{15}\text{NH}_3$ transitions.

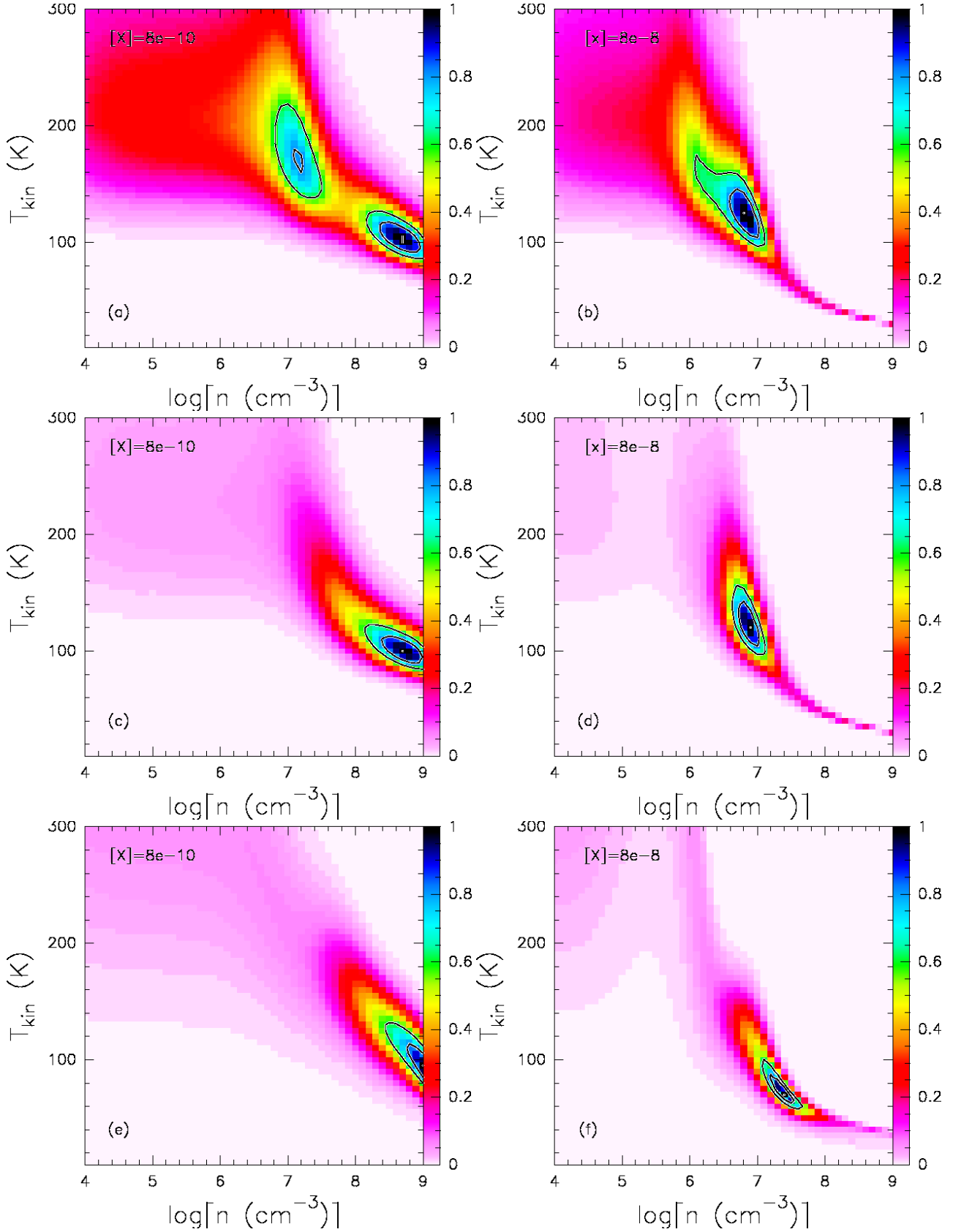


Fig. 9. Same as Fig. 8b, Fig. 8d, and Fig. 8f, but with different $^{15}\text{NH}_3$ abundances of 8×10^{-10} and 8×10^{-8} indicated in the upper left of each panel.

**Appendix A: The observed properties of detected
lines in the survey**

Table A.1. Transitions of recombination lines.

Transition	Rest frequency (MHz)	$\int S_\nu d\nu$ (Jy km s ⁻¹)	v_{lsr} (km s ⁻¹)	$\Delta\nu$ (km s ⁻¹)	S_ν (Jy)	σ (Jy)	notes
Hα							
H71 α	17992.6	72.67 \pm 0.05	-5.4 \pm 0.1	23.8 \pm 0.1	2.870 \pm 0.007	0.006	
H70 α	18769.2	76.19 \pm 0.07	-4.4 \pm 0.1	23.8 \pm 0.1	3.000 \pm 0.009	0.006	
H69 α	19591.1	70.67 \pm 0.04	-3.4 \pm 0.1	23.8 \pm 0.1	2.800 \pm 0.005	0.005	
H68 α	20461.8	73.24 \pm 0.13	-3.6 \pm 0.1	23.3 \pm 0.1	2.960 \pm 0.019	0.008	1
H67 α	21384.8	96.27 \pm 0.11	-5.1 \pm 0.1	23.7 \pm 0.1	3.820 \pm 0.017	0.014	2
H66 α	22364.2	92.61 \pm 0.07	-4.9 \pm 0.1	24.4 \pm 0.1	3.560 \pm 0.010	0.011	
H65 α	23404.3	< 64.39				0.009	b
H64 α	24509.9	62.25 \pm 0.02	-3.6 \pm 0.1	23.5 \pm 0.1	2.480 \pm 0.004	0.004	
H63 α	25686.3	57.00 \pm 0.03	-2.6 \pm 0.1	23.3 \pm 0.1	2.300 \pm 0.005	0.005	
Heα							
He71 α	17999.9	6.32 \pm 0.05	-6.0 \pm 0.1	15.4 \pm 0.2	0.386 \pm 0.007	0.005	
He70 α	18776.8	6.27 \pm 0.05	-4.9 \pm 0.1	15.2 \pm 0.1	0.388 \pm 0.008	0.007	
He69 α	19599.1	5.84 \pm 0.04	-3.9 \pm 0.1	15.2 \pm 0.1	0.361 \pm 0.006	0.005	
He68 α	20470.1	6.70 \pm 0.07	-4.0 \pm 0.1	15.6 \pm 0.2	0.405 \pm 0.011	0.008	
He67 α	21393.5	8.13 \pm 0.09	-5.3 \pm 0.1	14.8 \pm 0.2	0.515 \pm 0.015	0.016	
He66 α	22373.3	7.52 \pm 0.06	-4.7 \pm 0.1	15.5 \pm 0.1	0.455 \pm 0.010	0.010	
He65 α	23413.8	< 12.96				0.005	b
He64 α	24519.9	5.37 \pm 0.02	-4.1 \pm 0.1	15.2 \pm 0.1	0.333 \pm 0.004	0.003	
He63 α	25696.7	< 21.85				0.005	b
Cα							
C71 α	18001.5	0.40 \pm 0.03	6.7 \pm 0.1	4.9 \pm 0.4	0.077 \pm 0.007	0.006	t
C70 α	18778.5	0.30 \pm 0.02	8.1 \pm 0.1	4.0 \pm 0.3	0.070 \pm 0.006	0.006	t
C69 α	19600.9	0.30 \pm 0.02	8.8 \pm 0.2	5.8 \pm 0.5	0.048 \pm 0.005	0.005	t
C68 α	20472.0	0.51 \pm 0.12	7.6 \pm 0.8	11.0 \pm 3.6	0.044 \pm 0.010	0.008	t
C67 α	21395.5	0.54 \pm 0.07	7.1 \pm 0.3	5.9 \pm 0.7	0.085 \pm 0.015	0.016	t
C66 α	22375.3	0.39 \pm 0.04	7.6 \pm 0.2	5.8 \pm 0.6	0.063 \pm 0.009	0.007	t
C65 α	23416.0	0.17 \pm 0.04	8.0 \pm 0.3	3.5 \pm 0.8	0.047 \pm 0.013	0.005	t
C64 α	24522.1	0.27 \pm 0.02	8.1 \pm 0.1	4.7 \pm 0.3	0.054 \pm 0.005	0.004	t
C63 α	25699.1	0.20 \pm 0.02	9.2 \pm 0.2	4.3 \pm 0.4	0.045 \pm 0.006	0.004	t
Hβ							
H89 β	18045.9	18.73 \pm 0.07	-5.2 \pm 0.1	24.0 \pm 0.1	0.734 \pm 0.008	0.007	
H88 β	18661.1	19.98 \pm 0.04	-4.5 \pm 0.1	24.0 \pm 0.1	0.782 \pm 0.006	0.006	
H87 β	19304.7	21.95 \pm 0.05	-3.1 \pm 0.1	23.8 \pm 0.1	0.867 \pm 0.007	0.007	
H86 β	19978.2	24.25 \pm 0.10	-2.6 \pm 0.1	24.8 \pm 0.1	0.920 \pm 0.013	0.013	
H85 β	20683.3	20.49 \pm 0.06	-3.1 \pm 0.1	23.8 \pm 0.1	0.809 \pm 0.008	0.009	
H84 β	21422.1	< 28.64				0.026	b
H83 β	22196.5	23.00 \pm 0.10	-3.5 \pm 0.1	23.1 \pm 0.1	0.934 \pm 0.015	0.014	
H82 β	23008.6	16.32 \pm 0.03	-4.2 \pm 0.1	23.5 \pm 0.1	0.653 \pm 0.005	0.005	
H81 β	23860.9	17.94 \pm 0.03	-3.1 \pm 0.1	23.5 \pm 0.1	0.716 \pm 0.005	0.005	
H80 β	24755.7	16.88 \pm 0.03	-3.9 \pm 0.1	23.5 \pm 0.1	0.674 \pm 0.005	0.005	
H79 β	25695.9	< 22.09				0.007	b
Heβ							
He89 β	18053.2	1.56 \pm 0.04	-5.8 \pm 0.2	14.7 \pm 0.5	0.099 \pm 0.006	0.005	
He88 β	18668.7	1.79 \pm 0.05	-4.8 \pm 0.2	15.7 \pm 0.4	0.107 \pm 0.005	0.005	
He87 β	19312.6	2.06 \pm 0.04	-4.1 \pm 0.2	16.3 \pm 0.4	0.119 \pm 0.007	0.006	
He86 β	19986.3	2.37 \pm 0.11	-2.7 \pm 0.3	15.6 \pm 1.0	0.142 \pm 0.015	0.013	
He85 β	20691.8	1.79 \pm 0.05	-3.4 \pm 0.2	16.1 \pm 0.5	0.105 \pm 0.009	0.008	
He84 β	21430.8	1.87 \pm 0.09	-5.7 \pm 0.3	11.0 \pm 0.6	0.160 \pm 0.022	0.020	3
He83 β	22205.5	2.29 \pm 0.08	-4.3 \pm 0.2	15.9 \pm 0.6	0.135 \pm 0.013	0.013	
He82 β	23018.0	1.44 \pm 0.03	-4.3 \pm 0.1	14.9 \pm 0.3	0.090 \pm 0.005	0.005	
He81 β	23870.6	< 2.77				0.006	b
He80 β	24765.8	1.61 \pm 0.03	-4.6 \pm 0.1	16.7 \pm 0.3	0.090 \pm 0.005	0.004	
He79 β	25706.4	< 105.14				0.005	b
Hγ							
H101 γ	18327.5	10.12 \pm 0.05	-4.6 \pm 0.1	25.5 \pm 0.2	0.373 \pm 0.007	0.005	
H100 γ	18874.8	10.49 \pm 0.04	-3.9 \pm 0.1	24.5 \pm 0.1	0.402 \pm 0.006	0.006	
H99 γ	19444.0	9.64 \pm 0.04	-3.7 \pm 0.1	24.6 \pm 0.1	0.368 \pm 0.005	0.005	
H98 γ	20036.3	10.82 \pm 0.09	-1.5 \pm 0.1	25.3 \pm 0.2	0.402 \pm 0.012	0.009	

Table A.1. continued.

Transition	Rest frequency (MHz)	$\int S_\nu d\nu$ (Jy km s ⁻¹)	v_{lsr} (km s ⁻¹)	$\Delta\nu$ (km s ⁻¹)	S_ν (Jy)	σ (Jy)	notes
H97 γ	20653.0	9.16 \pm 0.06	-3.2 \pm 0.1	23.9 \pm 0.2	0.361 \pm 0.008	0.007	
H96 γ	21295.2	12.35 \pm 0.07	-4.4 \pm 0.1	24.6 \pm 0.2	0.472 \pm 0.011	0.011	
H95 γ	21964.3	11.18 \pm 0.09	-4.0 \pm 0.1	24.2 \pm 0.2	0.434 \pm 0.014	0.014	
H94 γ	22661.8	11.17 \pm 0.05	-3.9 \pm 0.1	25.1 \pm 0.1	0.417 \pm 0.008	0.008	
H93 γ	23389.1	8.50 \pm 0.05	-3.9 \pm 0.1	24.2 \pm 0.2	0.330 \pm 0.007	0.004	4
H92 γ	24147.9	7.63 \pm 0.02	-3.5 \pm 0.1	24.0 \pm 0.1	0.299 \pm 0.003	0.003	
H91 γ	24939.8	7.62 \pm 0.02	-3.7 \pm 0.1	23.4 \pm 0.1	0.305 \pm 0.004	0.004	
H90 γ	25766.8	< 10.64				0.004	b
He γ							
He101 γ	18335.0	0.92 \pm 0.04	-5.2 \pm 0.3	15.6 \pm 0.9	0.055 \pm 0.006	0.005	
He100 γ	18882.4	1.02 \pm 0.04	-5.4 \pm 0.3	17.6 \pm 0.8	0.055 \pm 0.006	0.006	
He99 γ	19451.9	0.92 \pm 0.03	-4.7 \pm 0.3	17.9 \pm 0.7	0.048 \pm 0.005	0.005	
He98 γ	20044.5	1.06 \pm 0.08	-3.4 \pm 0.5	15.3 \pm 1.4	0.065 \pm 0.012	0.011	
He96 γ	21303.9	1.03 \pm 0.07	-4.7 \pm 0.5	15.4 \pm 1.3	0.063 \pm 0.012	0.010	
He95 γ	21973.3	0.99 \pm 0.08	-4.0 \pm 0.5	14.0 \pm 1.6	0.066 \pm 0.014	0.014	
He94 γ	22671.0	0.88 \pm 0.04	-5.3 \pm 0.4	16.5 \pm 0.9	0.050 \pm 0.008	0.008	
He93 γ	23398.6	< 0.47				0.005	b
He92 γ	24157.7	0.67 \pm 0.02	-4.2 \pm 0.2	16.9 \pm 0.5	0.037 \pm 0.003	0.003	
He91 γ	24950.0	0.77 \pm 0.04	-4.0 \pm 0.3	17.7 \pm 1.1	0.041 \pm 0.004	0.004	
He90 γ	25777.3	0.53 \pm 0.03	-2.8 \pm 0.3	13.0 \pm 0.8	0.038 \pm 0.006	0.005	
H δ							
H111 δ	18241.7	4.58 \pm 0.06	-4.5 \pm 0.2	26.8 \pm 0.4	0.160 \pm 0.006	0.006	
H110 δ	18734.9	5.48 \pm 0.05	-4.3 \pm 0.1	25.5 \pm 0.3	0.202 \pm 0.006	0.005	
H109 δ	19246.1	6.80 \pm 0.05	-2.8 \pm 0.1	26.7 \pm 0.2	0.239 \pm 0.005	0.006	
H108 δ	19776.0	< 9.51				0.012	b
H107 δ	20325.5	5.52 \pm 0.06	-3.7 \pm 0.1	25.5 \pm 0.4	0.204 \pm 0.007	0.007	
H106 δ	20895.6	4.99 \pm 0.07	-3.1 \pm 0.2	24.8 \pm 0.4	0.189 \pm 0.009	0.009	
H105 δ	21487.2	7.34 \pm 0.13	-5.1 \pm 0.2	26.9 \pm 0.6	0.256 \pm 0.013	0.014	
H104 δ	22101.4	7.00 \pm 0.12	-3.7 \pm 0.2	24.6 \pm 0.5	0.267 \pm 0.015	0.014	
H103 δ	22739.2	3.63 \pm 0.05	-4.7 \pm 0.2	23.4 \pm 0.4	0.145 \pm 0.007	0.006	
H102 δ	23401.8	< 69.10				0.005	b
H101 δ	24090.4	4.19 \pm 0.03	-3.7 \pm 0.1	24.2 \pm 0.2	0.163 \pm 0.003	0.003	
H100 δ	24806.3	4.38 \pm 0.03	-3.7 \pm 0.1	23.7 \pm 0.2	0.174 \pm 0.005	0.005	
H99 δ	25550.8	4.08 \pm 0.03	-3.3 \pm 0.1	24.0 \pm 0.2	0.160 \pm 0.004	0.004	
He δ							
He110 δ	18742.5	0.64 \pm 0.04	-4.0 \pm 0.4	17.3 \pm 1.2	0.035 \pm 0.005	0.005	
He107 δ	20333.8	< 3.60				0.009	b
He103 δ	22748.5	0.33 \pm 0.03	-5.0 \pm 0.6	13.7 \pm 1.5	0.023 \pm 0.006	0.006	
He102 δ	23411.4	< 12.96				0.005	b
He101 δ	24100.2	0.37 \pm 0.02	-5.2 \pm 0.3	15.7 \pm 0.9	0.022 \pm 0.003	0.003	
He100 δ	24816.4	0.35 \pm 0.02	-5.0 \pm 0.5	16.1 \pm 1.4	0.020 \pm 0.004	0.004	
He99 δ	25561.2	0.38 \pm 0.02	-5.0 \pm 0.5	16.4 \pm 1.3	0.022 \pm 0.004	0.004	
H ϵ							
H120 ϵ	17901.6	3.38 \pm 0.08	-6.5 \pm 0.3	29.0 \pm 0.8	0.110 \pm 0.006	0.006	
H119 ϵ	18347.5	3.64 \pm 0.07	-5.1 \pm 0.2	27.3 \pm 0.6	0.125 \pm 0.006	0.006	
H118 ϵ	18808.4	< 5.84				0.005	b
H117 ϵ	19284.8	< 7.25				0.005	b
H116 ϵ	19777.4	< 9.29				0.012	b
H115 ϵ	20287.0	2.83 \pm 0.06	-3.6 \pm 0.2	23.9 \pm 0.6	0.111 \pm 0.007	0.007	
H114 ϵ	20814.3	3.20 \pm 0.08	-3.8 \pm 0.3	26.3 \pm 0.8	0.114 \pm 0.009	0.009	
H113 ϵ	21359.9	4.25 \pm 0.14	-6.0 \pm 0.4	23.9 \pm 1.0	0.167 \pm 0.015	0.016	
H112 ϵ	21924.8	4.31 \pm 0.11	-3.4 \pm 0.3	25.5 \pm 0.8	0.159 \pm 0.013	0.013	
H111 ϵ	22509.8	2.91 \pm 0.06	-4.1 \pm 0.2	25.6 \pm 0.6	0.107 \pm 0.007	0.007	
H110 ϵ	23115.9	2.71 \pm 0.03	-4.4 \pm 0.2	25.1 \pm 0.4	0.101 \pm 0.005	0.005	
H109 ϵ	23743.8	2.92 \pm 0.04	-3.1 \pm 0.2	24.4 \pm 0.4	0.112 \pm 0.006	0.006	
H108 ϵ	24394.8	2.78 \pm 0.03	-3.4 \pm 0.1	24.3 \pm 0.3	0.107 \pm 0.004	0.004	
H107 ϵ	25069.7	2.45 \pm 0.04	-4.1 \pm 0.2	23.5 \pm 0.4	0.098 \pm 0.005	0.005	
H106 ϵ	25769.8	< 10.82				0.004	b
He ϵ							

Table A.1. continued.

Transition	Rest frequency (MHz)	$\int S_\nu d\nu$ (Jy km s ⁻¹)	v_{lsr} (km s ⁻¹)	$\Delta\nu$ (km s ⁻¹)	S_ν (Jy)	σ (Jy)	notes
He107 ϵ	25079.9	< 1.43				0.005	b
Hζ							
H127 ζ	17978.5	2.01 \pm 0.05	-6.5 \pm 0.3	24.2 \pm 0.7	0.078 \pm 0.005	0.004	
H126 ζ	18400.1	< 8.62				0.006	b
H125 ζ	18835.1	2.54 \pm 0.07	-3.4 \pm 0.3	27.8 \pm 0.9	0.086 \pm 0.005	0.006	
H124 ζ	19283.8	< 7.25				0.008	b
H122 ζ	20225.1	2.12 \pm 0.06	-3.2 \pm 0.3	23.6 \pm 0.9	0.084 \pm 0.007	0.006	
H121 ζ	20718.7	< 5.26				0.009	b
H120 ζ	21228.6	< 3.75				0.006	b
H118 ζ	22299.6	2.67 \pm 0.11	-4.8 \pm 0.4	25.3 \pm 1.3	0.099 \pm 0.011	0.012	
H117 ζ	22862.3	2.16 \pm 0.07	-4.2 \pm 0.3	27.0 \pm 1.1	0.075 \pm 0.006	0.006	
H116 ζ	23444.0	< 8.09				0.005	b
H115 ζ	24045.6	2.21 \pm 0.04	-2.3 \pm 0.2	26.0 \pm 0.6	0.080 \pm 0.004	0.004	
H114 ζ	24668.0	1.79 \pm 0.03	-4.0 \pm 0.2	24.9 \pm 0.6	0.068 \pm 0.004	0.004	
H113 ζ	25312.0	2.05 \pm 0.04	-3.5 \pm 0.2	24.8 \pm 0.7	0.078 \pm 0.005	0.005	
H112 ζ	25978.7	2.24 \pm 0.06	-3.0 \pm 0.3	24.0 \pm 0.7	0.088 \pm 0.009	0.009	
Hη							
H133 η	18123.4	1.38 \pm 0.09	-5.3 \pm 0.7	27.9 \pm 2.3	0.047 \pm 0.007	0.007	
H132 η	18528.0	1.81 \pm 0.08	-5.3 \pm 0.5	30.0 \pm 1.7	0.057 \pm 0.006	0.006	
H131 η	18944.7	1.71 \pm 0.08	-4.9 \pm 0.5	28.9 \pm 1.6	0.056 \pm 0.006	0.006	
H130 η	19374.0	1.60 \pm 0.06	-3.5 \pm 0.4	26.5 \pm 1.2	0.057 \pm 0.005	0.005	
H129 η	19816.4	1.83 \pm 0.21	-1.6 \pm 1.2	30.3 \pm 4.5	0.057 \pm 0.014	0.014	
H128 η	20272.4	1.16 \pm 0.09	-6.1 \pm 0.9	28.9 \pm 3.0	0.038 \pm 0.007	0.007	
H126 η	21227.2	< 3.74				0.007	b
H123 η	22775.1	1.02 \pm 0.03	-4.7 \pm 0.3	23.0 \pm 0.9	0.042 \pm 0.004	0.004	
H122 η	23324.4	< 2.12				0.006	b
H121 η	23891.6	1.40 \pm 0.04	-3.3 \pm 0.3	24.1 \pm 0.9	0.055 \pm 0.005	0.005	
H120 η	24477.3	1.25 \pm 0.03	-3.4 \pm 0.3	23.7 \pm 0.8	0.050 \pm 0.004	0.004	
H119 η	25082.3	< 1.65				0.005	b
H118 η	25707.4	< 2.75				0.005	b
Hθ							
H139 θ	18019.0	1.46 \pm 0.12	-8.4 \pm 1.0	31.5 \pm 3.1	0.044 \pm 0.006	0.006	
H138 θ	18402.8	< 6.80				0.008	b
H135 θ	19621.6	2.02 \pm 0.06	-3.8 \pm 0.3	31.0 \pm 1.2	0.061 \pm 0.004	0.004	
H134 θ	20051.7	2.77 \pm 0.36	-6.7 \pm 1.7	41.6 \pm 6.4	0.063 \pm 0.013	0.013	5
H133 θ	20494.5	< 3.82				0.006	b
H132 θ	20950.5	1.27 \pm 0.15	-0.7 \pm 1.4	35.3 \pm 5.3	0.034 \pm 0.008	0.008	5
H131 θ	21420.0	< 29.45				0.051	b
H130 θ	21903.8	0.97 \pm 0.10	-3.4 \pm 0.9	18.5 \pm 2.2	0.049 \pm 0.015	0.015	5
H129 θ	22402.1	1.27 \pm 0.06	-3.4 \pm 0.5	26.7 \pm 1.6	0.045 \pm 0.006	0.006	
H128 θ	22915.8	0.97 \pm 0.05	-5.1 \pm 0.5	24.7 \pm 1.6	0.037 \pm 0.006	0.006	
H127 θ	23445.2	< 8.11				0.005	b
H126 θ	23991.2	1.06 \pm 0.03	-3.6 \pm 0.2	28.2 \pm 1.0	0.035 \pm 0.003	0.003	
H124 θ	25134.9	1.10 \pm 0.04	-4.0 \pm 0.4	28.1 \pm 1.3	0.037 \pm 0.004	0.004	
H123 θ	25734.1	0.85 \pm 0.04	-1.9 \pm 0.6	23.4 \pm 1.6	0.034 \pm 0.006	0.006	
Hι							
H142 ι	18859.0	0.62 \pm 0.04	-7.2 \pm 0.7	21.9 \pm 1.9	0.026 \pm 0.005	0.005	
H140 ι	19654.0	0.96 \pm 0.09	-6.6 \pm 1.2	35.1 \pm 4.2	0.026 \pm 0.005	0.005	
H138 ι	20494.3	< 3.37				0.008	b
H137 ι	20932.5	0.83 \pm 0.09	0.3 \pm 1.2	27.0 \pm 4.0	0.029 \pm 0.009	0.009	5
H136 ι	21383.2	< 97.36				0.014	b
H134 ι	22324.4	1.02 \pm 0.07	-5.4 \pm 0.7	27.8 \pm 2.4	0.034 \pm 0.006	0.006	
H133 ι	22815.7	0.98 \pm 0.10	-8.4 \pm 1.2	32.0 \pm 3.8	0.029 \pm 0.006	0.006	
H132 ι	23321.6	1.00 \pm 0.08				0.006	b
H131 ι	23842.5	0.97 \pm 0.06	-3.6 \pm 0.6	28.2 \pm 2.2	0.033 \pm 0.005	0.005	
H130 ι	24379.1	0.67 \pm 0.03	-2.5 \pm 0.4	24.0 \pm 1.2	0.026 \pm 0.004	0.004	
H129 ι	24931.9	< 63.73				0.050	b
H128 ι	25501.5	0.68 \pm 0.03	-4.4 \pm 0.5	23.6 \pm 1.3	0.027 \pm 0.004	0.004	
Hκ							

Table A.1. continued.

Transition	Rest frequency (MHz)	$\int S_\nu d\nu$ (Jy km s ⁻¹)	v_{lsr} (km s ⁻¹)	$\Delta\nu$ (km s ⁻¹)	S_ν (Jy)	σ (Jy)	notes
H136 κ	23518.2	1.14 ± 0.05	-5.1 ± 0.8	35.0 ± 2.0	0.031 ± 0.004	0.004	5
H132 κ	25642.8	0.50 ± 0.04	-3.0 ± 0.6	28.4 ± 2.5	0.017 ± 0.006	0.004	
H λ							
H136 λ	25609.7	0.72 ± 0.03	-2.8 ± 0.6	31.2 ± 1.3	0.022 ± 0.006	0.004	5

Notes. – (1) Although H68 α is blended with HDO (3_{2,1}–4_{1,4}) (see Fig. B.16), the integrated intensity of HDO (3_{2,1}–4_{1,4}) can be ignored compared with H68 α . (2) Although H67 α is blended with H136 ι (see Fig. B.10), the integrated intensity of H136 ι can be neglected. (3) Note that the observed line width is narrower than those of other He RRL transitions. (4) Although H93 γ is blended with CH₃OCH₃ (12_{3,10}–11_{4,7}) (see Fig. B.16), the integrated intensity of CH₃OCH₃ (12_{3,10}–11_{4,7}) can be ignored compared with H93 γ . (5) Note that the fitted parameters are possibly wrong due to low signal-to-noise ratios. (b) it indicates that this line is blended (see Table 2). (t) The fit for the C α line is tentative because it is blended.

Table A.2. The observed properties of NH_3 , $^{15}\text{NH}_3$ and NH_2D transitions.

Rest frequency (MHz)	(J, K)	$\int S_\nu d\nu$ (Jy km s $^{-1}$)	v_{lsr} (km s $^{-1}$)	$\Delta\nu$ (km s $^{-1}$)	S_ν (Jy)	σ (Jy)	notes
NH_3 non-metastable							
18017.3	(7,3)	1.12 ± 0.02	3.4 ± 0.1	6.4 ± 0.1	0.165 ± 0.005	0.005	HC
18391.5	(6,1)	0.28 ± 0.02	3.8 ± 0.3	6.7 ± 0.6	0.039 ± 0.006	0.006	HC
18499.3	(9,6)	0.94 ± 0.03	3.8 ± 0.1	6.1 ± 0.2	0.145 ± 0.008	0.008	HC
18808.5	(8,5)	< 5.89				0.006	b
18884.6	(6,2)	1.27 ± 0.03	3.9 ± 0.1	6.5 ± 0.2	0.185 ± 0.007	0.006	HC
19218.4	(7,4)	1.76 ± 0.02	4.9 ± 0.1	7.3 ± 0.1	0.227 ± 0.006	0.006	HC
19757.5	(6,3)	4.82 ± 0.07	4.9 ± 0.1	8.3 ± 0.1	0.543 ± 0.014	0.014	HC
19838.3	(5,1)	1.93 ± 0.05	5.8 ± 0.1	8.2 ± 0.3	0.220 ± 0.011	0.011	HC
20371.5	(5,2)	3.65 ± 0.07	7.2 ± 0.1	9.4 ± 0.2	0.365 ± 0.009	0.006	HC
20719.2	(8,6)	< 5.1410				0.008	HC, b
20735.4	(9,7)	0.51 ± 0.03	5.9 ± 0.2	4.7 ± 0.3	0.102 ± 0.011	0.010	HC
20804.9	(7,5)	2.83 ± 0.05	7.5 ± 0.1	7.9 ± 0.2	0.334 ± 0.008	0.008	HC
20994.7	(6,4)	5.76 ± 0.04	7.4 ± 0.1	9.1 ± 0.1	0.595 ± 0.010	0.010	HC
21070.7	(11,9)	0.28 ± 0.03	6.9 ± 0.3	6.2 ± 0.7	0.043 ± 0.007	0.008	HC
21134.3	(4,1)	3.32 ± 0.04	7.2 ± 0.1	8.2 ± 0.1	0.381 ± 0.009	0.008	HC
21285.3	(5,3)	9.67 ± 0.04	5.9 ± 0.1	11.8 ± 0.1	0.773 ± 0.007	0.008	a
21703.4	(4,2)	17.16 ± 0.09				0.016	a
22653.0	(5,4)	10.65 ± 0.02				0.003	a
22688.3	(4,3)	22.20 ± 0.02				0.004	a
22732.5	(6,5)	8.80 ± 0.03				0.005	a
22834.2	(3,2)	19.39 ± 0.04				0.006	a
22925.0	(7,6)	8.99 ± 0.04				0.007	a
23098.8	(2,1)	26.22 ± 0.04				0.006	a
23232.3	(8,7)	2.71 ± 0.02	5.8 ± 0.1	7.1 ± 0.1	0.358 ± 0.006	0.006	HC
23657.6	(9,8)	1.65 ± 0.02	7.5 ± 0.1	6.4 ± 0.1	0.244 ± 0.005	0.005	HC
24205.4	(10,9)	1.25 ± 0.01	7.1 ± 0.1	6.9 ± 0.1	0.171 ± 0.004	0.004	HC
24882.0	(11,10)	0.35 ± 0.01	7.3 ± 0.1	5.7 ± 0.2	0.058 ± 0.004	0.004	HC
NH_3 metastable							
23694.5	(1,1)	85.91 ± 0.04				0.004	a
23722.6	(2,2)	82.79 ± 0.06				0.006	a
23870.1	(3,3)	< 104.32				0.008	a, b
24139.4	(4,4)	41.12 ± 0.03				0.003	a
24532.9	(5,5)	31.84 ± 0.04				0.005	a
25056.0	(6,6)	32.80 ± 0.04				0.004	a
25715.1	(7,7)	13.29 ± 0.03				0.003	a
$^{15}\text{NH}_3$ non-metastable							
21637.9	(4,3)	0.59 ± 0.04	5.3 ± 0.2	5.8 ± 0.5	0.095 ± 0.013	0.013	HC
21784.0	(3,2)	0.41 ± 0.06	6.5 ± 0.4	6.3 ± 1.3	0.062 ± 0.013	0.013	HC
22044.2	(2,1)	0.40 ± 0.05	5.9 ± 0.4	7.3 ± 1.2	0.052 ± 0.011	0.011	HC
$^{15}\text{NH}_3$ metastable							
22624.9	(1,1)	0.52 ± 0.04	6.1 ± 0.2	8.7 ± 0.9	0.056 ± 0.006	0.006	HC
22649.8	(2,2)	0.55 ± 0.02	5.8 ± 0.1	6.8 ± 0.4	0.076 ± 0.007	0.006	HC
22789.4	(3,3)	1.38 ± 0.02	5.7 ± 0.1	7.4 ± 0.1	0.175 ± 0.005	0.005	HC
23046.0	(4,4)	0.55 ± 0.02	5.5 ± 0.1	6.3 ± 0.3	0.082 ± 0.006	0.006	HC
23422.0	(5,5)	0.33 ± 0.02	6.1 ± 0.2	7.2 ± 0.4	0.043 ± 0.005	0.005	HC
23922.3	(6,6)	0.31 ± 0.01	5.7 ± 0.1	7.1 ± 0.3	0.041 ± 0.003	0.003	HC
25323.5	(8,8)	< 0.19				0.004	HC, b
NH_2D							
	J_{k_a, k_c}						
18807.9	$3_{1,3S} - 3_{0,3a}$	< 5.84				0.006	ortho, HC, b
25023.8	$4_{1,4a} - 4_{0,4S}$	0.19 ± 0.01	6.9 ± 0.2	5.7 ± 0.5	0.031 ± 0.004	0.005	para, HC

Notes. – (a) the line originates not only from the HC but also contains emission from other components such as the CR, plateau, ER and HC(S).
(b) this line is blended (see Table. 2).

Table A.3. The observed properties of CH₃OH transitions.

Rest frequency (MHz)	J_{k_a}	$\int S_\nu d\nu$ (Jy km s ⁻¹)	v_{LSR} (km s ⁻¹)	$\Delta\nu$ (km s ⁻¹)	S_ν (Jy)	σ (Jy)	notes
CH₃OH							
19967.4	$2_1 - 3_0 E$	5.09±0.03	8.8±0.1	2.7±0.1	1.780±0.013	0.011	
20171.1	$11_1 - 10_2 A^+$	3.36±0.03	8.1±0.1	4.6±0.1	0.688±0.008	0.007	CR
20346.8	$17_6 - 18_5 E$	0.23±0.03	8.1±0.2	4.9±0.7	0.045±0.007	0.006	CR
20908.9	$16_{-4} - 15_{-5} E$	0.60±0.03	8.9±0.1	3.8±0.2	0.147±0.009	0.008	CR
23121.0	$9_2 - 10_1 A^+$	3.17±0.02	7.0±0.1	4.6±0.1	0.651±0.008	0.006	CR
23347.0	$7_1 - 7_1 A^+$	0.77±0.02	7.4±0.1	3.4±0.1	0.214±0.006	0.005	CR
23444.8	$10_1 - 9_2 A^-$	< 4.95				0.004	CR, b
24928.7	$3_2 - 3_1 E$	< 20.42				0.008	M, b
24933.5	$4_2 - 4_1 E$	48.84±0.11	7.8±0.1	2.2±0.1	20.600±0.0558	0.064	M
24934.4	$2_2 - 2_1 E$	10.05±0.17	8.0±0.1	3.2±0.1	2.940±0.0691	0.054	M
24959.1	$5_2 - 5_1 E$	71.01±0.12	7.9±0.1	2.4±0.1	28.300±0.061	0.009	M
25018.1	$6_2 - 6_1 E$	89.20±0.18	7.7±0.1	1.8±0.1	45.600±0.107	0.011	M
25124.9	$7_2 - 7_1 E$	82.39±0.16	7.9±0.1	1.9±0.1	41.700±0.092	0.011	M
25294.4	$8_2 - 8_1 E$	63.70±0.19	8.1±0.1	1.8±0.1	33.100±0.110	0.010	M
25541.4	$9_2 - 9_1 E$	43.21±0.19	8.5±0.1	1.9±0.1	21.700±0.107	0.008	M
25787.1	$26_2 - 26_1 E$	0.06±0.02	8.4±0.2	2.6±0.8	0.022±0.004	0.004	CR
25878.3	$10_2 - 10_1 E$	26.64±0.16	9.0±0.1	2.0±0.1	12.200±0.087	0.005	M
CH₃OH ($v_t=1$)							
20970.7	$10_1 - 11_2 A^+$	0.72±0.02	8.8±0.1	4.2±0.2	0.160±0.008	0.007	CR
21550.3	$12_2 - 11_1 A^-$	0.76±0.05	6.2±0.1	3.4±0.2	0.208±0.012	0.012	CR
25322.8	$9_9 - 9_8 A$	< 0.18				0.004	CR, b
26120.6	$10_1 - 11_2 A^-$	1.44±0.04	8.3±0.1	3.7±0.1	0.364±0.016	0.016	CR
¹³CH₃OH							
23145.4	$4_0 - 3_1 E$	0.11±0.01	6.8±0.2	3.5±0.4	0.030±0.005	0.005	CR

Notes. – (M) these transitions are masers (e.g. Menten et al. 1988a; Matsakis et al. 1980). (b) this line is blended (see Table. 2).

Table A.4. Observed properties of SO₂ and OCS transitions.

Rest frequency (MHz)	J_{k_a,k_c}	$\int S_\nu d\nu$ (Jy km s ⁻¹)	v_{lsr} (km s ⁻¹)	$\Delta\nu$ (km s ⁻¹)	S_ν (Jy)	σ (Jy)	notes
SO ₂							
20335.404	12 _{3,9} – 13 _{2,12}	< 3.72				0.007	b
23414.248	5 _{2,4} – 6 _{1,5}	< 12.96				0.005	b
24039.629	21 _{5,17} – 22 _{4,18}	0.90 ± 0.05	10.6 ± 0.7	26.3 ± 1.1	0.032 ± 0.004	0.003	plateau
24039.629		0.60 ± 0.05	5.3 ± 0.1	8.9 ± 0.4	0.063 ± 0.004	0.003	HC
24083.479	8 _{2,6} – 9 _{1,9}	4.38 ± 0.04	9.2 ± 0.1	26.9 ± 0.2	0.153 ± 0.003	0.003	plateau
24083.479		0.91 ± 0.03	6.2 ± 0.1	8.2 ± 0.2	0.105 ± 0.003	0.003	HC
25392.818	8 _{1,7} – 7 _{2,6}	9.62 ± 0.01	10.0 ± 0.1	27.7 ± 0.1	0.326 ± 0.005	0.005	plateau
25392.818		2.03 ± 0.03	6.1 ± 0.1	9.7 ± 0.1	0.198 ± 0.005	0.005	HC
25392.818		0.58 ± 0.01	8.4 ± 0.1	2.3 ± 0.1	0.241 ± 0.005	0.005	maser?
OCS							
24325.9	2-1	1.08 ± 0.04	5.9 ± 0.2	14.8 ± 0.6	0.069 ± 0.004	0.004	plateau
		1.18 ± 0.03	7.7 ± 0.1	4.2 ± 0.1	0.263 ± 0.004	0.004	HC(S)

Notes. – (b) the line is blended (see Table. 2).

Table A.5. The observed properties of CH₃OCHO transitions.

Rest frequency (MHz)	J_{k_a,k_c}	$\int S_\nu d\nu$ (Jy km s ⁻¹)	ν_{lsr} (km s ⁻¹)	$\Delta\nu$ (km s ⁻¹)	S_ν (Jy)	σ (Jy)	notes
CH ₃ OCHO							
22827.7	2 _{1,2} – 1 _{1,1} E	< 0.26				0.006	CR, b
22828.1	2 _{1,2} – 1 _{1,1} A	< 0.26				0.006	CR, b
24296.5	2 _{0,2} – 1 _{0,1} E	0.24 ± 0.01	7.6 ± 0.1	3.8 ± 0.2	0.060 ± 0.004	0.004	CR
24298.5	2 _{0,2} – 1 _{0,1} A	0.23 ± 0.01	8.4 ± 0.1	3.5 ± 0.2	0.061 ± 0.004	0.004	CR
24625.2	12 _{3,9} – 12 _{3,10} E	0.09 ± 0.01	7.8 ± 0.1	2.8 ± 0.3	0.032 ± 0.004	0.004	CR
24649.4	12 _{3,9} – 12 _{3,10} A	0.07 ± 0.01	7.4 ± 0.3	3.3 ± 0.6	0.019 ± 0.004	0.004	CR
25497.5	20 _{5,15} – 20 _{5,16} E	0.04 ± 0.01	8.6 ± 0.3	2.8 ± 0.5	0.013 ± 0.004	0.004	CR
25530.7	20 _{5,15} – 20 _{5,16} A	0.06 ± 0.01	7.8 ± 0.2	3.0 ± 0.8	0.020 ± 0.005	0.005	CR
25730.2	16 _{4,12} – 16 _{4,13} E	0.05 ± 0.01	6.7 ± 0.1	1.4 ± 0.2	0.033 ± 0.004	0.005	CR
25759.8	16 _{4,12} – 16 _{4,13} A	0.07 ± 0.01	8.5 ± 0.2	3.0 ± 0.5	0.021 ± 0.004	0.004	CR
26044.8	2 _{1,1} – 1 _{1,0} E	0.29 ± 0.02	8.7 ± 0.1	2.5 ± 0.2	0.110 ± 0.009	0.009	CR
26048.5	2 _{1,1} – 1 _{1,0} A	0.29 ± 0.02	9.3 ± 0.1	2.6 ± 0.2	0.105 ± 0.010	0.010	CR

Notes. –(b) this line is blended (see Table 2).

Table A.6. Observed properties of H₂O, HDO, CH₃CN, HC₃N, HC₅N, CH₃OCH₃, H₂CO and HNCO transitions.

Rest frequency (MHz)	transitions	$\int S_\nu d\nu$ (Jy km s ⁻¹)	v_{lsr} (km s ⁻¹)	$\Delta\nu$ (km s ⁻¹)	S_ν (Jy)	σ (Jy)	notes
transitions without hfs							
20460.0	HDO (3 _{2,1} – 4 _{1,4})	< 0.54				0.007	HC(S), b
21301.3	HC ₅ N (8–7)	0.20 ± 0.03	8.6 ± 0.4	5.3 ± 0.9	0.034 ± 0.008	0.009	CR
22235.1	H ₂ O (6 _{1,6} – 5 _{2,3})	> 75000.00				0.014	maser
22965.6	H ₂ CO (9 _{2,7} – 9 _{2,8})	0.41 ± 0.02	7.1 ± 0.1	6.0 ± 0.4	0.064 ± 0.005	0.005	HC(S)
23390.0	CH ₃ OCH ₃ (12 _{3,10} – 11 _{4,7} AA)	< 8.77			0.007		CR, b
23393.1	CH ₃ OCH ₃ (12 _{3,10} – 11 _{4,7} EE)	0.10 ± 0.01	7.3 ± 0.2	2.8 ± 0.4	0.035 ± 0.038	0.007	CR
23963.9	HC ₅ N (9–8)	0.14 ± 0.01	8.1 ± 0.2	4.8 ± 0.5	0.028 ± 0.004	0.004	CR
transitions with hfs							
ν (MHz)	transitions	$\int S_\nu d\nu^{(1)}$ (Jy km s ⁻¹)	v_{lsr} (km s ⁻¹)	$\Delta\nu$ (km s ⁻¹)	τ	σ (Jy)	notes
18196.2	HC ₃ N (2–1)	1.81 ± 0.04	6.6 ± 0.1	4.3 ± 0.1	< 0.1	0.005	HC
18398.0	CH ₃ CN (1 ₀ – 0 ₀)	1.57 ± 0.05	6.1 ± 0.1	6.4 ± 0.4	< 0.1	0.006	HC, b
21981.6	HNCO (1 _{0,1} – 0 _{0,0})	0.99 ± 0.09	8.4 ± 0.3	6.4 ± 0.7	< 0.1	0.014	HC(S)
26124.6	CH ₃ CH ₂ CN (3 _{1,3} – 2 _{1,2})	1.09 ± 0.09	5.9 ± 0.5	7.4 ± 0.9	0.2 ± 0.1	0.014	HC

Notes. – (1) Integrated intensities are calculated from integrating the spectral range with errors derived from σ . Note that integrated intensities for CH₃CN (1₀ – 0₀) are calculated by integrating the spectral range of the fitted hfs model because its observed spectrum is blended. (b) the line is blended (see Table 2)

Appendix B: Zoom-in plots of observed spectra

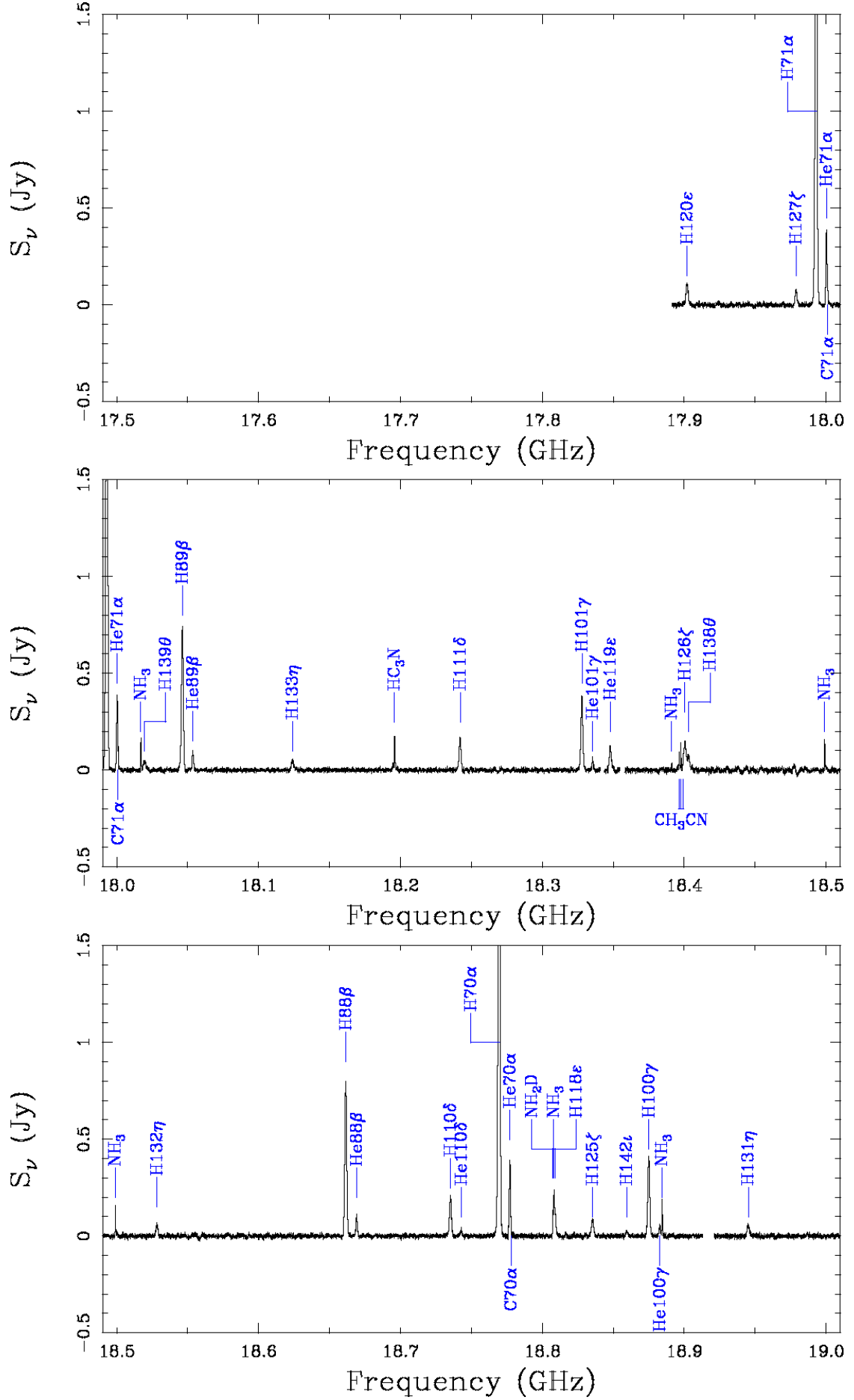


Fig. B.1. Observed spectrum of Orion KL from 17.9 to 26.2 GHz. The displayed frequency scale is based on the Local Standard of Rest velocity 0 km s^{-1} .

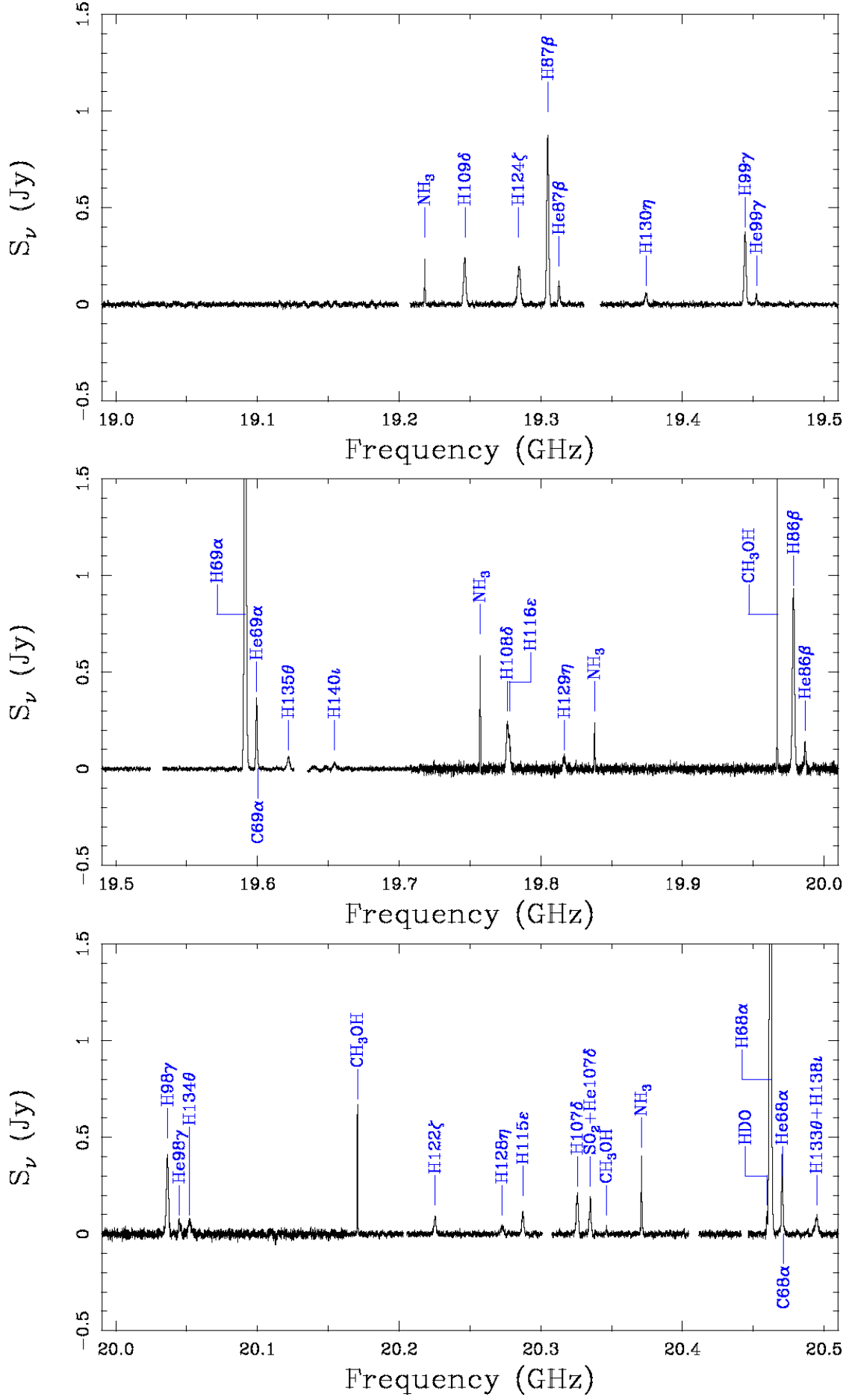


Fig. B.1. — Continued.

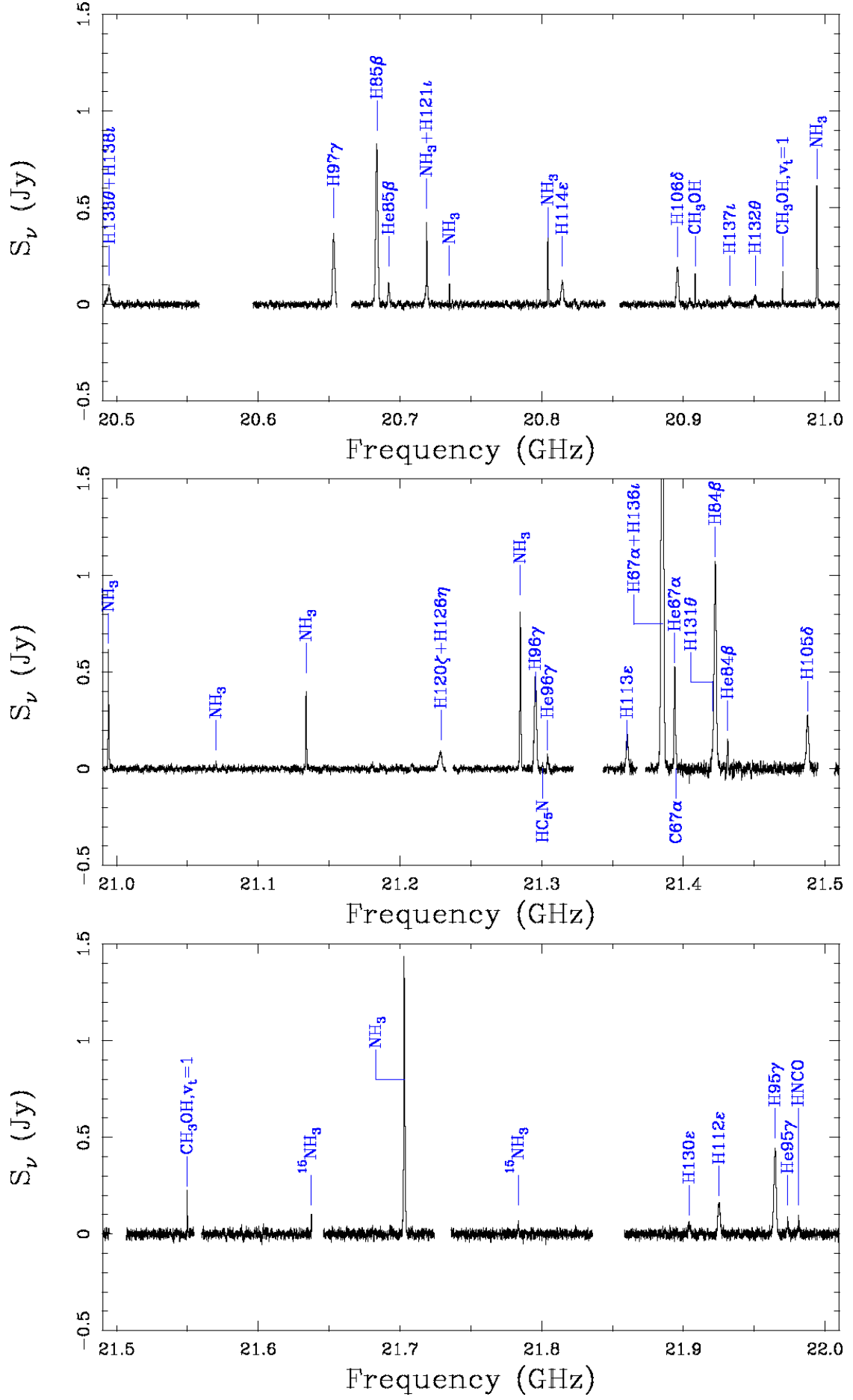


Fig. B.1. — Continued.

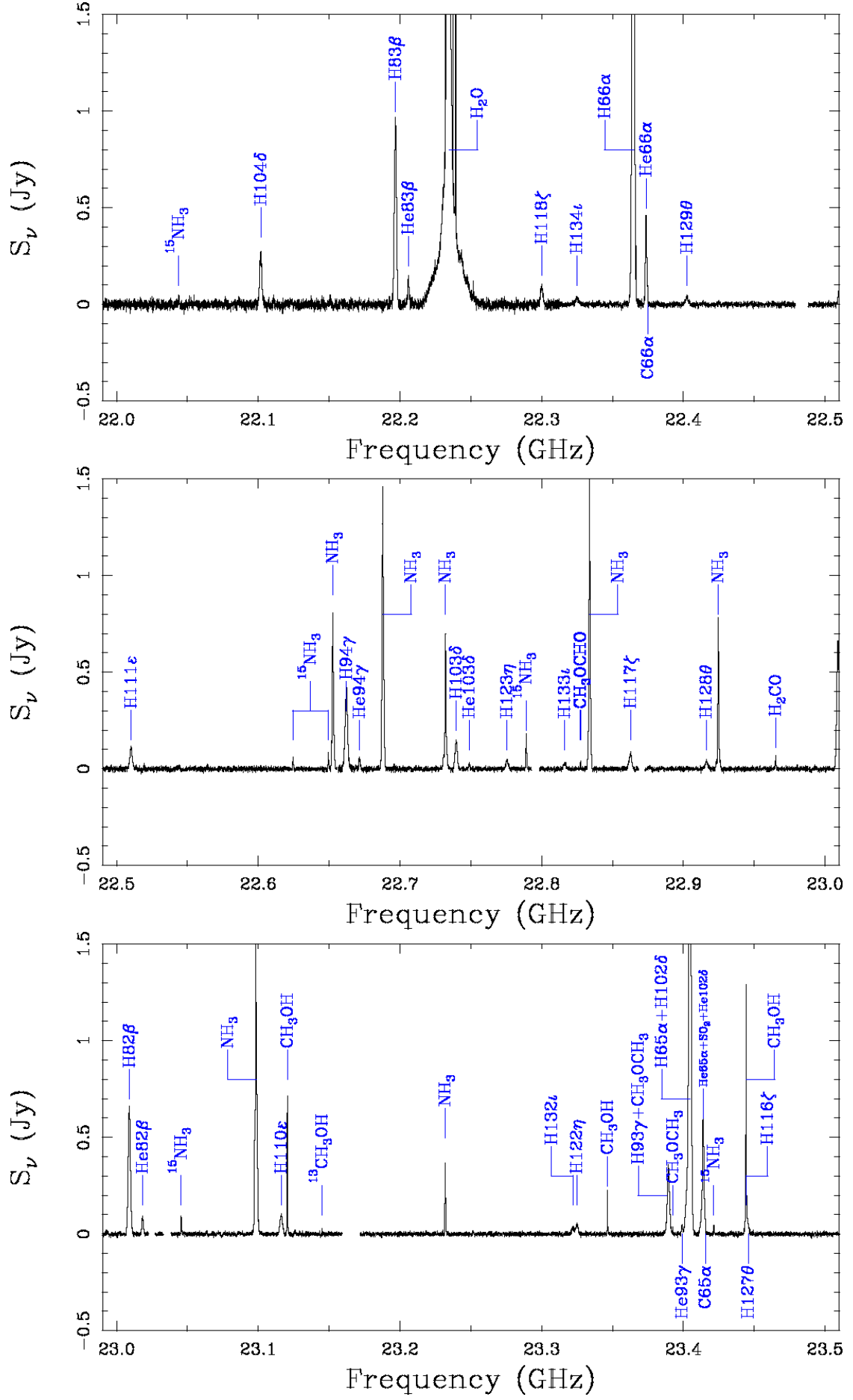


Fig. B.1. — Continued.

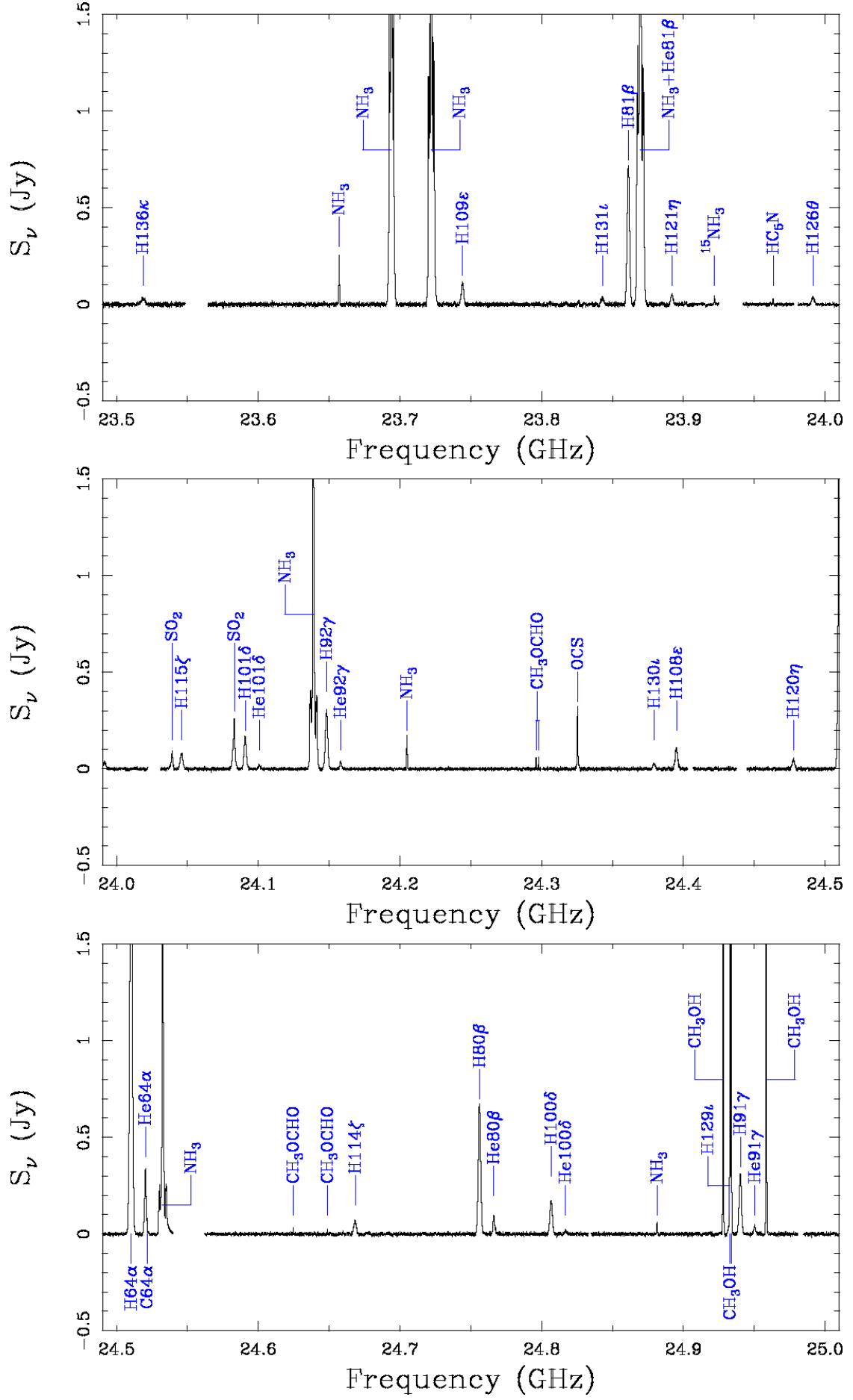


Fig. B.1. — Continued.

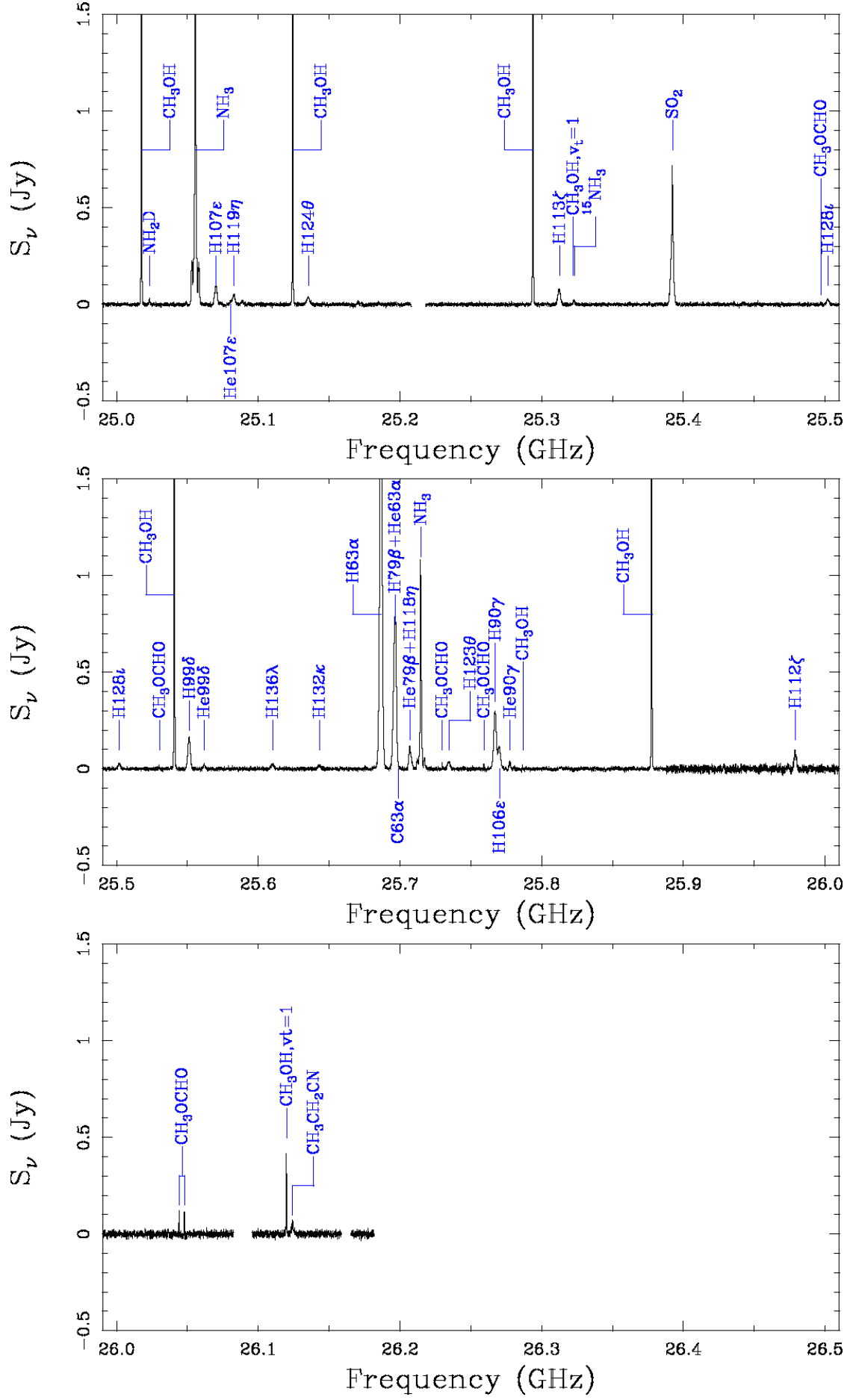


Fig. B.1. — Continued.

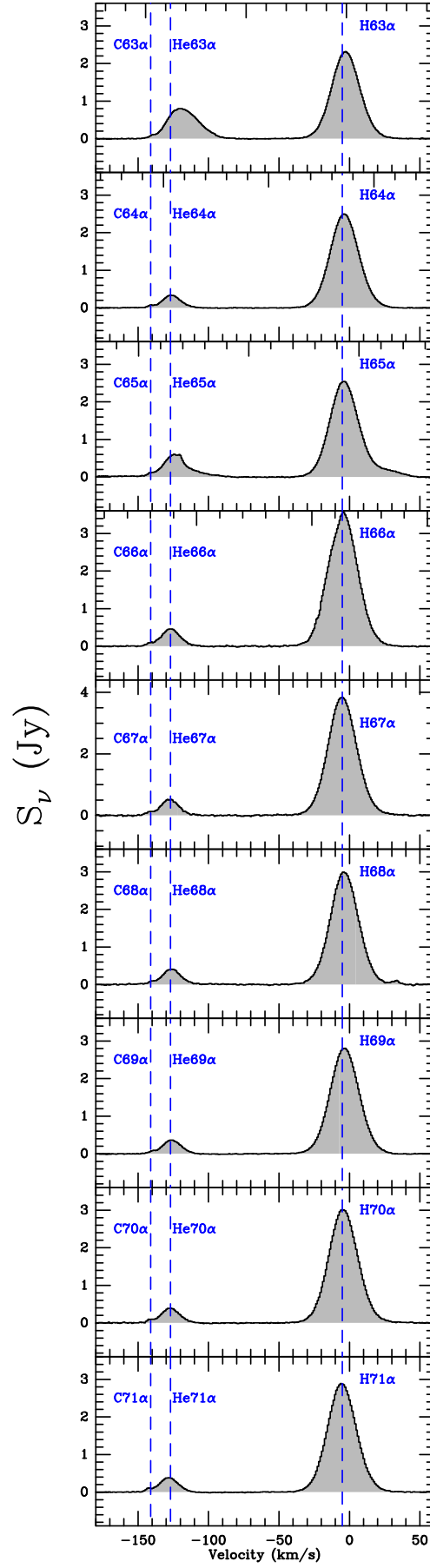


Fig. B.2. The observed H α , He α and C α transitions indicated by dashed lines with n and Δn (see Sect. 4.1) also given. He63 α is blended with H79 β while He65 α is blended with SO₂ ($5_{2,4} - 6_{1,5}$). The velocity scale refers to the respective H α line in each panel.

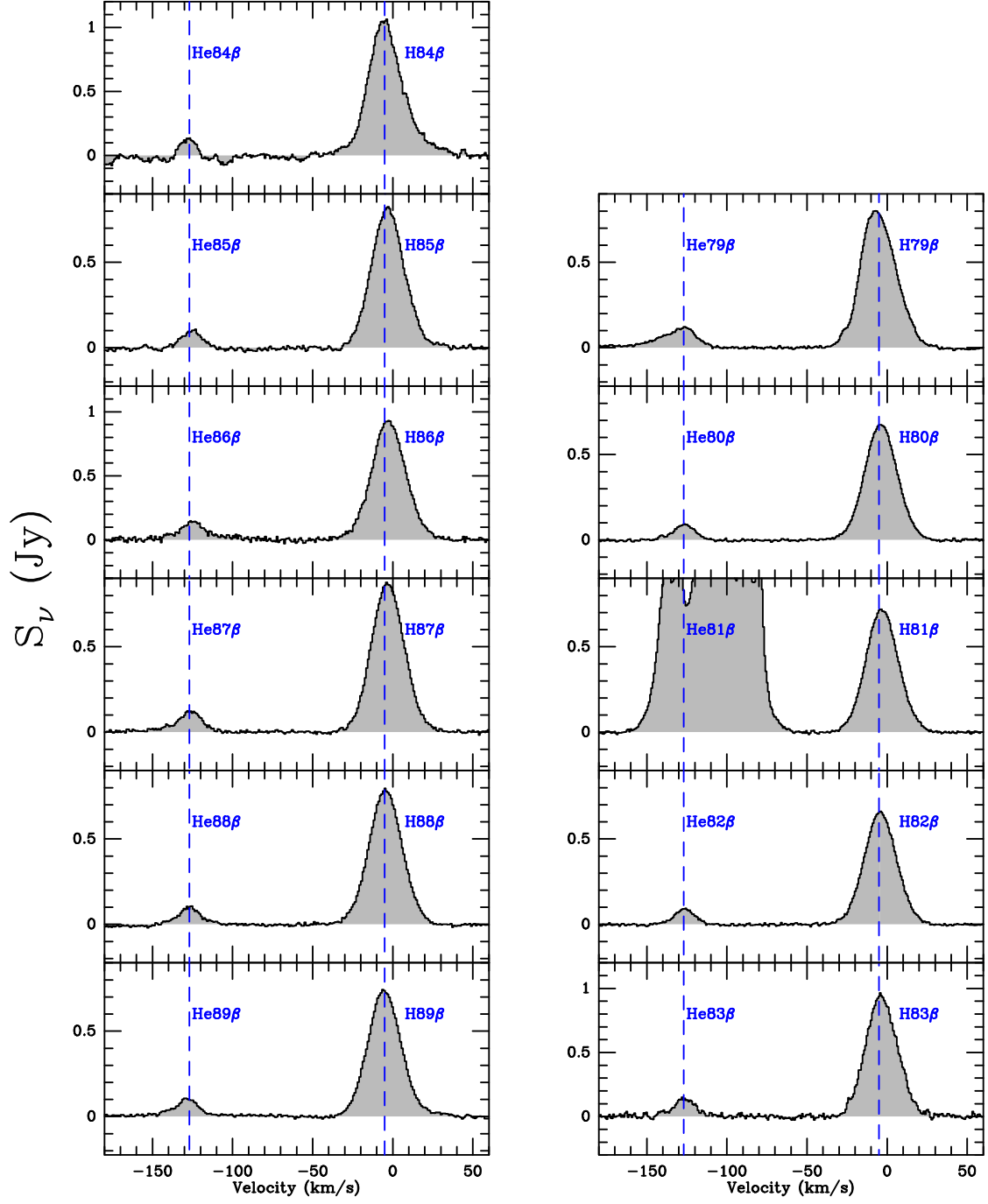


Fig. B.3. The observed H β and He β transitions indicated by dashed lines with n and Δn also given. H79 β is blended with He63 α while H81 β is blended with NH₃ (3,3). The velocity scale refers to the respective H β line in each panel.

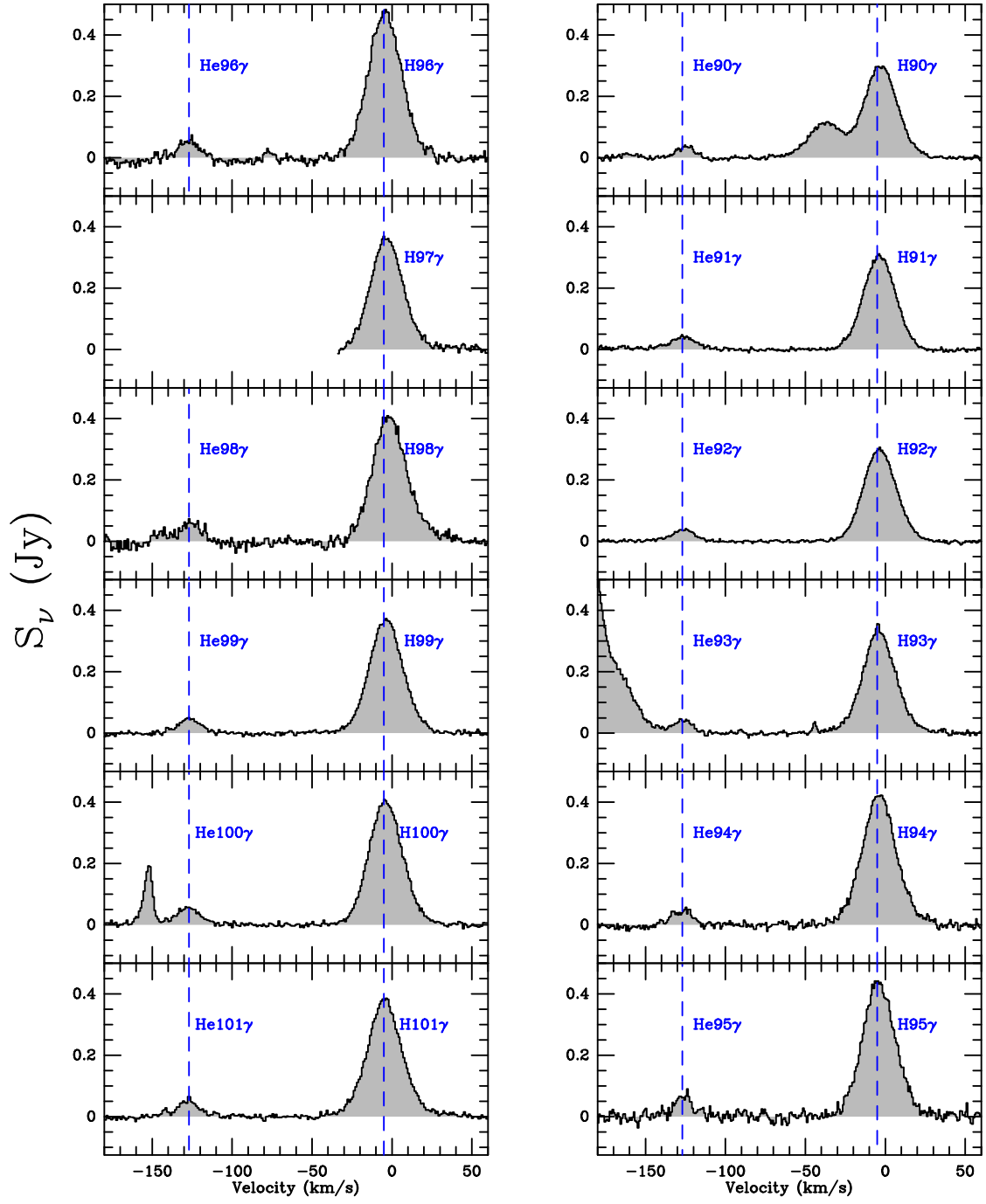


Fig. B.4. The observed H γ and H ϵ transitions indicated by dashed lines with n and Δn also given. The velocity scale refers to the respective H γ line in each panel. The spectrum near He100 γ is NH₃ (6,2).

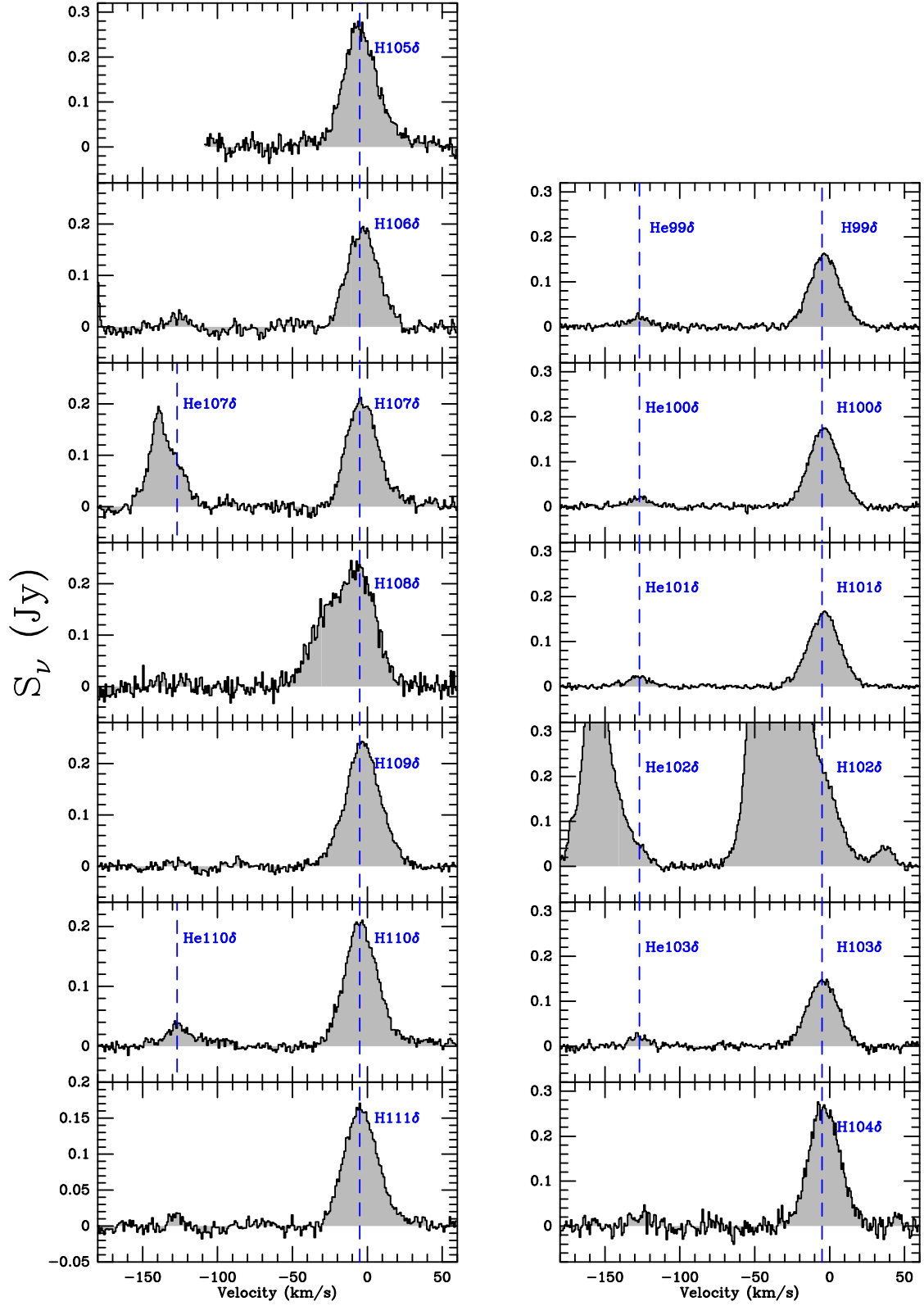


Fig. B.5. The observed H δ and He δ transitions indicated by dashed lines with n and Δn also given. The velocity scale refers to the respective H δ line in each panel.

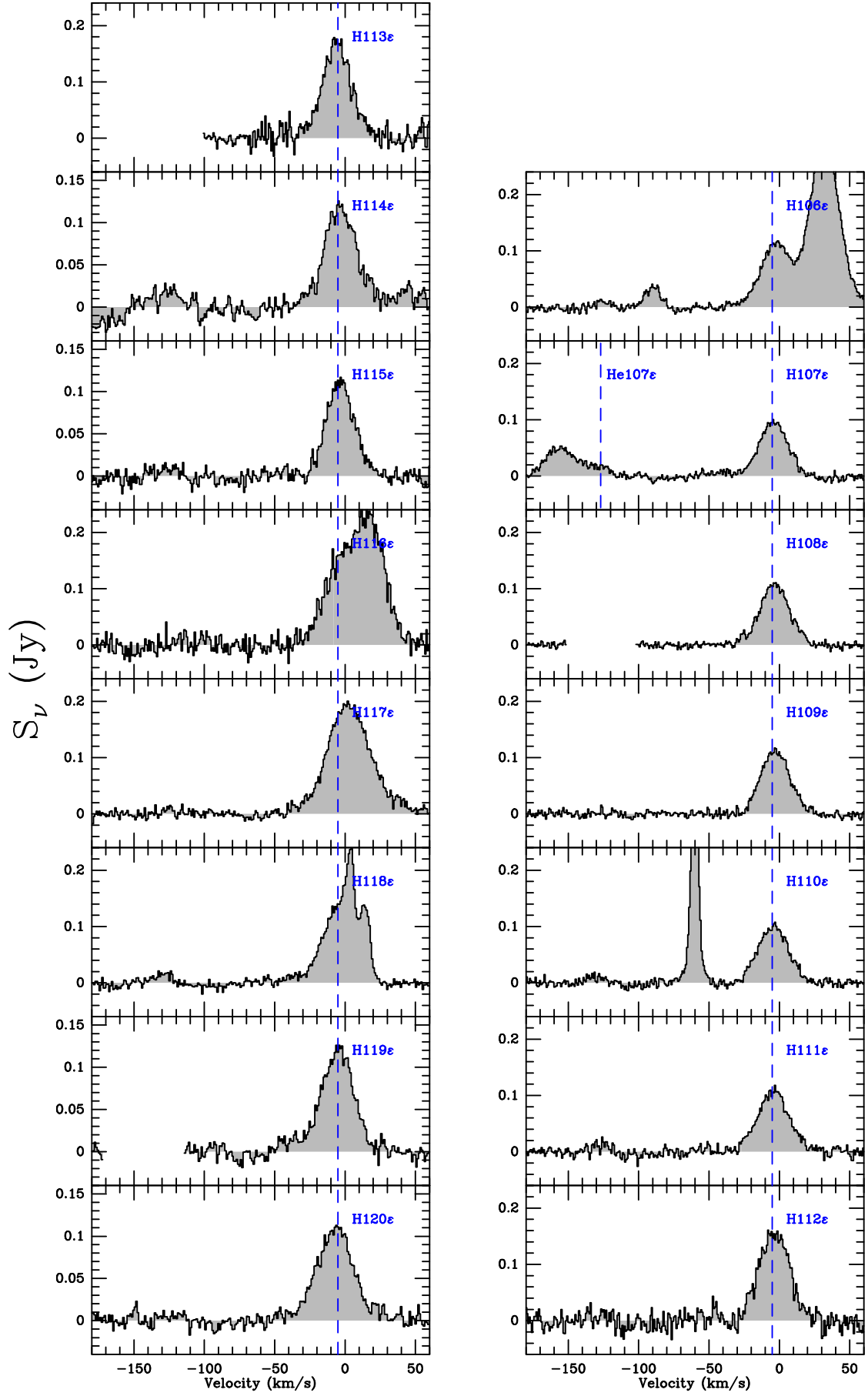


Fig. B.6. The observed H ϵ and He ϵ transitions indicated by dashed lines with n and Δn also given. The velocity scale refers to the respective H ϵ line in each panel.

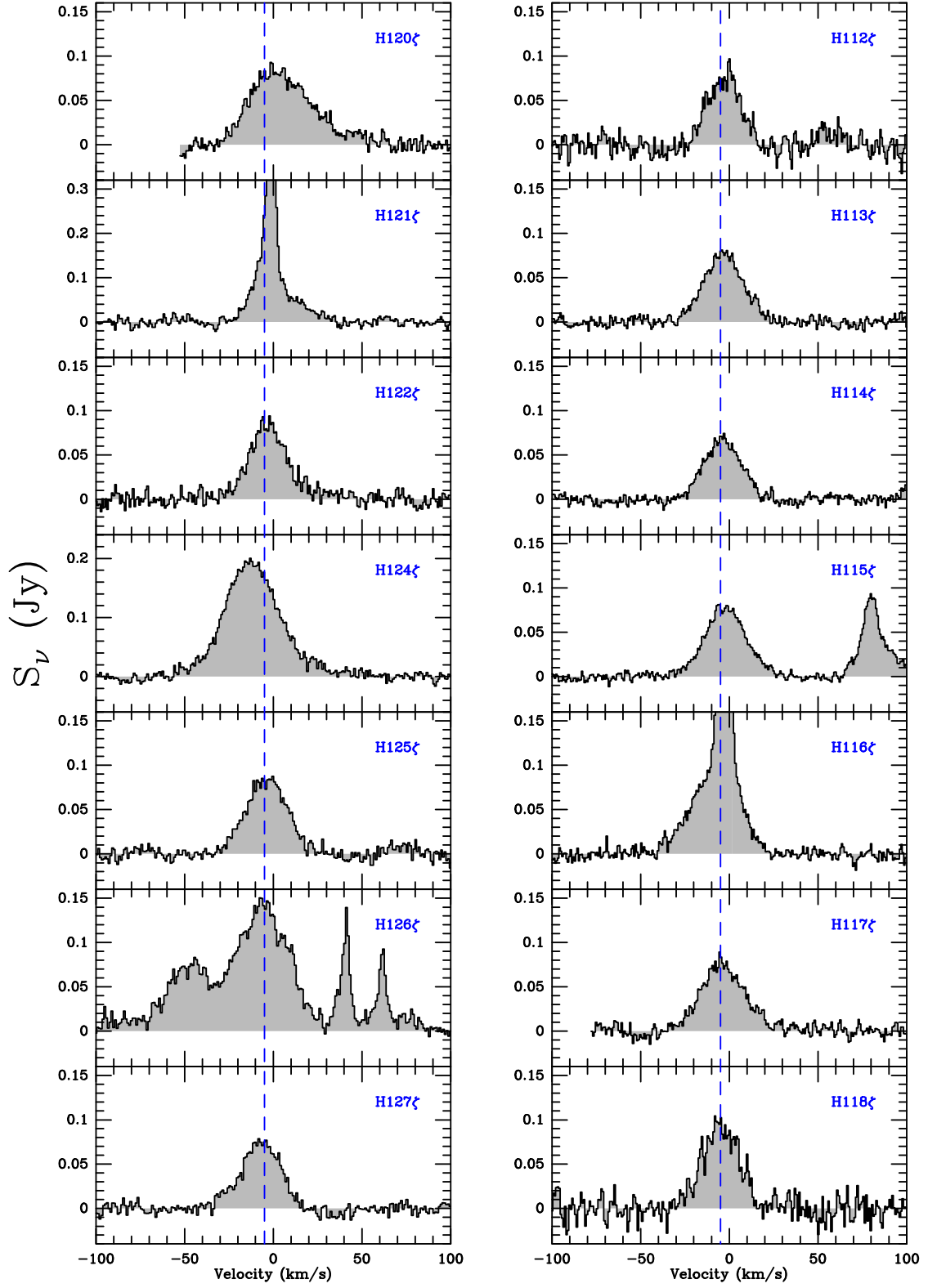


Fig. B.7. The observed H ζ transitions indicated by dashed lines with n and Δn also given. The velocity scale refers to the respective H ζ line in each panel.

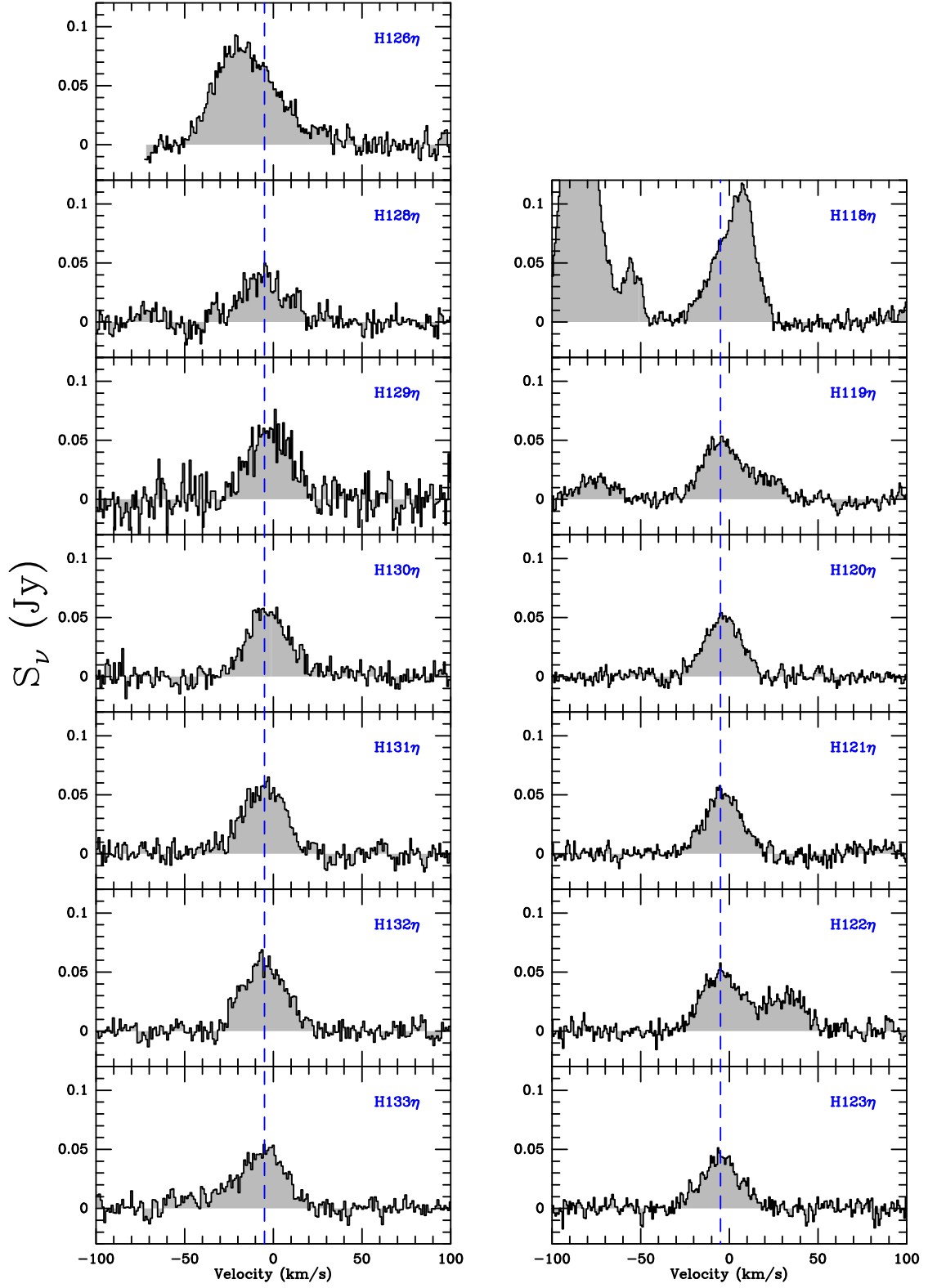


Fig. B.8. The observed $H_n\gamma$ transitions indicated by dashed lines with n and Δn also given. The velocity scale refers to the respective $H_n\gamma$ line in each panel.

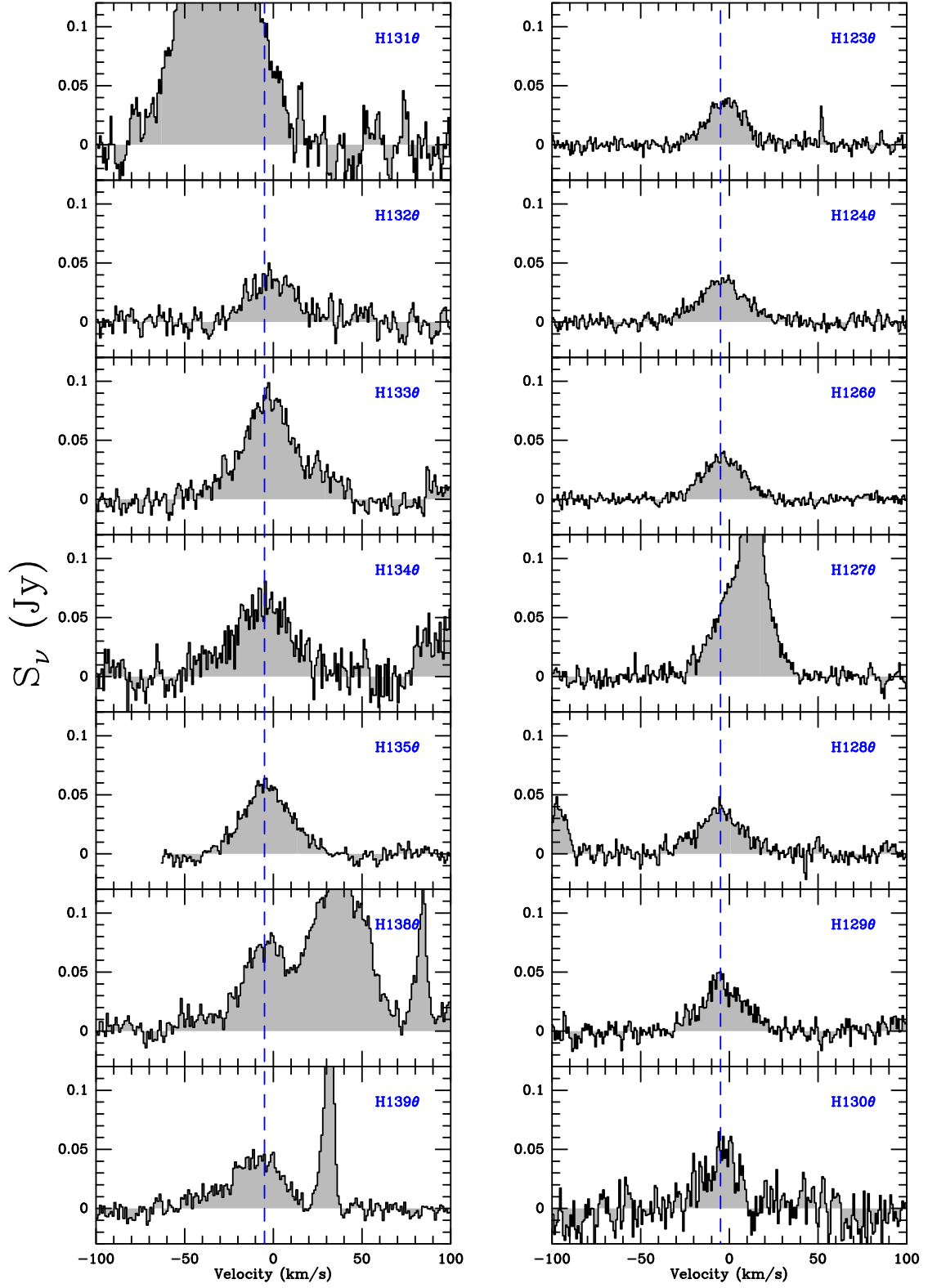


Fig. B.9. The observed $H\theta$ transitions indicated by dashed lines with n and Δn also given. The velocity scale refers to the respective $H\theta$ line in each panel.

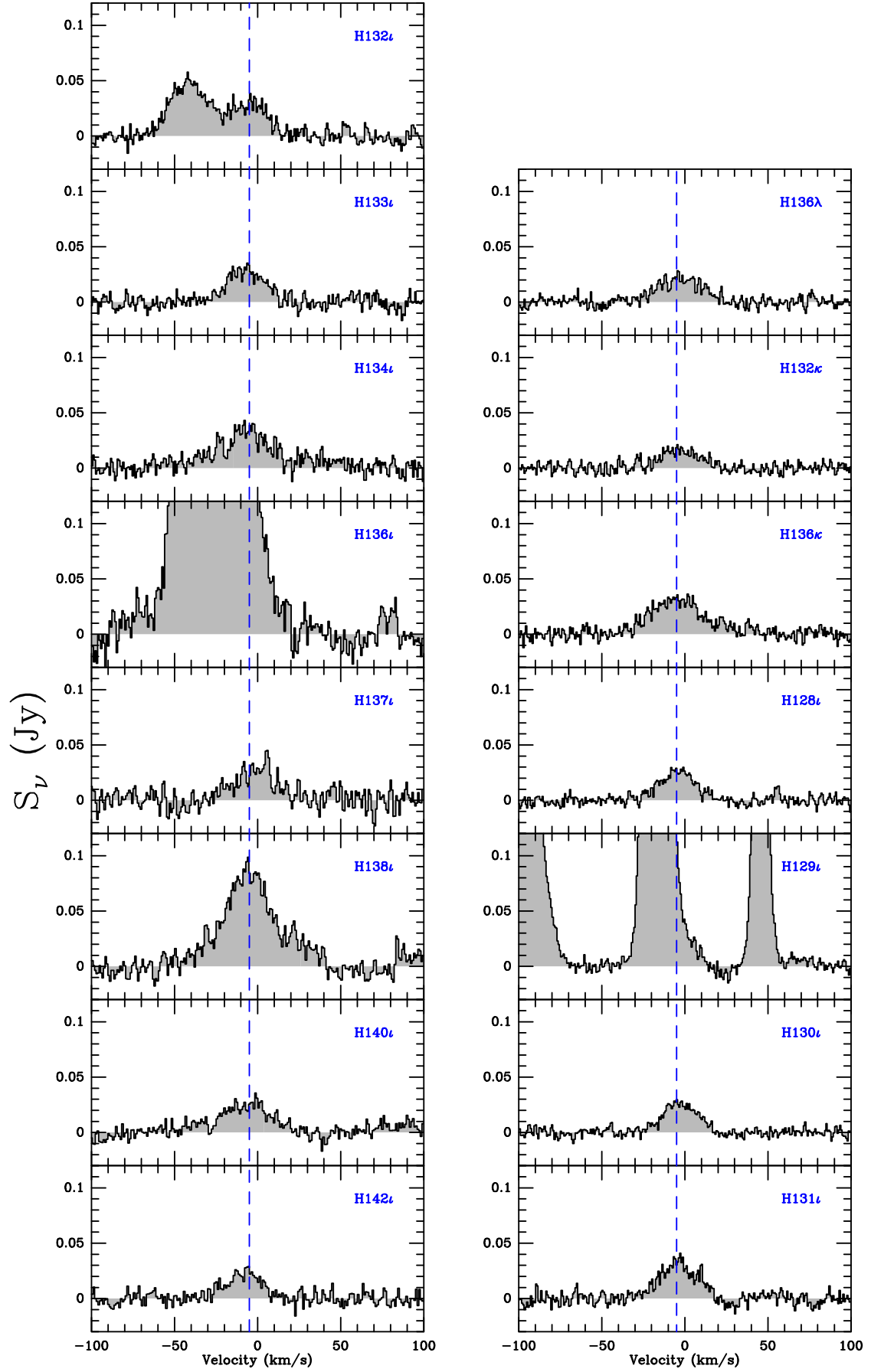


Fig. B.10. The observed H ϵ , H κ and H λ transitions indicated by dashed lines with n and Δn also given. The velocity scale refers to the respective H ϵ , H κ and H λ lines in each panel.

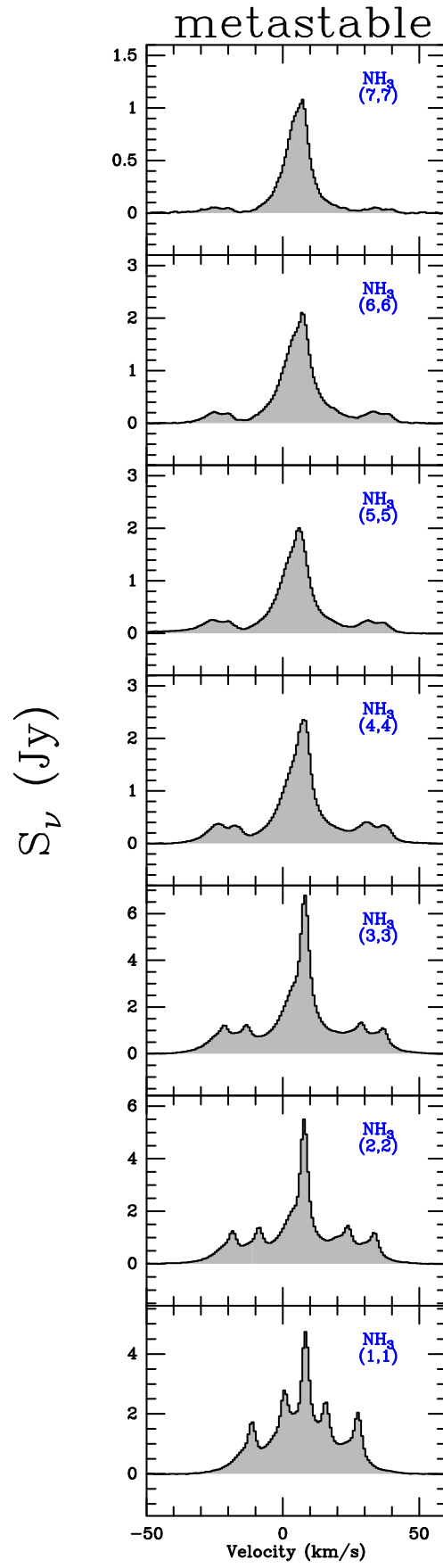


Fig. B.11. The observed NH_3 transitions with quantum numbers indicated in the upper right of each panel.

non-metastable

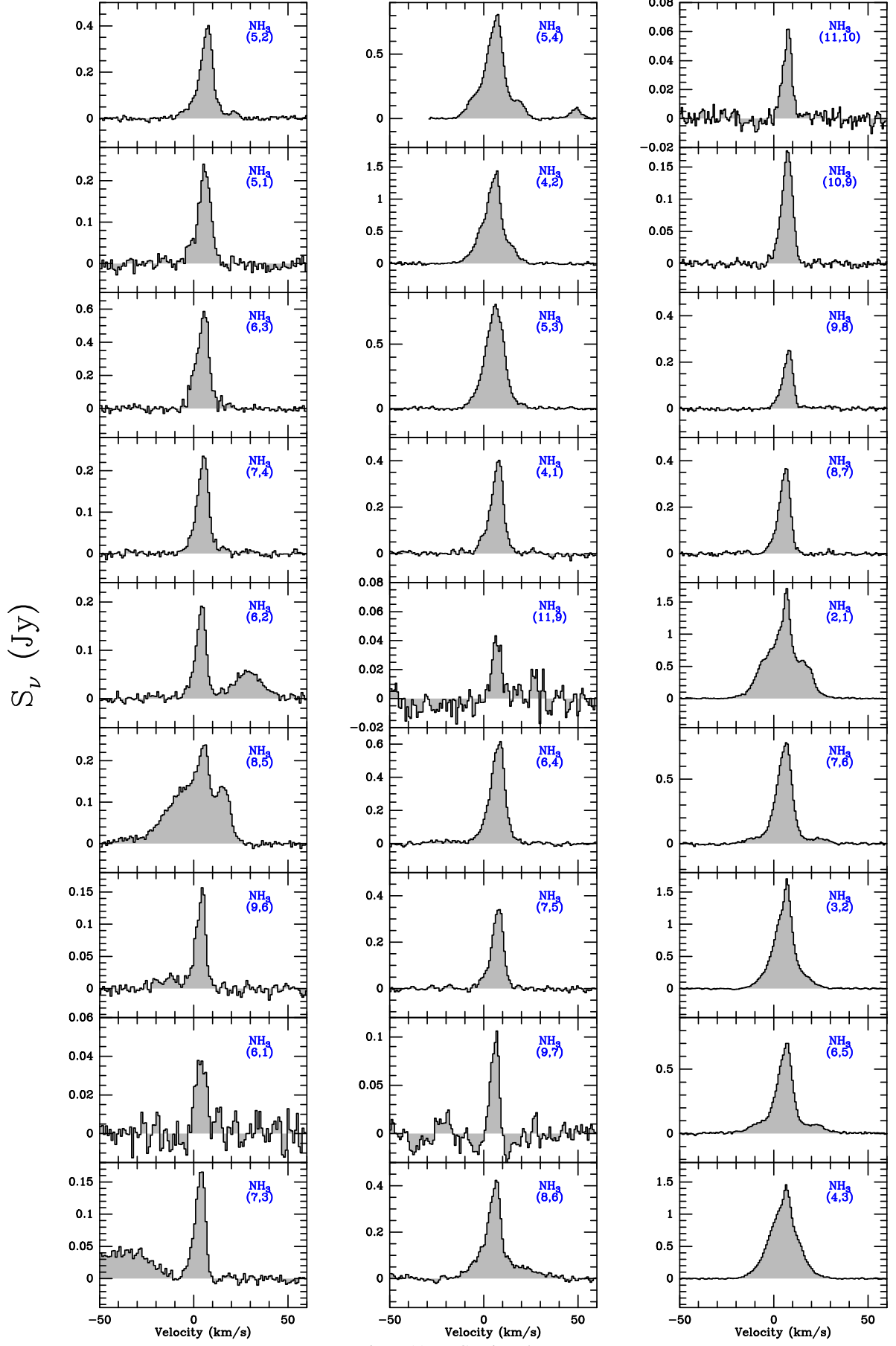


Fig. B.11. — Continued.

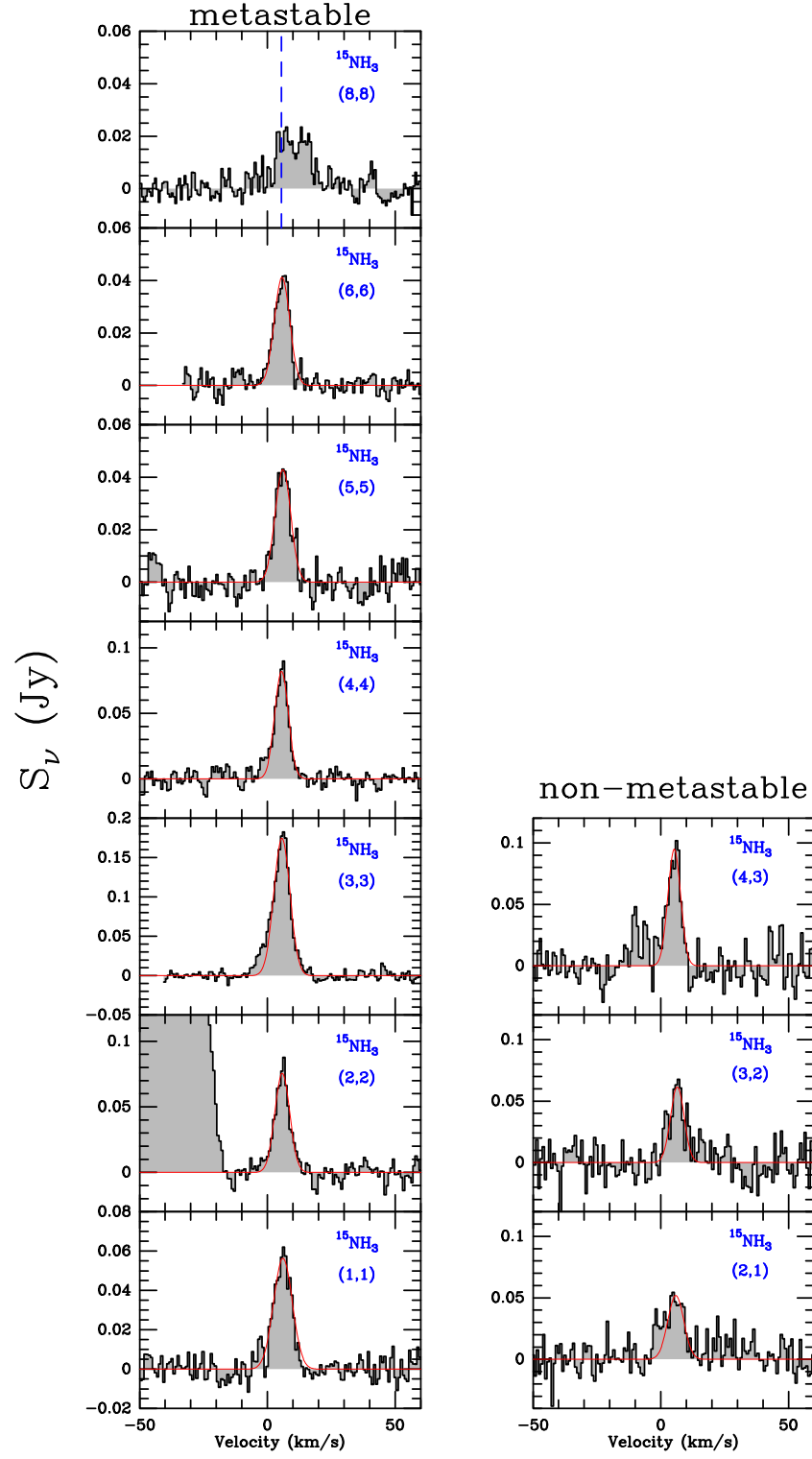


Fig. B.12. The observed $^{15}\text{NH}_3$ and NH_2D transitions with a one-component Gaussian fit shown (red lines). Quantum numbers are indicated in the upper right of each panel.

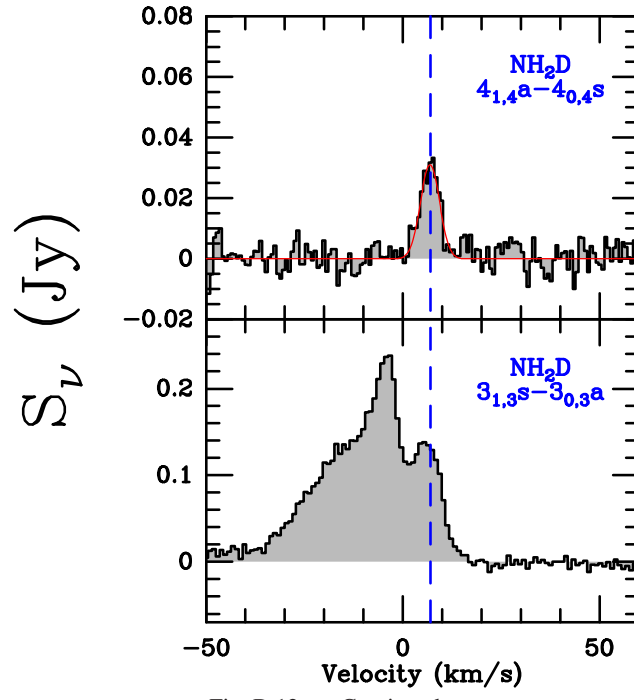


Fig. B.12. — Continued.

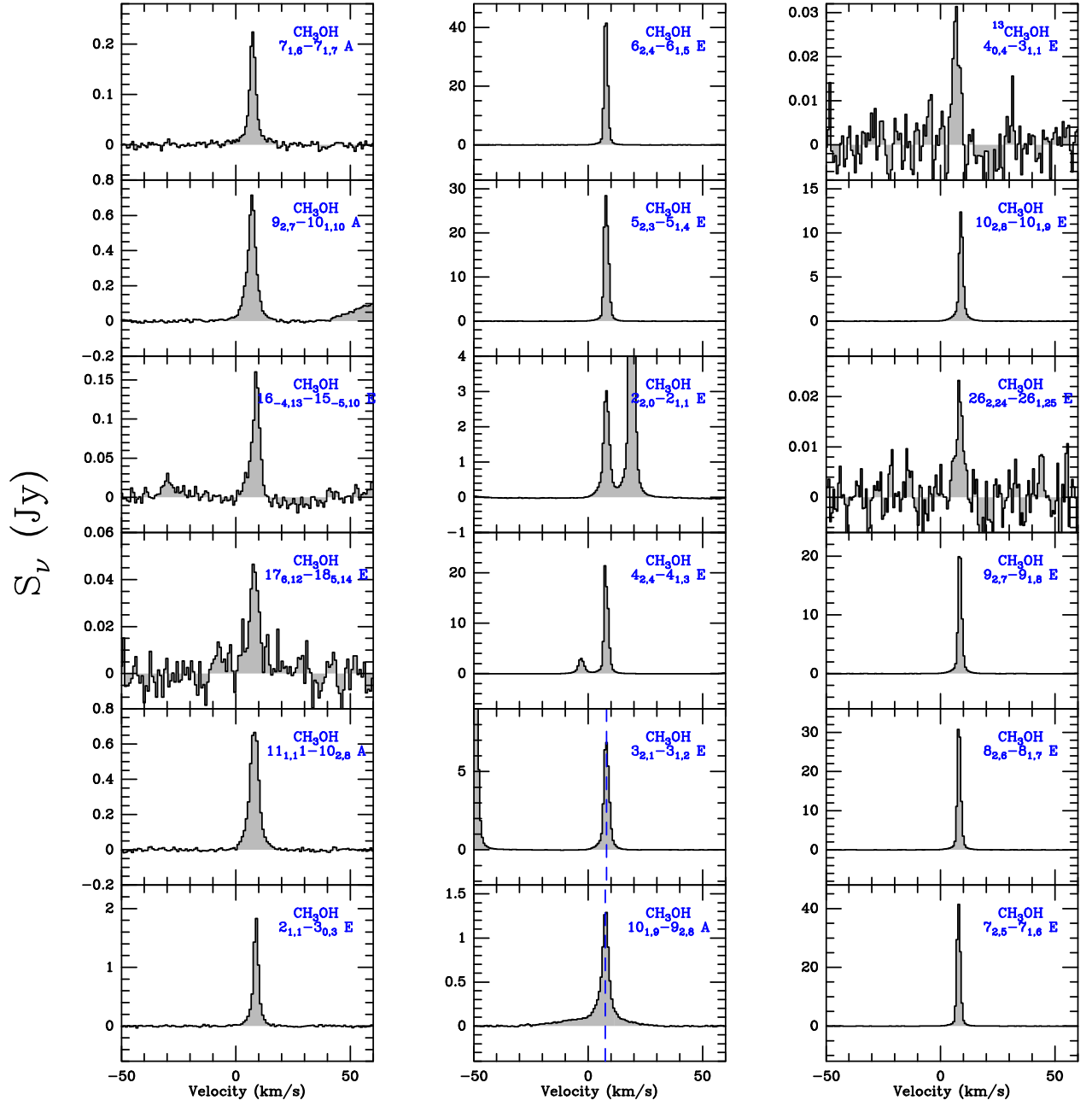
CH_3OH , $^{13}\text{CH}_3\text{OH}$ ($v_t=0$)


Fig. B.13. The observed CH_3OH and $^{13}\text{CH}_3\text{OH}$ transitions with a one-component Gaussian fit shown (red lines). Species and quantum numbers are given in the upper right of each panel.

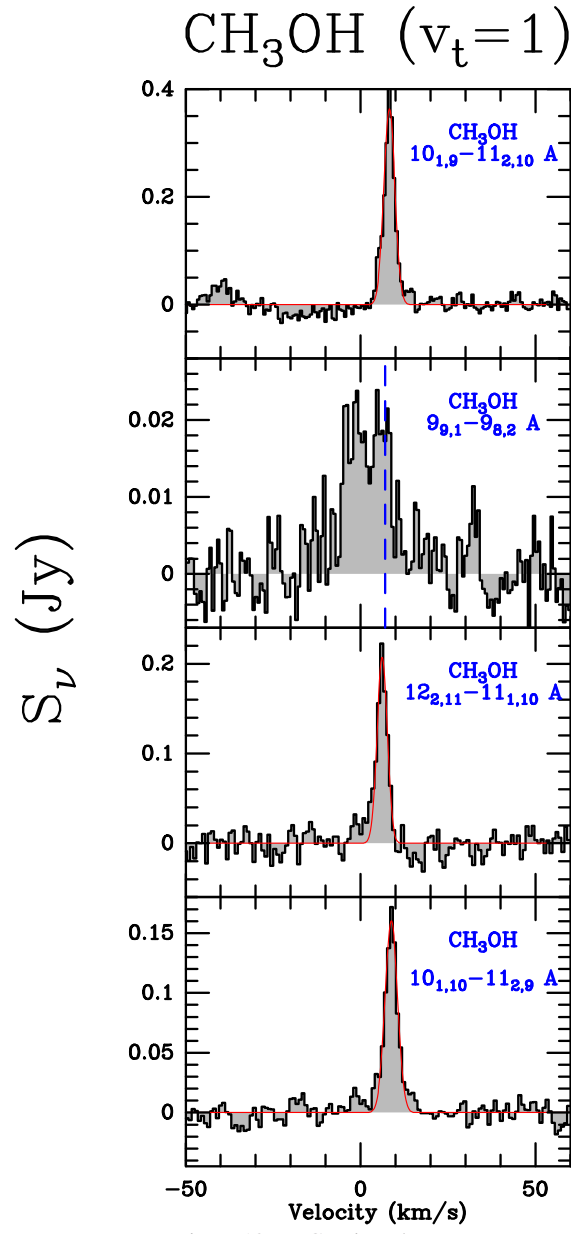


Fig. B.13. — Continued.

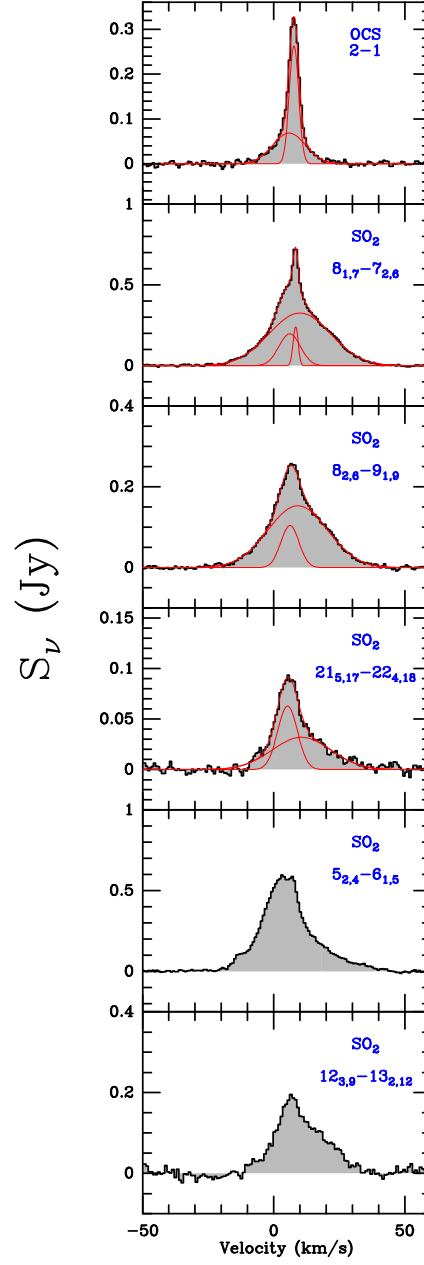


Fig. B.14. The observed SO₂ and OCS transitions (black lines) with a two- or three-component Gaussian fit shown together with the individual Gaussian components (red lines). Species and quantum numbers are given in the upper right of each panel. Note that SO₂ (5_{2,4}-6_{1,5}) is blended with He65 α at 23413.8 MHz and SO₂ (12_{3,9}-13_{2,12}) is blended with He107 δ at 20333.8 MHz.

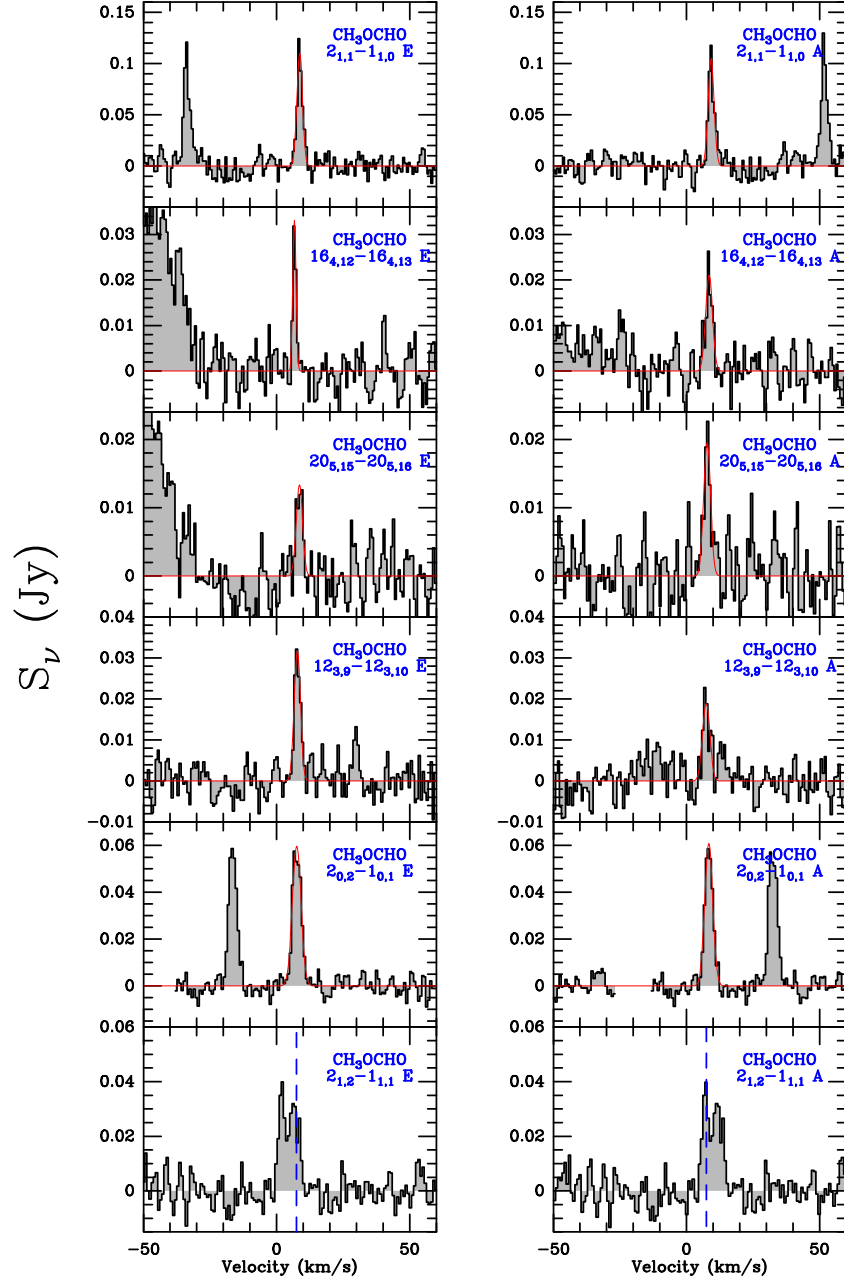


Fig. B.15. The observed CH_3OCHO transitions with one Gaussian fit shown (red lines). Species and quantum numbers are given in the upper right of each panel. In the CH_3OCHO ($2_{1,2}-1_{1,1}$ E) and CH_3OCHO ($2_{1,2}-1_{1,1}$ A) panels, the blue dashed lines represent the systemic velocities.

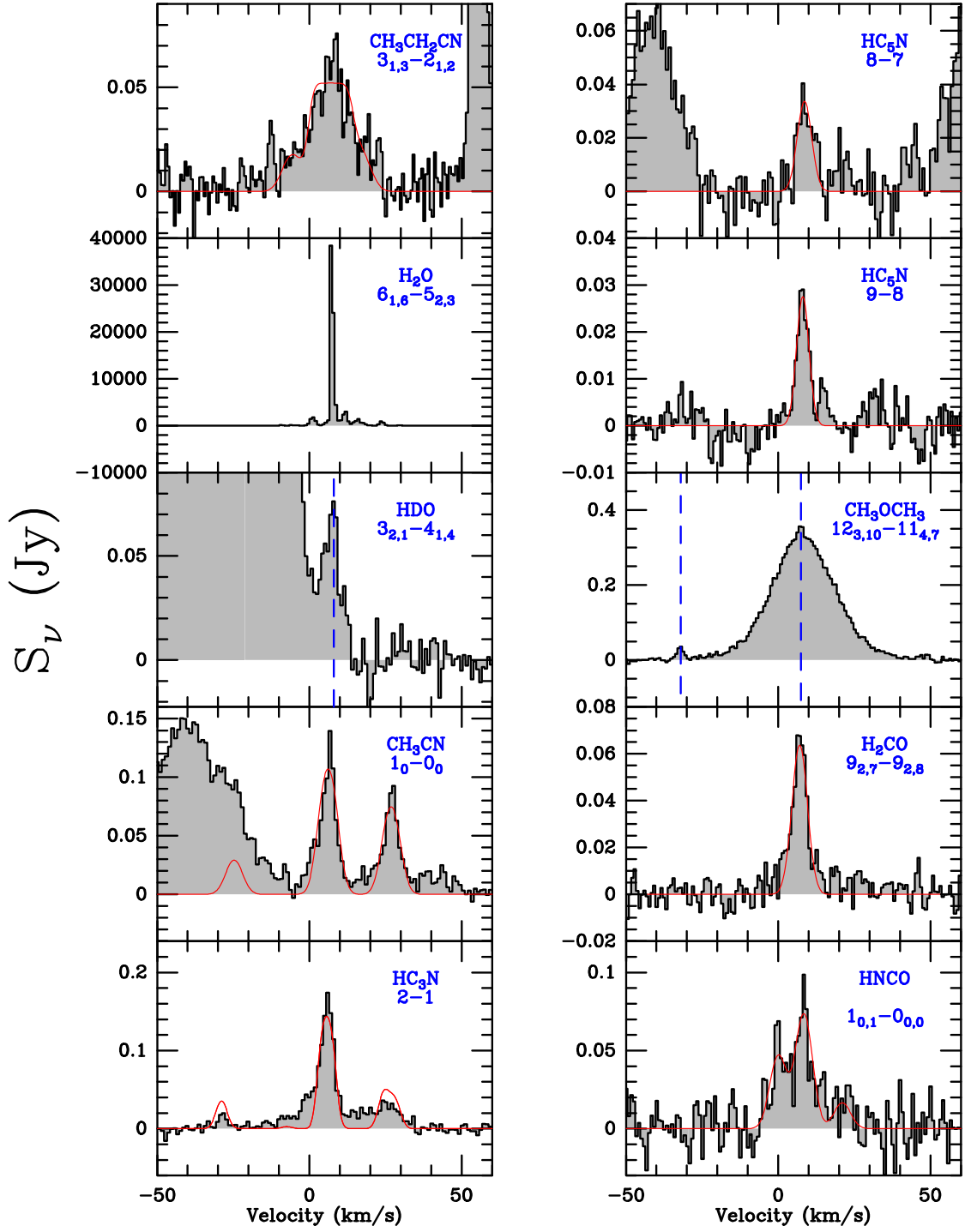


Fig. B.16. The observed HC_3N , CH_3CN , HDO , H_2O , HNCO , H_2CO , CH_3OCH_3 , HC_5N , and $\text{CH}_3\text{CH}_2\text{CN}$ transitions. Species and quantum numbers are indicated in the upper right of each panel. For HC_3N , CH_3CN , HNCO , and $\text{CH}_3\text{CH}_2\text{CN}$, the spectra are fitted with the HFS method indicated by red lines. For the HDO and CH_3OCH_3 transitions which are blended, their systemic velocity is indicated by blue dashed lines.

Appendix C: The ALMA maps of detected molecules and comparisons with other studies

We make use of the ALMA line survey archival data to study the distribution of molecules detected by our 1.3 cm line survey. The transitions used are listed in Table C.1. Fig. C.1 shows the channel maps of these transitions. Note that the first $[0,2] \text{ km s}^{-1}$ panel of NH_2D ($3_{2,2}s - 3_{1,2}a$) is contaminated by H_2CO ($9_{1,8} - 9_{1,9}$) at 216268.7 MHz.

Recently, Feng et al. (2015) studied Orion KL using combined SMA and IRAM 30m data, which covers parts of the frequency range of the ALMA-SV data. Here, we make a brief comparison between these data. By comparing the dust continuum emission in both datasets, mm2 in Feng et al. (2015) is resolved into MM4, MM5, and MM6 by ALMA. On the other hand, the dust continuum sources SR, NE, OF1N, and OF1S in Feng et al. (2015) are not detected in the ALMA-SV data. A comparison of OCS (18–17) demonstrates that Feng et al. (2015) show more extended emission while the ALMA-SV data display more sub-structures. That is because the ALMA-SV data have a higher spatial resolution but lack short spacing and have a smaller primary beam.

We also estimate the flux loss by comparing the ALMA-SV data with those obtained with the IRAM-30m single dish telescope. We make use of HC_3N (24–23) from Esplugues et al. (2013a), OCS (18–17) from Tercero et al. (2010), and SO_2 ($11_{5,7} - 12_{4,8}$) from Esplugues et al. (2013b). Based on the telescope information¹¹, we use a forward efficiency of 94%, a main beam efficiency of 63%, and a conversion factor from brightness temperature to flux of 7.5 Jy/K to derive the total flux observed by the IRAM-30m telescope. Meanwhile, the IRAM-30m telescope has a spatial resolution of $\sim 12''$, covering most emitting regions in Orion KL, so the IRAM-30m data can be considered to represent the total flux densities of Orion KL. By integrating the whole regions of the ALMA-SV data, we find that the ALMA-SV data can account for 89% of the HC_3N (24–23), 57% of the OCS (18–17), and 44% of the SO_2 ($11_{5,7} - 12_{4,8}$) emission.

¹¹ <http://www.iram.es/IRAMES/mainWiki/Iram30mEfficiencies>

Table C.1. Transitions from the ALMA line survey..

Frequencies (MHz)	Transitions	E_u/k (K)
Orion KL		
216562.7	NH ₂ D ($3_{2,2}s - 3_{1,2}a$)	120
218324.7	HC ₃ N ($24 - 23$)	131
218222.2	H ₂ CO ($3_{0,3} - 2_{0,2}$)	21
218903.4	OCS ($18 - 17$)	100
218981.0	HNCO ($10_{1,10} - 9_{1,9}$)	101
223200.1	CH ₃ OCH ₃ ($8_{2,7} - 7_{1,6} AE$)	38
229347.6	SO ₂ ($11_{5,7} - 12_{4,8}$)	122
233827.5	CH ₃ CH ₂ CN ($8_{4,5} - 7_{3,4}$)	33
235190.6	CH ₃ OCHO ($10_{9,1} - 10_{8,2} A$)	86
239064.3	CH ₃ CN ($13_4 - 12_4$)	195
243915.8	CH ₃ OH ($5_{1,4} - 4_{1,3} A$)	50

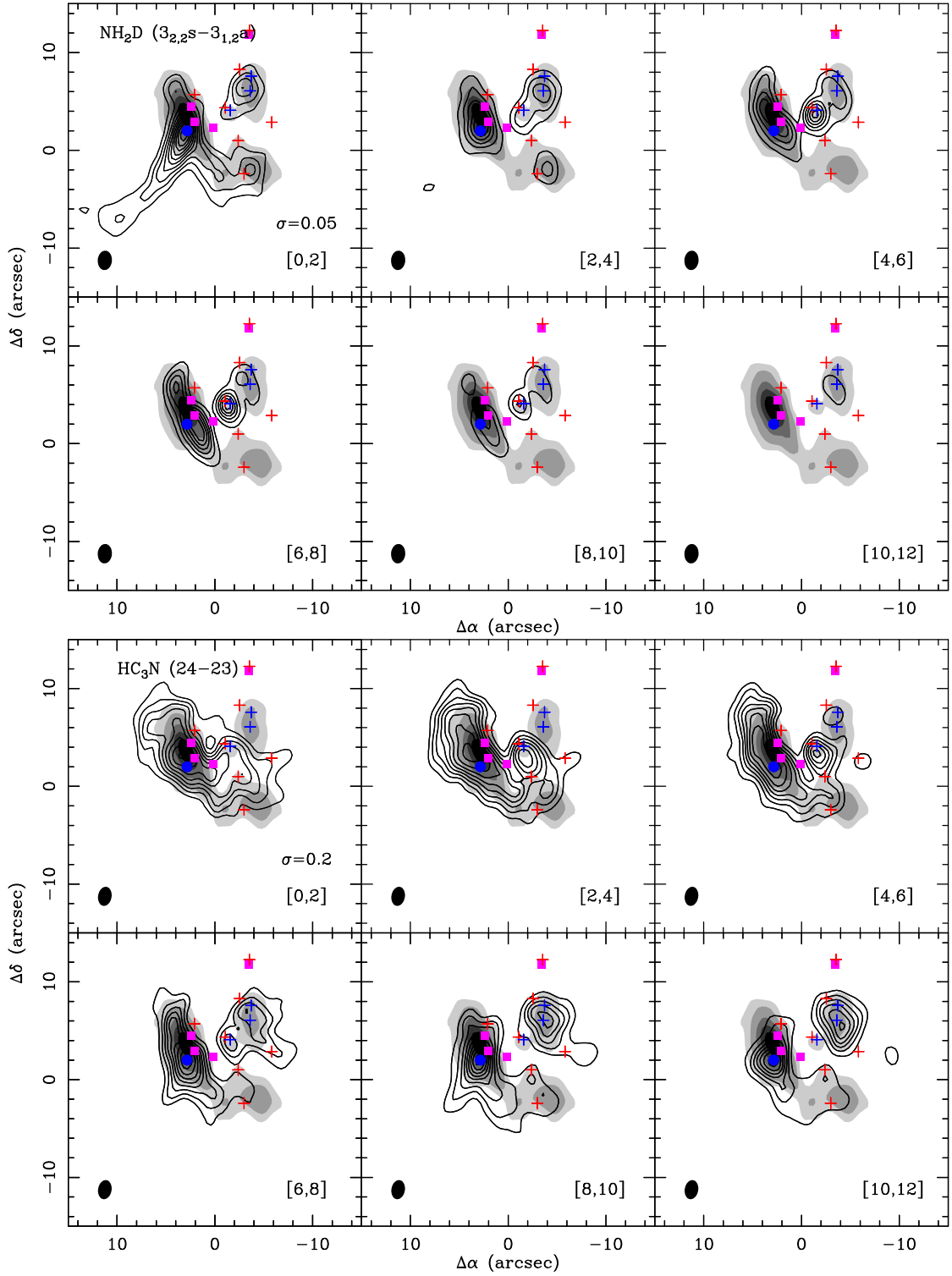


Fig. C.1. Molecular line channel maps (contours) overlaid on the 230 GHz continuum map (grey). Grey shadings of the continuum image are 10%, 20%, 40%, 60%, 80% of the peak intensity of $1.406 \text{ Jy beam}^{-1}$. The contour levels of the molecular line images start at 5σ and continue in steps of 5σ , where the σ value for each transition is shown in the first panel in units of Jy beam^{-1} . The dotted contours are the negative features with the same contour absolute levels as the positive ones in each panel. The symbols are the same as in Fig. 1. The corresponding molecular transitions are indicated in the upper left of the first panel. The velocity range is given in the lower right of each panel in km s^{-1} . The synthesized beams of the molecular line images are shown in the lower left of each panel. The (0, 0) position in each panel is $(\alpha_{J2000}, \delta_{J2000}) = (05^{\text{h}}35^{\text{m}}14.350^{\text{s}}, -05^{\circ}22'35.00'')$.

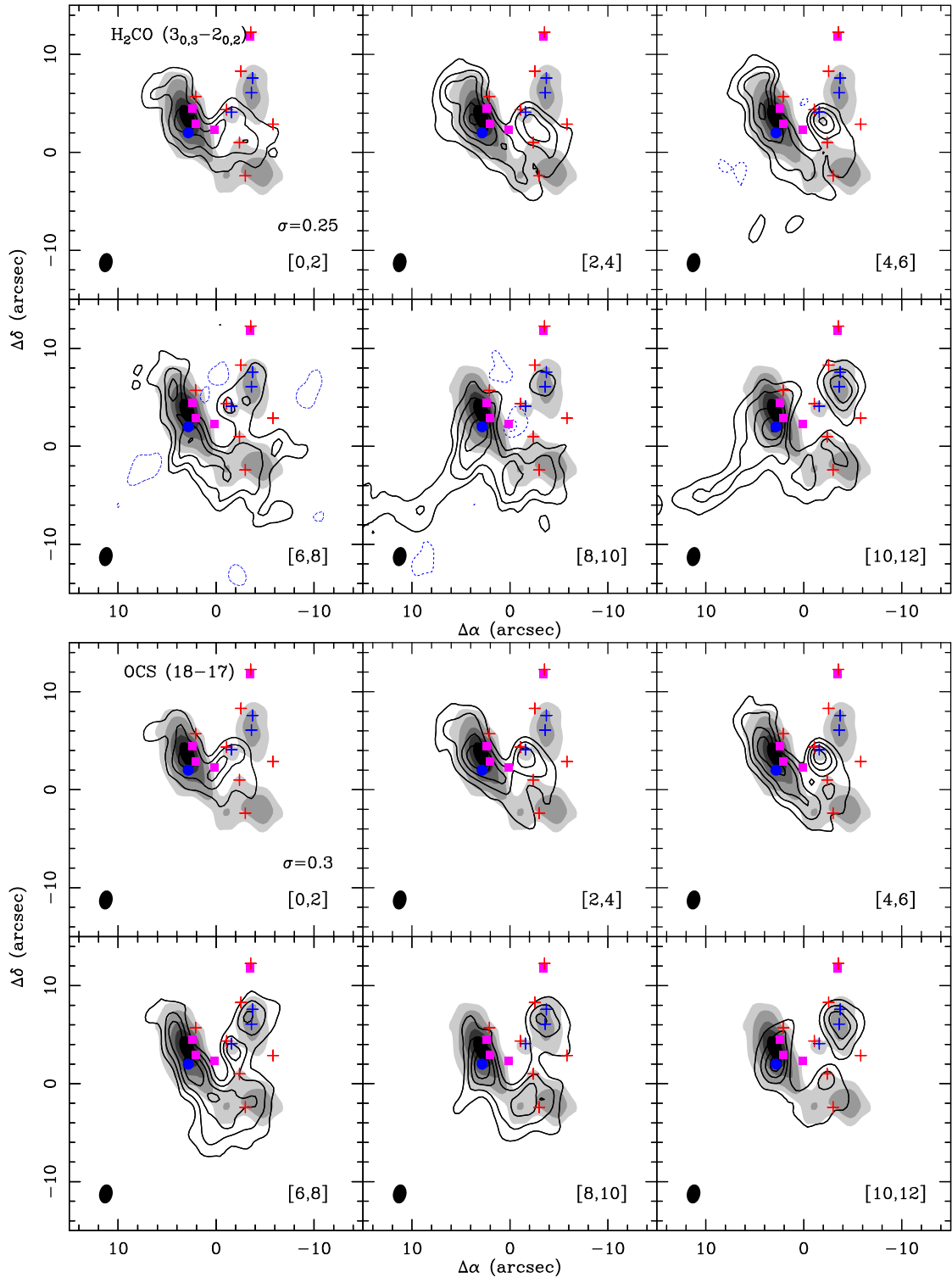


Fig. C.1. — Continued.

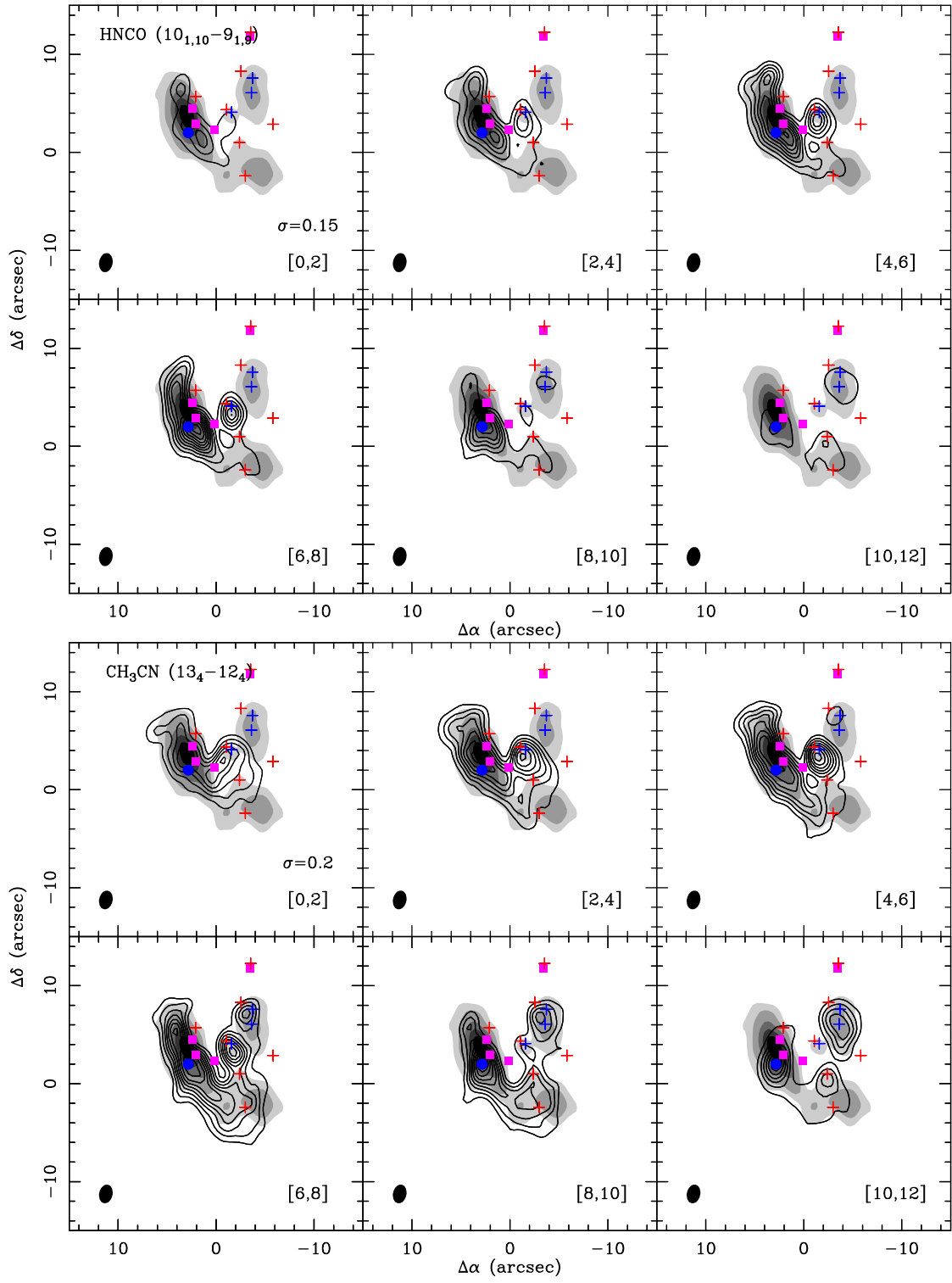


Fig. C.1. — Continued.

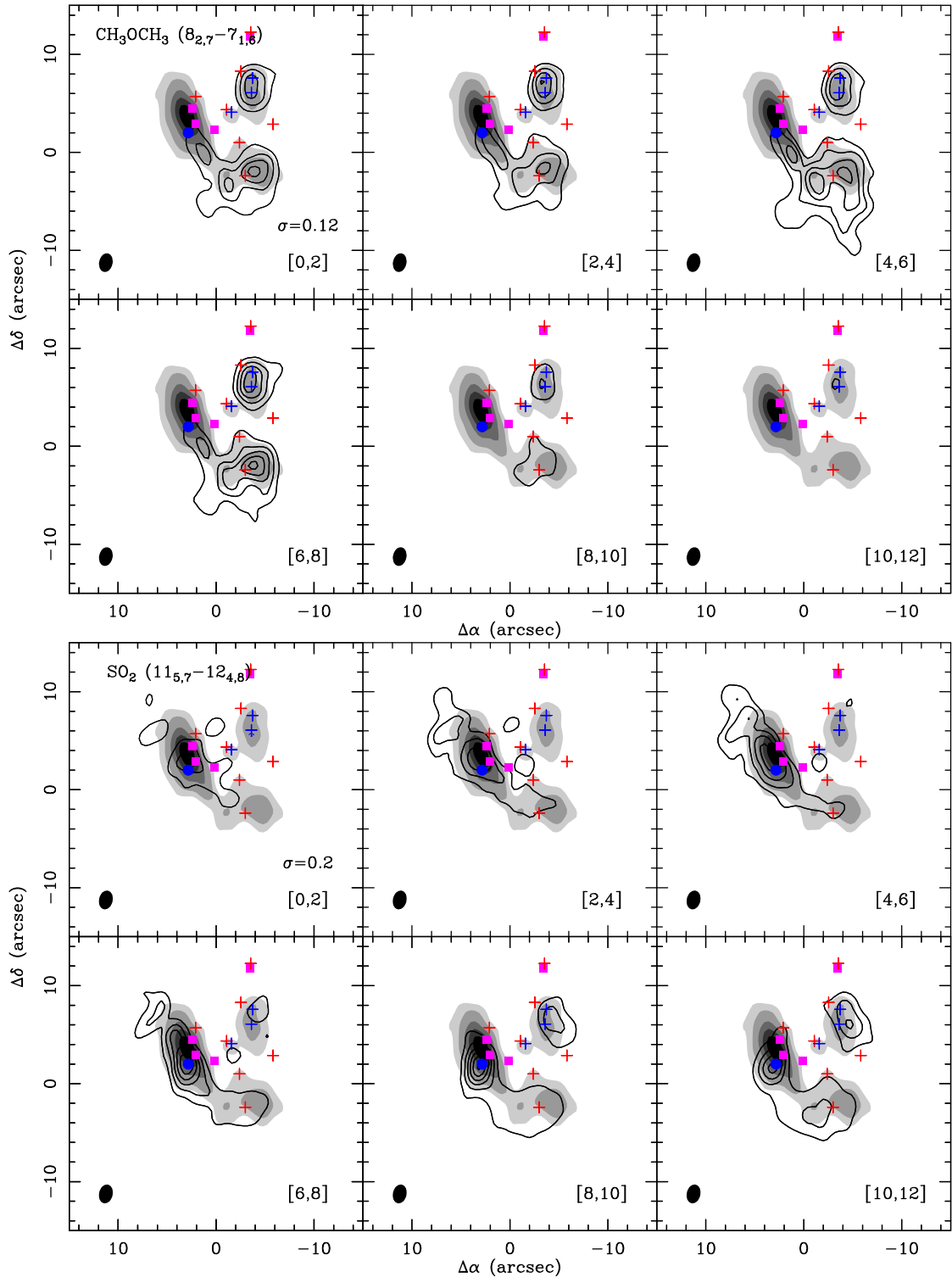


Fig. C.1. — Continued.

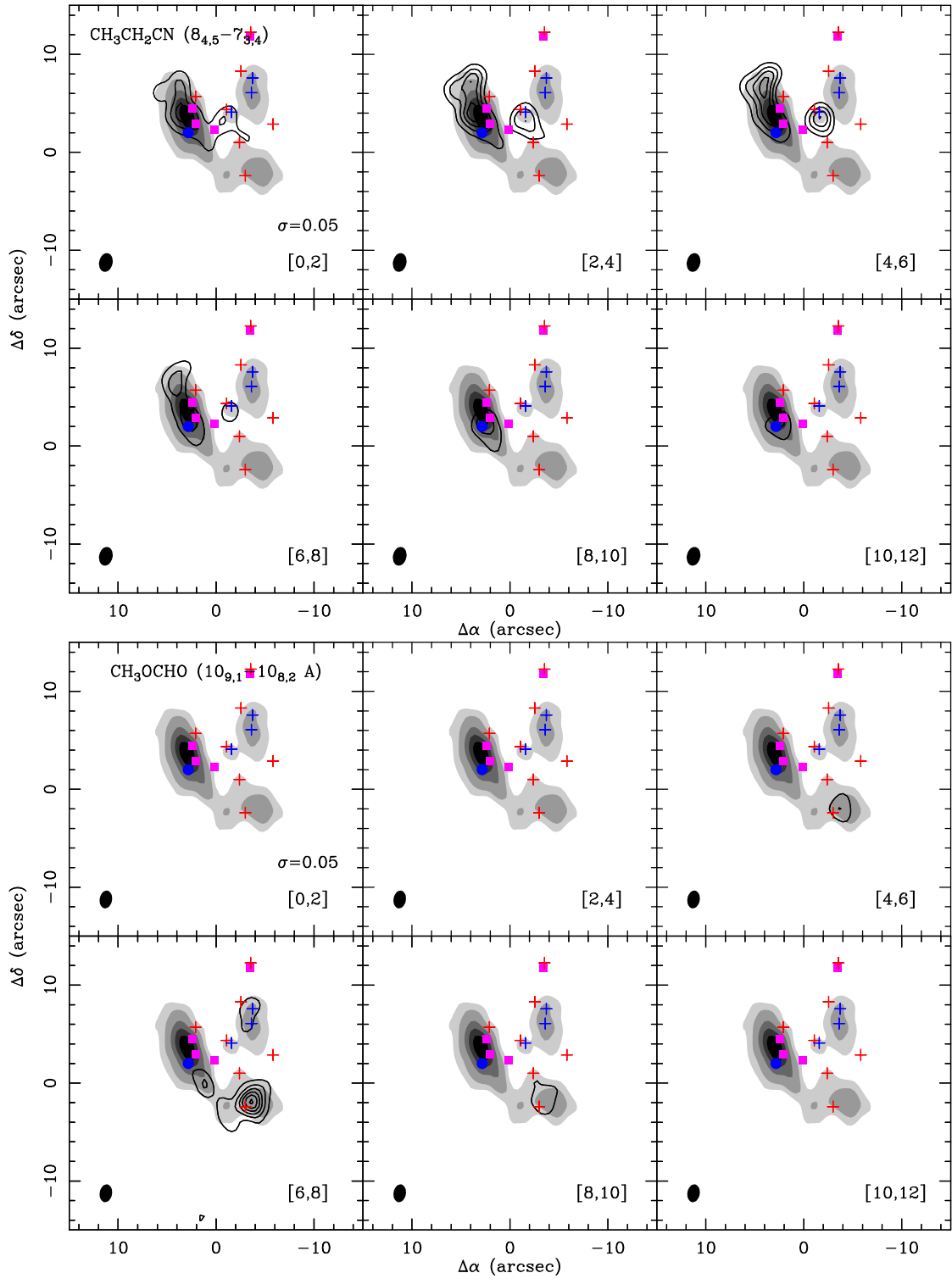


Fig. C.1. — Continued.

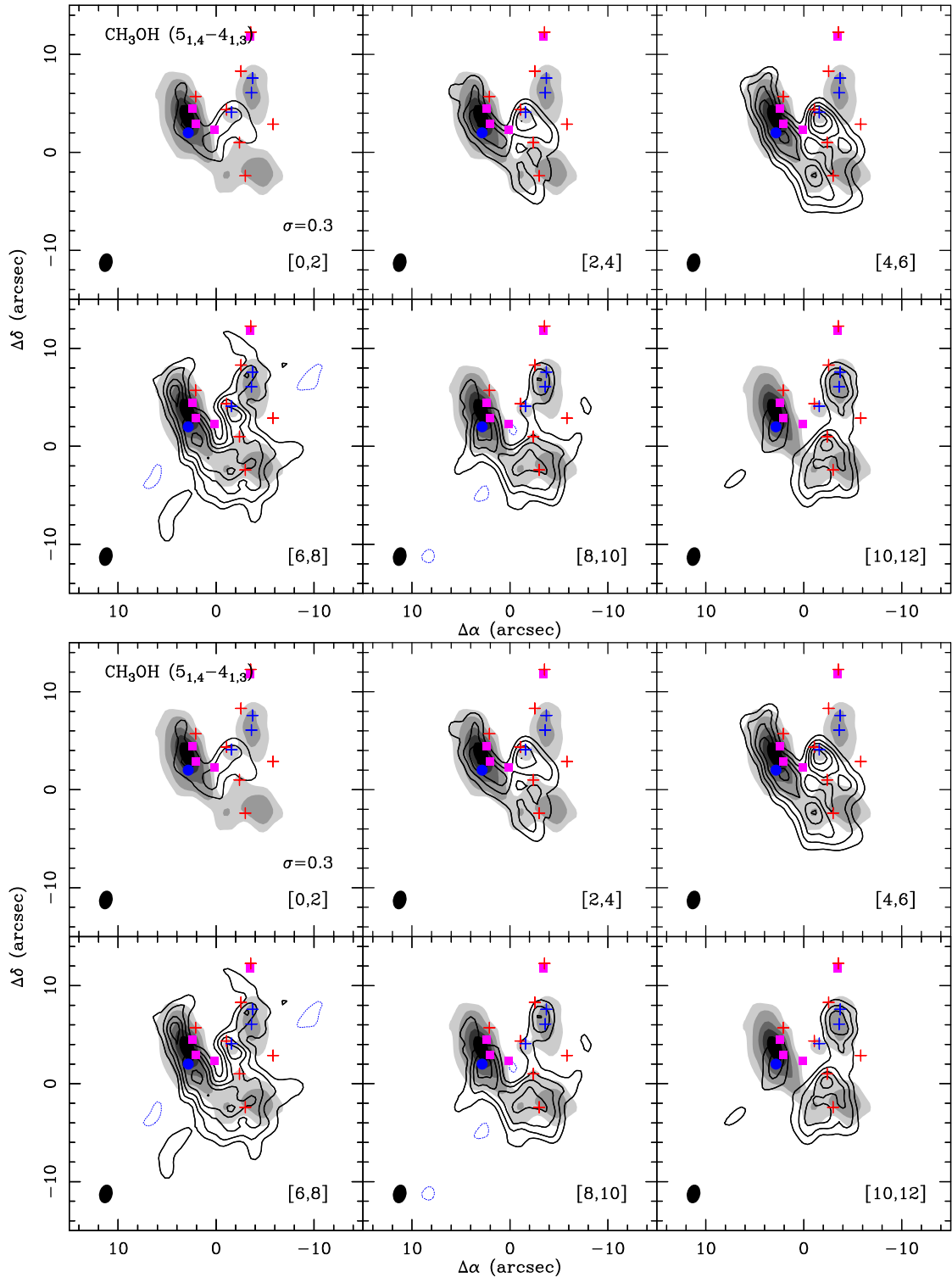


Fig. C.1. — Continued.